

UNCLASSIFIED

AD NUMBER

AD918103

LIMITATION CHANGES

TO:

Approved for public release; distribution is unlimited.

FROM:

Distribution authorized to U.S. Gov't. agencies only; Test and Evaluation; MAR 1974. Other requests shall be referred to Air Force Armament Development and Test Center, ATTN: ADTC/SD, Eglin AFB, FL 32542.

AUTHORITY

USADTC ltr dtd 5 Jun 1979

THIS PAGE IS UNCLASSIFIED

APR 12 1974

APR 15 1974
MAY 09 1983

cy.2



AERODYNAMIC AND INLET CHARACTERISTICS OF THE HAST I AND II MISSILES AT MACH NUMBERS 0.5 TO 1.6

-12
-8 to 16'

0
2
4
8

J. B. Carman
ARO, Inc.

.8 0 .95 1.05

1.2 1.6 1.96

PROPULSION WIND TUNNEL FACILITY
ARNOLD ENGINEERING DEVELOPMENT CENTER
AIR FORCE SYSTEMS COMMAND
ARNOLD AIR FORCE STATION, TENNESSEE 37389

March 1974

TECHNICAL REPORTS FILE COPY

Final Report for Period September 22, 1973 - November 20, 1973

Distribution limited to U. S. Government agencies only; this report contains information on test and evaluation of military hardware; March 1974; other requests for this document must be referred to Air Force Armament Development and Test Center (ADTC/SD), Eglin AFB, FL 32542.

Prepared for

AIR FORCE ARMAMENT DEVELOPMENT AND TEST CENTER (ADTC/SD)
AIR FORCE SYSTEMS COMMAND
EGLIN AFB, FL 32542

Approved for Release by the Air Force

Approved for Release by the Air Force

cy 2

NOTICES

When U. S. Government drawings specifications, or other data are used for any purpose other than a definitely related Government procurement operation, the Government thereby incurs no responsibility nor any obligation whatsoever, and the fact that the Government may have formulated, furnished, or in any way supplied the said drawings, specifications, or other data, is not to be regarded by implication or otherwise, or in any manner licensing the holder or any other person or corporation, or conveying any rights or permission to manufacture, use, or sell any patented invention that may in any way be related thereto.

Qualified users may obtain copies of this report from the Defense Documentation Center.

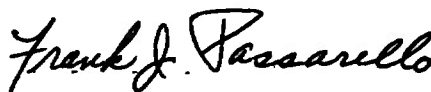
References to named commercial products in this report are not to be considered in any sense as an endorsement of the product by the United States Air Force or the Government.

APPROVAL STATEMENT

This technical report has been reviewed and is approved.



LAMAR R. KISSLING
Lt Colonel, USAF
Chief Air Force Test Director, PWT
Directorate of Test



FRANK J. PASSARELLO
Colonel, USAF
Director of Test

REPORT DOCUMENTATION PAGE		READ INSTRUCTIONS BEFORE COMPLETING FORM
1. REPORT NUMBER AEDC-TR-74-16 AFATL-TR-74-43	2. GOVT ACCESSION NO.	3. RECIPIENT'S CATALOG NUMBER
4. TITLE (and Subtitle) AERODYNAMIC AND INLET CHARACTERISTICS OF THE HAST I AND II MISSILES AT MACH NUM- BERS 0.5 TO 1.6	5. TYPE OF REPORT & PERIOD COVERED Final Report - September 22-November 20, 1973	
	6. PERFORMING ORG. REPORT NUMBER	
7. AUTHOR(s) J. B. Carman, ARO, Inc.	8. CONTRACT OR GRANT NUMBER(s)	
9. PERFORMING ORGANIZATION NAME AND ADDRESS Arnold Engineering Development Center (XO) Arnold Air Force Station, Tenn. 37389	10. PROGRAM ELEMENT, PROJECT, TASK AREA & WORK UNIT NUMBERS Program Element 63232F System 469A	
11. CONTROLLING OFFICE NAME AND ADDRESS Air Force Armament Development and Test Center (ADTC/SD), Eglin AFB, Florida 32542	12. REPORT DATE March 1974	
	13. NUMBER OF PAGES 108	
14. MONITORING AGENCY NAME & ADDRESS (if different from Controlling Office)	15. SECURITY CLASS. (of this report) UNCLASSIFIED	
	15a. DECLASSIFICATION/DOWNGRADING SCHEDULE N/A	
16. DISTRIBUTION STATEMENT (of this Report) Distribution limited to U.S. Government agencies only; this report contains information on test and evaluation of military hardware; March 1974; other requests for this document must be referred to Air Force Armament Development and Test Center (ADTC/SD), Eglin AFB, FL 32542.		
17. DISTRIBUTION STATEMENT (of the abstract entered in Block 20, if different from Report)		
18. SUPPLEMENTARY NOTES Available in DDC		
19. KEY WORDS (Continue on reverse side if necessary and identify by block number) HAST I missile aerodynamic characteristics HAST II missile stability transonic flow ogives air inlets wind tunnel tests cylindrical bodies canards wing-body configuration deflection		
20. ABSTRACT (Continue on reverse side if necessary and identify by block number) The aerodynamic and inlet characteristics were investigated for 0.25-scale models of the HAST I and II missiles. Mach number was varied from 0.5 to 1.6 for the HAST I test phase, but the HAST II models were tested only at Mach number 1.6. Reynolds number, based on model length, varied between 13.9 and 18.7 million. Data were obtained on the HAST I for canard deflection angles from -20 to 20 deg, aileron deflection angles from 0 to 10 deg, inlet capture area ratios from 0 to 1.2, angles of attack from -4 to 12 deg,		

20. Abstract (Continued)

and sideslip angles of 0 and 6 deg. Data were obtained on the HAST II at angles of attack from -4 to 4 deg with canard deflection angle, aileron deflection angle, and sideslip angle all zero. Also characteristics of 18 HAST I and six HAST II configurations were evaluated. Test results indicated that canard deflection significantly affected axial-force, pitching-moment, and trim characteristics while aileron deflection affected only the rolling-moment characteristics. The inlet performance parameters showed significant variation with changes in capture area ratio and free-stream Mach number.

PREFACE

The work reported herein was conducted by the Arnold Engineering Development Center (AEDC) and sponsored by the Air Force Armament Development and Test Center (ADTC/SD), Air Force Systems Command (AFSC), under Program Element 63232F, System 469A.

The test results presented were obtained by ARO, Inc. (a subsidiary of Sverdrup & Parcel and Associates, Inc.), contract operator of the AEDC, AFSC, Arnold Air Force Station, Tennessee. The tests were conducted from September 22 through November 20, 1973, under ARO Project No. PA402. The manuscript (ARO Control No. ARO-PWT-TR-74-5) was submitted for publication on January 10, 1974.

CONTENTS

	<u>Page</u>
1.0 INTRODUCTION	7
2.0 APPARATUS	
2.1 Test Facility	7
2.2 Test Article	7
2.3 Instrumentation	8
3.0 TEST PROCEDURE	
3.1 Test Conditions and Description	8
3.2 Data Reduction	9
3.3 Precision of Measurements	9
4.0 RESULTS AND DISCUSSION	
4.1 HAST I Inlet Characteristics	11
4.2 Basic HAST I Aerodynamic Characteristics	11
4.3 HAST I Component Buildup Characteristics	12
4.4 HAST II Aerodynamic and Inlet Characteristics	13
5.0 CONCLUDING REMARKS	13
REFERENCES	13

ILLUSTRATIONS

Figure

1. Schematic of Tunnel 4T Test Section Showing Model Location	15
2. Photograph Showing HAST I Model Installed in Tunnel 4T	16
3. Model Details	17
4. Sign Convention and Coordinate System	30
5. HAST I Inlet Mass Flow Functions, Capture Area Ratios and Throat Areas	31
6. Variation of the Inlet Plenum Pressures, Exit Pressures and Axial-Force Coefficients with Capture Area Ratio, Configuration 2, $\delta_c = \delta_a = \alpha = \beta = 0$	32
7. Effect of Angle of Attack on the Inlet Characteristics, $A_t = 0.505 \text{ in.}^2$, $\delta_c = \delta_a = \beta = 0$, Configuration 2	33
8. Effect of Angle of Sideslip on the Inlet Characteristics, $A_t = 0.505 \text{ in.}^2$, $\delta_c = \delta_a = \alpha = 0$, Configuration 2	34
9. Effect of Canard Deflection on the Inlet Characteristics, $A_t = 0.505 \text{ in.}^2$, $\delta_a = \alpha = \beta = 0$, Configuration 2	35

<u>Figure</u>	<u>Page</u>
10. Variation of the Inlet Characteristics with Mach Number, $\delta_c = \delta_a = \alpha = \beta = 0$, Configuration 2	36
11. Variation of the Inlet Characteristics with Model Configuration, $\delta_c = \delta_a = \alpha = \beta = 0$, $A_o/A_c = 0.7$	37
12. Effects of Capture Area Ratio on the Normal-Force, Pitching-Moment, and Axial-Force Coefficients, Configuration 2, $\delta_c = \delta_a = \beta = 0$	38
13. Variation of the Axial-Force and Base Pressure Characteristics with Capture Area Ratio at Zero Angle of Attack, Configuration 2, $\delta_c = \delta_a = \beta = 0$	44
14. Effects of Canard Deflection on the Normal-Force, Pitching-Moment, and Axial-Force Coefficients, $M_\infty = 0.8$, $A_t = 0.505 \text{ in.}^2$, $\delta_a = \beta = 0$	45
15. Effects of Canard Deflection on the Normal-Force, Pitching-Moment, and Axial-Force Coefficients, $M_\infty = 0.95$, $A_t = 0.505 \text{ in.}^2$, $\delta_a = \beta = 0$	48
16. Effects of Canard Deflection on the Normal-Force, Pitching-Moment, and Axial-Force Coefficients, $M_\infty = 1.1$, $A_t = 0.505 \text{ in.}^2$, $\delta_a = \beta = 0$	51
17. Effects of Canard Deflection on the Normal-Force, Pitching-Moment, and Axial-Force Coefficients, $M_\infty = 1.3$, $A_t = 0.505 \text{ in.}^2$, $\delta_a = \beta = 0$	54
18. Effects of Canard Deflection on the Normal-Force, Pitching-Moment, and Axial-Force Coefficients, $M_\infty = 1.6$, $A_t = 0.505 \text{ in.}^2$, $\delta_a = \beta = 0$	57
19. Effects of Afterbody and Antennas on C_{N_a} and C_{m_a} , $A_t = 0.505 \text{ in.}^2$, $\delta_c = \delta_a = \alpha = \beta = 0$	60
20. Effects of Canards, Afterbody, and Antennas on $C_{A,F}$, $A_t = 0.505 \text{ in.}^2$, $\delta_a = \alpha = \beta = 0$	61
21. Variations of Canard Effectiveness and Trim Angle with Mach Number, $A_t = 0.505 \text{ in.}^2$, $\delta_a = \beta = 0$	62
22. Effects of Canard Deflection on the Side-Force, Yawing-Moment, and Rolling-Moment Coefficients, $M_\infty = 0.8$, $A_t = 0.505 \text{ in.}^2$, $\delta_a = 0$, Configuration 2	64
23. Effects of Canard Deflection on the Side-Force, Yawing-Moment, and Rolling-Moment Coefficients, $M_\infty = 0.95$, $A_t = 0.505 \text{ in.}^2$, Configuration 2	66
24. Effects of Canard Deflection on the Side-Force, Yawing-Moment, and Rolling-Moment Coefficients, $M_\infty = 1.1$, $A_t = 0.505 \text{ in.}^2$, $\delta_a = 0$, Configuration 2	68

<u>Figure</u>	<u>Page</u>
25. Effects of Canard Deflection on the Side-Force, Yawing-Moment, and Rolling-Moment Coefficients, $M_\infty = 1.3$, $A_t = 0.505 \text{ in.}^2$, $\delta_a = 0$, Configuration 2	70
26. Effects of Canard Deflection on the Side-Force, Yawing-Moment, and Rolling-Moment Coefficients, $M_\infty = 1.6$, $A_t = 0.505 \text{ in.}^2$, $\delta_a = 0$, Configuration 2	72
27. Effects of Aileron Deflection on the Side-Force, Yawing-Moment, and Rolling-Moment Coefficients, $M_\infty = 0.8$, $A_t = 0.505 \text{ in.}^2$, $\delta_c = 0$, Configuration 2	74
28. Effects of Aileron Deflection on the Side-Force, Yawing-Moment, and Rolling-Moment Coefficients, $M_\infty = 0.95$, $A_t = 0.505 \text{ in.}^2$, $\delta_c = 0$, Configuration 2	76
29. Effects of Aileron Deflection on the Side-Force, Yawing-Moment, and Rolling-Moment Coefficients, $M_\infty = 1.1$, $A_t = 0.505 \text{ in.}^2$, $\delta_c = 0$, Configuration 2	78
30. Effects of Aileron Deflection on the Side-Force, Yawing-Moment, and Rolling-Moment Coefficients, $M_\infty = 1.3$, $A_t = 0.505 \text{ in.}^2$, $\delta_c = 0$, Configuration 2	80
31. Effects of Aileron Deflection on the Side-Force, Yawing-Moment, and Rolling-Moment Coefficients, $M_\infty = 1.6$, $A_t = 0.505 \text{ in.}^2$, Configuration 2, $\delta_c = \beta = 0$	82
32. Variation of Aileron Effectiveness with Mach Number, $A_t = 0.505 \text{ in.}^2$, $\delta_c = \alpha = \beta = 0$	83
33. Effect of Angle of Sideslip on the Side-Force, Yawing-Moment, and Rolling-Moment Coefficients, $M_\infty = 0.8$, $A_t = 0.505 \text{ in.}^2$, $\delta_c = 0$, Configuration 2	84
34. Effect of Angle of Sideslip on the Side-Force, Yawing-Moment, and Rolling-Moment Coefficients, $M_\infty = 0.95$, $A_t = 0.505 \text{ in.}^2$, $\delta_c = 0$, Configuration 2	86
35. Effect of Angle of Sideslip on the Side-Force, Yawing-Moment, and Rolling-Moment Coefficients, $M_\infty = 1.1$, $A_t = 0.505 \text{ in.}^2$, $\delta_c = 0$, Configuration 2	88
36. Effect of Angle of Sideslip on the Side-Force, Yawing-Moment, and Rolling-Moment Coefficients, $M_\infty = 1.3$, $A_t = 0.505 \text{ in.}^2$, $\delta_c = 0$, Configuration 2	90
37. Effect of Angle of Sideslip on the Side-Force, Yawing-Moment, and Rolling-Moment Coefficients, $M_\infty = 1.6$, $A_t = 0.50 \text{ in.}^2$, $\delta_c = \delta_a = 0$, Configuration 2	92

<u>Figure</u>	<u>Page</u>
38. Effects of Missile Components on the Longitudinal Stability Derivatives and Axial-Force Coefficients at Zero Angle of Attack, $\delta_c = \delta_a = \beta = 0$	93
39. Effects of Missile Components on the Normal-Force, Pitching-Moment, and Axial-Force Coefficients. $M_\infty = 1.6$, $\delta_c = \delta_a = \beta = 0$	96
40. Effects of Missile Components on the Side-Force, Yawing-Moment, and Rolling-Moment Coefficients, $M_\infty = 1.6$, $\delta_c = \delta_a = \beta = 0$	99
41. Effects of Angle of Attack on the Inlet Exit Total Pressure Distributions, $\delta_c = \delta_a = \beta = 0$	102

TABLES

1. Configuration Listing	103
2. Wind Tunnel Test Conditions	104
3. Test Summary	105
 NOMENCLATURE	 106

1.0 INTRODUCTION

Because of the addition of several antennas and other protuberances along with a 25-percent increase in the intake area of the ram air turbine inlet, a requirement existed to update the aerodynamic and inlet characteristics of the High Altitude Supersonic Target (HAST) missile. It was the purpose of the present investigation to determine the static stability, axial-force, and inlet characteristics of the present HAST I and HAST II missile configurations and also to evaluate the contribution of individual missile components to total missile performance. The tests were conducted in the Aerodynamic Wind Tunnel (4T) of the Propulsion Wind Tunnel Facility (PWT) using 0.25-scale models. Mach number was varied from 0.5 to 1.6 for the HAST I configurations while the HAST II models were tested only at Mach number 1.6. Free-stream Reynolds number, based on model length, ranged from 13.9 to 18.7 million for angles of attack from -4 to 12 deg and angles of sideslip of 0 and 6 deg. Test variables included canard angle, aileron angle, and inlet throat area. Previous tests on the Sandpiper and HAST missiles are reported in Refs. 1 through 5.

2.0 APPARATUS

2.1 TEST FACILITY

The Aerodynamic Wind Tunnel (4T) is a closed-loop, continuous flow, variable-density tunnel in which the Mach number can be varied from 0.1 to 1.3 and operated at Mach numbers 1.6 and 2.0 by placing nozzle inserts over the permanent sonic nozzle. At all Mach numbers, the stagnation pressure can be varied from 300 to 3700 psfa. The test section is 4 ft square and 12.5 ft long with perforated, variable porosity (0.5- to 10-percent open) walls. It is completely enclosed in a plenum chamber from which the air can be evacuated, allowing part of the tunnel airflow to be removed through the perforated walls of the test section. A more thorough description of the tunnel may be found in Ref. 6. A sketch of the test section wall details and the location of the test model in the test section is shown in Fig. 1.

2.2 TEST ARTICLE

Model photographs and details are shown in Figs. 2 and 3, respectively. The 0.25-scale model was fabricated from stainless steel and was furnished by the Beech Aircraft Corporation. The basic HAST I configuration is shown in Fig. 3a. The model fuselage was a 3.25-in.-diam cylinder with 3.5-cal tangent-ogive nose and a 0.69-cal boattail and was 50 in. in length. Attached to the fuselage were wings (Fig. 3b), vertical fins (Fig.

3c), canards (Fig. 3d), and ailerons (Fig. 3d). Canard deflection angles were -20, -10, 0, 10, and 20 deg, and the aileron could be positioned at 0, 5, and 10 deg. Both canard and aileron angles were set manually. Addition of the T5 pod (Fig. 3e), either of two afterbodies (Fig. 3e), inlet (Figs. 3f and g), launch pins (Fig. 3h), pitot tube (Fig. 3i), and 12 antennas (Figs. 3h through j) completed the configuration.

Capture area ratio of the HAST I inlet was varied by using interchangeable orifice plates with throat areas from 0 to approximately 0.6 in.² (Fig. 3g). Three total pressure orifices and four static pressure orifices were located in the inlet (Fig. 3g) and calibration of the inlet was accomplished in the AEDC von Kármán Gas Dynamics Facility (VKF).

The HAST II configurations were transformed from the basic HAST I configuration as follows: First, all antennas, pitot tube, launch pins, T5 pod, HAST I inlet and afterbody were removed. Then, one of two raceways (Fig. 3k) was attached to the bottom of the model, one of three ramburner tailpipes (Fig. 3l) was attached to the base of the model and finally the HAST II inlet system (Fig. 3m) was added. A complete listing of both the HAST I and II model configurations is shown in Table 1.

2.3 INSTRUMENTATION

Aerodynamic forces and moments on the model were measured with a six-component, moment-type, internal strain-gage balance supplied and calibrated by the AEDC-PWT. Inlet pressures and model base pressures were measured with 15- and 5-psid transducers, respectively.

3.0 TEST PROCEDURE

3.1 TEST CONDITIONS AND DESCRIPTION

A complete test summary and the wind tunnel test conditions are given in Tables 2 and 3. Steady-state force data along with inlet pressure data were obtained at nominal free-stream Mach numbers of 0.5, 0.8, 0.95, 1.1, 1.3, and 1.6. Tunnel conditions were held constant at each Mach number while pitch angle was varied and data recorded at each selected angle. The pitch range was from -4 to 12 deg at angles of sideslip of 0 and 6 deg. Test variables included canard angles between -20 and 20 deg, aileron angles of 0, 5, and 10 deg, inlet throat areas from 0 to 0.6 in.², and several model configurations.

3.2 DATA REDUCTION

Force and moment data from the main balance were reduced to coefficient form in the body axes system. The moment reference was 57 percent of the model length. A sketch of the coordinate system showing positive directions of all forces and moments along with the positive directions for the canard and aileron deflection angles is presented in Fig. 4.

The HAST I inlet free-stream capture area ratio (A_o/A_c) was defined as

$$A_o/A_c = \frac{(p_{sp})}{p_\infty} \frac{(A_p)}{A_c} \frac{f(M_p)}{f(M_\infty)} \quad (1)$$

where p_{sp} is the inlet plenum static pressure, p_∞ is the free-stream static pressure, A_p is the inlet plenum area, A_c is the inlet cowl area, $f(M_p)$ is the plenum mass flow function from inlet calibration and given in Fig. 5, and $f(M_\infty)$ is the free-stream mass flow function for isentropic flow, as shown in Fig. 5, and defined as

$$f(M_\infty) = gM_\infty \left(\frac{\gamma}{R} \right)^{1/2} \left(1 + \frac{\gamma-1}{2} M_\infty^2 \right)^{1/2}$$

where g is the acceleration due to gravity, M_∞ is the free-stream Mach number, γ is the specific heat ratio, and R is the universal gas constant.

The internal axial-force coefficient of the inlet ($C_{A_{i,e}}$) can then be computed by the relation (Ref. 7)

$$C_{A_{i,e}} = \frac{-2(A_e/S)}{\gamma M_\infty^2} \left[\frac{p_{s_e}}{p_\infty} (1 + \gamma M_e^2) - 1 \right] + 2(A_o/S) \quad (2)$$

where A_e is the inlet exit area, S is the reference area, p_{s_e} is the inlet exit static pressure, and M_e is the inlet exit Mach number.

3.3 PRECISION OF MEASUREMENTS

Uncertainties in the basic tunnel parameters, free-stream total pressure (p_t), free-stream total temperature (T_t), and M_∞ were estimated from repeat calibrations of the instrumentation and from repeatability and uniformity of the test section flow during

tunnel calibration. These uncertainties were then used to estimate uncertainties in other free-stream properties, using the Taylor series method of error propagation (Ref. 8) (q_∞ is the free-stream dynamic pressure, and Re_l is the free-stream Reynolds number based on model length):

M_∞	Uncertainty, percent					
	M_∞	p_t	T_t	p_∞	q_∞	Re_l
0.5	±0.4	±0.1	±0.4	±0.2	±0.7	±0.6
0.8	±0.3	±0.1	±0.4	±0.2	±0.4	±0.5
0.95	±0.3	±0.1	±0.4	±0.4	±0.3	±0.5
1.1	±0.6	±0.1	±0.4	±0.8	±0.4	±0.5
1.3	±1.1	±0.1	±0.4	±2.0	±0.3	±0.5
1.6	±0.6	±0.1	±0.4	±1.2	±0.2	±0.6

Model attitude corrections were made for model-balance deflections under air load, but no corrections were made for any test section flow inclination or tunnel wall interference effects. The precision of the angles of attack and sideslip (α and β) is estimated to be ±0.1 deg.

The balance uncertainties, based on a 95-percent confidence level, were combined with uncertainties in the tunnel parameters, assuming a Taylor series error propagation, to estimate the precision of the aerodynamic coefficients. The maximum estimated uncertainties are given in the following table:

Coefficient	Uncertainty					
	$M_\infty = 0.5$	0.8	0.95	1.1	1.3	1.6
C_N	±0.068	±0.039	±0.039	±0.042	±0.034	±0.028
C_m	±0.005	±0.003	±0.003	±0.004	±0.004	±0.003
C_Y	±0.015	±0.009	±0.009	±0.009	±0.008	±0.006
C_n	±0.003	±0.002	±0.002	±0.002	±0.001	±0.001
C_l	±0.003	±0.002	±0.002	±0.002	±0.002	±0.002
$C_{A,F}$	±0.004	±0.002	±0.003	±0.005	±0.006	±0.004

4.0 RESULTS AND DISCUSSION

4.1 HAST I INLET CHARACTERISTICS

Variations of the inlet pressures and internal axial-force characteristics with capture area ratio, angle of attack (α), angle of sideslip (β), canard deflection angle (δ_c), Mach number, and model configuration are presented in Figs. 6 through 11, respectively. As would be expected, the larger variations in the inlet performance parameters resulted from changes in A_o/A_c (Fig. 6) and free-stream Mach number (Fig. 10). As shown in Fig. 10, agreement between the present and Ref. 5 data was quite good, and total pressure measurements in the plenum agreed well with the predicted pressures downstream of a normal shock wave (Ref. 9). Some variations in the inlet characteristics were noted with changing angle of attack (Fig. 7), angle of sideslip (Fig. 8), canard deflection (Fig. 9), and model configuration (Fig. 11), but these were in most cases small.

The effects of capture area ratio on the missile normal-force (C_N), pitching-moment (C_m), and axial-force ($C_{A,F}$) characteristics are shown in Figs. 12 and 13. As may be seen, varying A_o/A_c had little effect on C_N and C_m (Fig. 12) at all Mach numbers and little effect on the axial-force coefficients at $M_\infty = 0.5$ and 0.8 . However, at $M_\infty \geq 0.95$, forebody axial-force coefficient ($C_{A,F}$) decreased approximately 6 percent as A_o/A_c increased from 0 to ≈ 0.8 (Fig. 13).

4.2 BASIC HAST I AERODYNAMIC CHARACTERISTICS

The effects of canard deflection on the normal-force, pitching-moment, and axial-force coefficients at an inlet throat area (A_1) of 0.505 in.^2 are presented in Figs. 14 through 18 for Mach numbers 0.8, 0.95, 1.1, 1.3, and 1.6, respectively. Deflection of the canards produced only small changes in C_N over the angle-of-attack range but large changes in both C_m and $C_{A,F}$ were noted. The preceding data are summarized in Figs. 19 through 21. As shown in Fig. 19, the addition of the antennas slightly increased the slopes of both the normal-force and pitching-moment curves (compare configurations 2 and 3), while differences in the normal-force derivative (C_{N_α}) and pitching-moment derivative (C_{m_α}) were small for the two afterbody configurations (compare configurations 1 and 2). Deflection of the canards (Fig. 20) produced a significant increase in the axial-force coefficient, whereas addition of the antennas resulted in about a 30-percent increase in $C_{A,F}$ at transonic Mach numbers. $C_{A,F}$ was also slightly larger for the larger (T3) afterbody of configuration 1. Differences in canard effectiveness and trim angle (Fig. 21) for the two afterbody configurations or with the addition of the antennas were small. In general, agreement between the present data and the Ref. 5 data was quite good (Figs. 19 through

21). Direct comparison of the present data with the Refs. 1 and 2 data are not valid because of configuration differences. However, the data trends and levels are similar as would be expected.

The effects of canard deflection on the side-force (C_Y), yawing-moment (C_n), and rolling-moment (C_l) coefficients for $A_t = 0.505 \text{ in.}^2$ are shown in Figs. 22 through 26 for Mach numbers 0.8, 0.95, 1.1, 1.3, and 1.6, respectively. The data on configuration 2 (shown) were typical of the data obtained on both configurations 1 and 3. At $\beta = 0$, little change in the C_Y , C_n , or C_l data occurred with changes in canard deflection angle or angle of attack. At $\beta = 6 \text{ deg}$, deflection of the canards generally resulted in small variations in C_Y and C_n . However, for the C_l data at $\beta = 6 \text{ deg}$ and low angles of attack, a significant increment in rolling moment was produced by a deflection of the canards that was opposite in sign to the canard deflection angle.

The effects of aileron deflection on C_Y , C_n , and C_l for $A_t = 0.505 \text{ in.}^2$ are presented for configuration 2 in Figs. 27 through 31 for Mach numbers 0.8, 0.95, 1.1, 1.3, and 1.6, respectively. Deflection of the ailerons did not significantly affect either C_Y or C_n at angle of attack or sideslip. However, a positive aileron deflection angle (δ_a) produced a positive increment in rolling moment as would be expected. A sharp decrease in aileron effectiveness (Fig. 32) was evident at $M_\infty = 0.95$, and the present data showed reasonable agreement with the data of Refs. 1, 2, 3, and 5.

The effects of sideslip angle on the side-force, yawing-moment, and rolling-moment coefficients are illustrated for configuration 2 in Figs. 33 through 37 at Mach numbers 0.8, 0.95, 1.1, 1.3, and 1.6, respectively. As would be expected, a positive β increment resulted in a negative side force and positive yawing moment over the angle-of-attack range. Increasing β to 6 deg also introduced a negative slope to the C_l versus α curve. However, this was to be expected from the dihedral effect of sideslip on swept wings.

4.3 HAST I COMPONENT BUILDUP CHARACTERISTICS

The effects of individual missile components on the longitudinal stability derivatives and axial-force coefficients at $\alpha = 0$ are presented in Fig. 38. Buildup was begun from the clean ogive cylinder and the effects of each component as it was added are evident. It is interesting to note that in a comparison of the clean ogive cylinder to the full HAST I configuration (configurations 18 to 2) at $M_\infty = 1.1$, C_{N_α} was increased by a factor of approximately 16, C_{m_α} was changed from unstable to very stable trim, and $C_{A,F}$ was increased by a factor of approximately 3. As may be seen, the present data agreed quite well with the Ref. 5 data.

4.4 HAST II AERODYNAMIC AND INLET CHARACTERISTICS

The effects of the missile components on the HAST II longitudinal stability and axial-force characteristics are presented in Fig. 39. Comparison of the data for the two raceways (Fig. 39a) showed configuration 21, with the modified HAST I raceway, to have a slightly higher trim angle and axial force. Increasing the size of the ramburner tailpipes (Fig. 39b) increased the magnitude of C_{m_a} and C_A but had little effect on $C_{A,F}$. Addition of the inlet (Fig. 39c, configuration 26) resulted in increased C_N , C_A , and $C_{A,F}$ along with a reduction in trim angle of attack (α_t). The small differences in the side-force, yawing-moment, and rolling-moment coefficients (Fig. 40) should probably not be attributed to component effects but rather to model asymmetries. The effects of angle of attack on the inlet exit total pressure distributions (Fig. 41) were generally small except at $\theta = 180$ deg.

5.0 CONCLUDING REMARKS

The aerodynamic and inlet characteristics of 0.25-scale models of the HAST I and II missiles were investigated at Mach numbers from 0.5 to 1.6. Based on the test results, the following comments can be made:

1. The more significant variation in the inlet performance parameters resulted from changes in capture area ratio and free-stream Mach number.
2. Deflection of the canards had significant effects on pitching-moment and axial-force coefficients, and model trim angle of attack at zero sideslip. For sideslip greater than zero, canard deflection also had a significant effect on rolling-moment coefficient.
3. Addition of the antennas to the clean configuration increased axial force by approximately 30 percent.
4. Aileron deflection had significant effects only on rolling-moment coefficient.

REFERENCES

1. White, Warren E. "Investigation of the Static Stability and Store Separation Characteristics of the Sandpiper Target Missile at Transonic Mach Numbers." AEDC-TR-70-97 (AD868795), May 1970.

2. Carman, J. B. "Static Stability and Inlet Characteristics of the HAST Missile at Transonic Mach Numbers." AEDC-TR-71-178 (AD887776L), September 1971.
3. Jones, J. H. "Aerodynamic Characteristics of the HAST Missile at Mach Numbers 2.25, 3, and 4." AEDC-TR-72-6 (AD890591L), January 1972.
4. Knox, E. C. and Carter, L. D. "Heat-Transfer Tests Using Thermographic Phosphor Paint on the High Altitude Supersonic Target (HAST) Missile at Mach Number 4." AEDC-TR-73-20 (AD907690L), February 1973.
5. Best, J. T., Jr. and Rhudy, R. W. "Static Stability and Drag Characteristics of the HAST Missile at Mach Numbers 2.25, 3, and 4." AEDC-TR-74-24.
6. Test Facilities Handbook (Ninth Edition). "Propulsion Wind Tunnel Facility, Vol. 4." Arnold Engineering Development Center, July 1971.
7. Zucrow, M. J. "Aircraft and Missile Propulsion , Volume II." John Wiley & Sons, Inc., New York, New York, 1958, pp. 360-367.
8. Beers, Yardley. Introduction to the Theory of Error. Addison-Wesley Publishing Company, Inc., Reading, Massachusetts, 1957, pp. 26-36.
9. Ames Research Staff. "Equations, Tables, and Charts for Compressible Flow." NACA Report 1135, 1953.

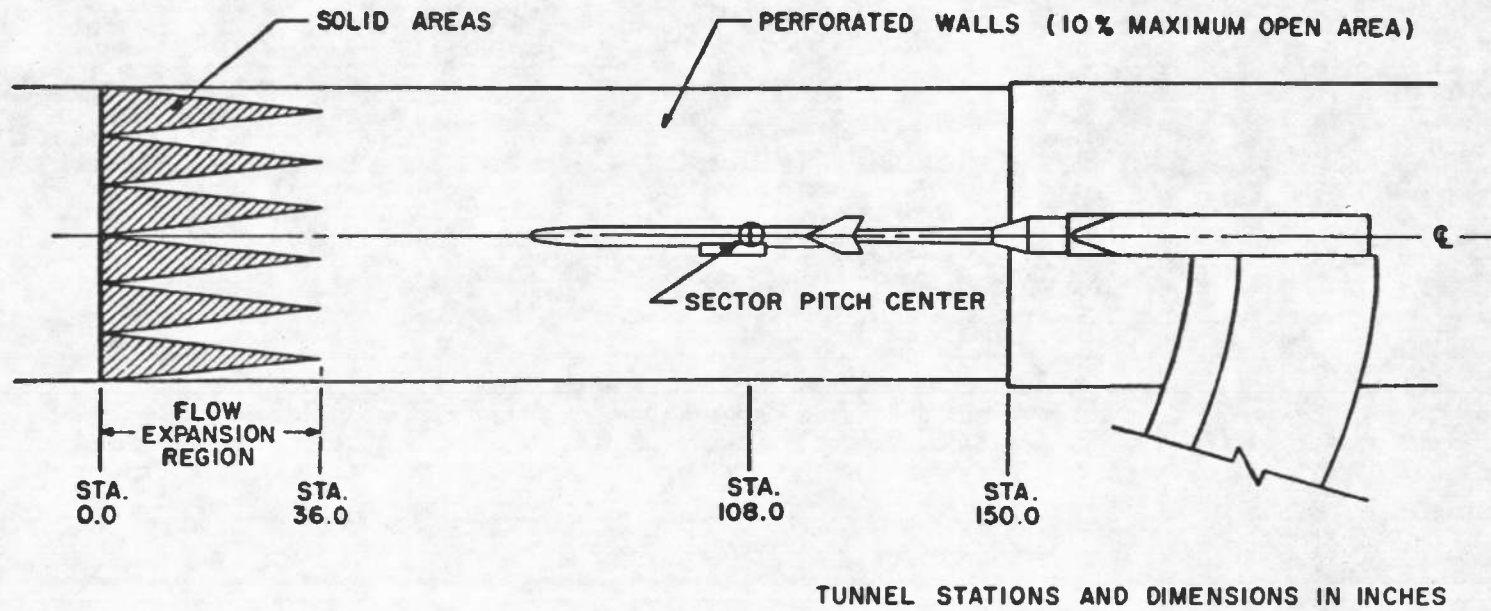
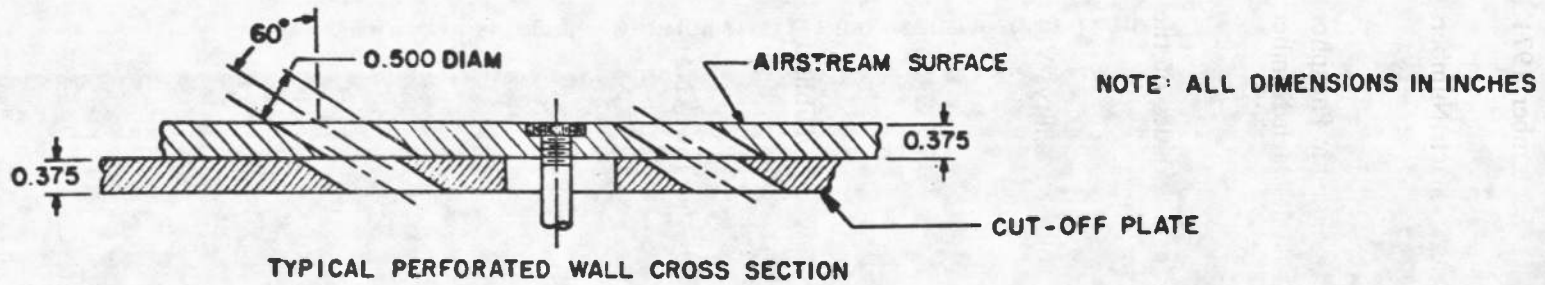


Figure 1. Schematic of Tunnel 4T test section showing model location.

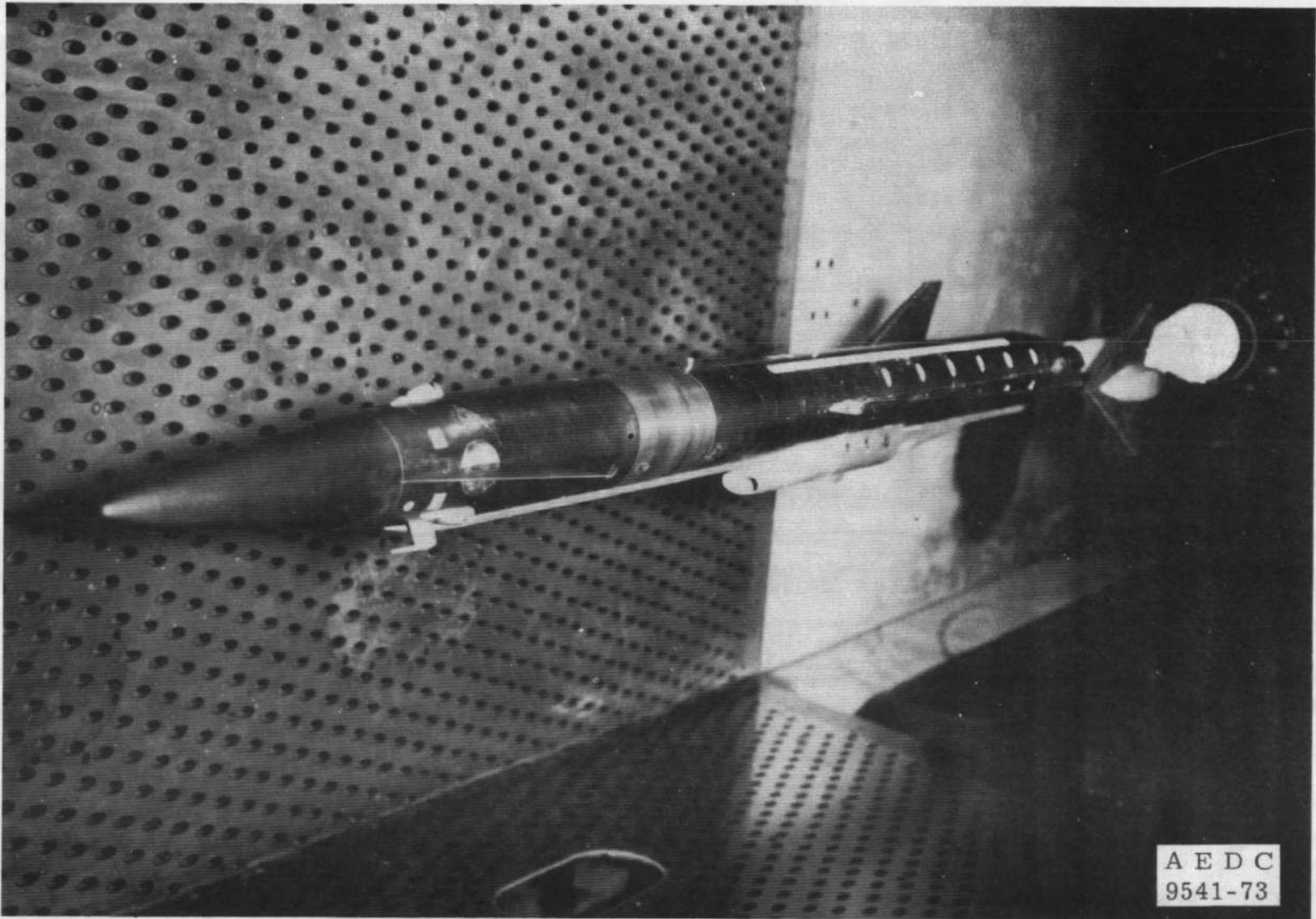
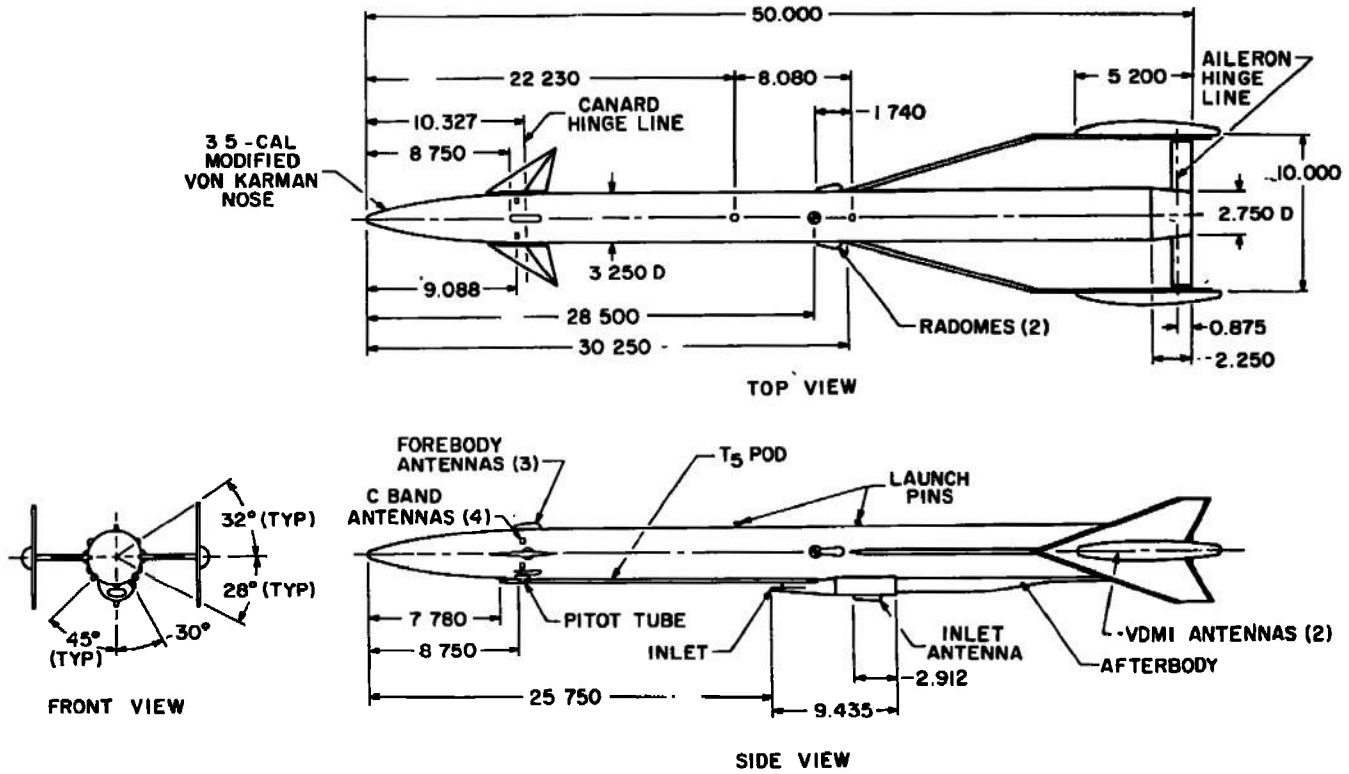
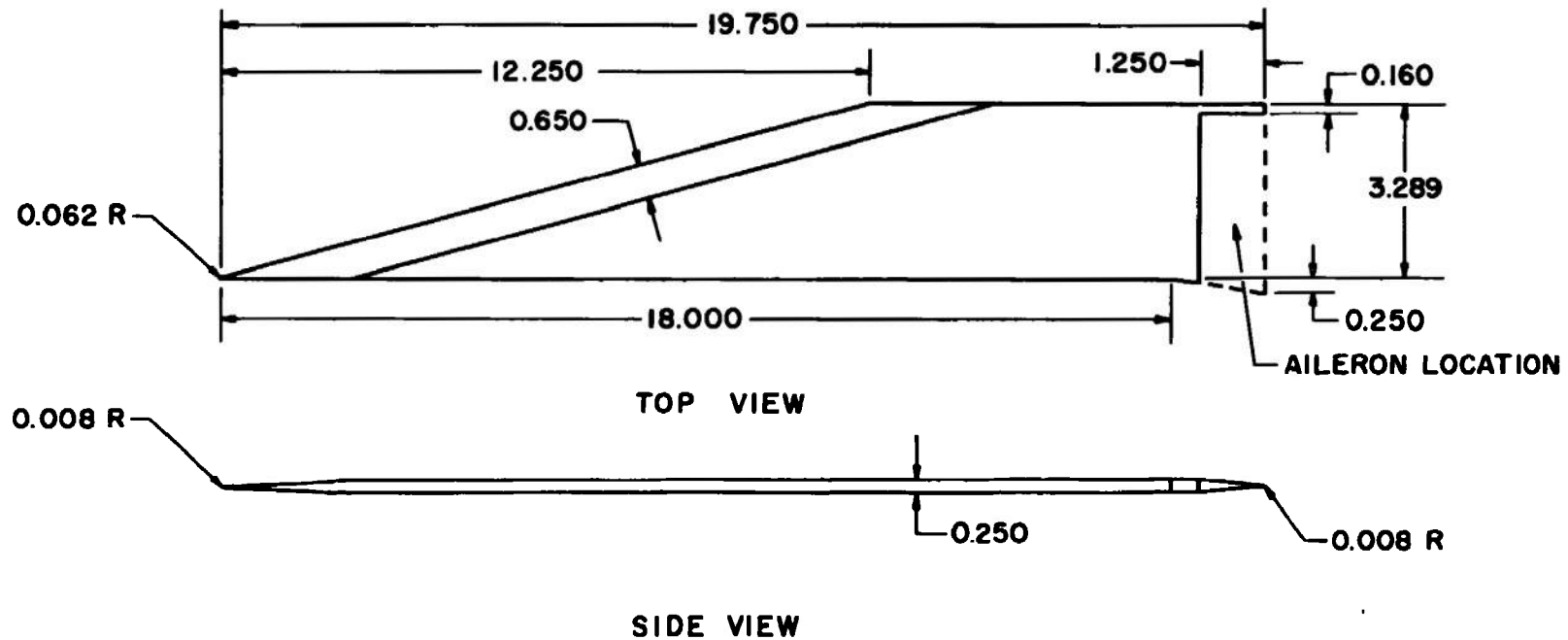


Figure 2. Photograph showing HAST I model installed in Tunnel 4T.



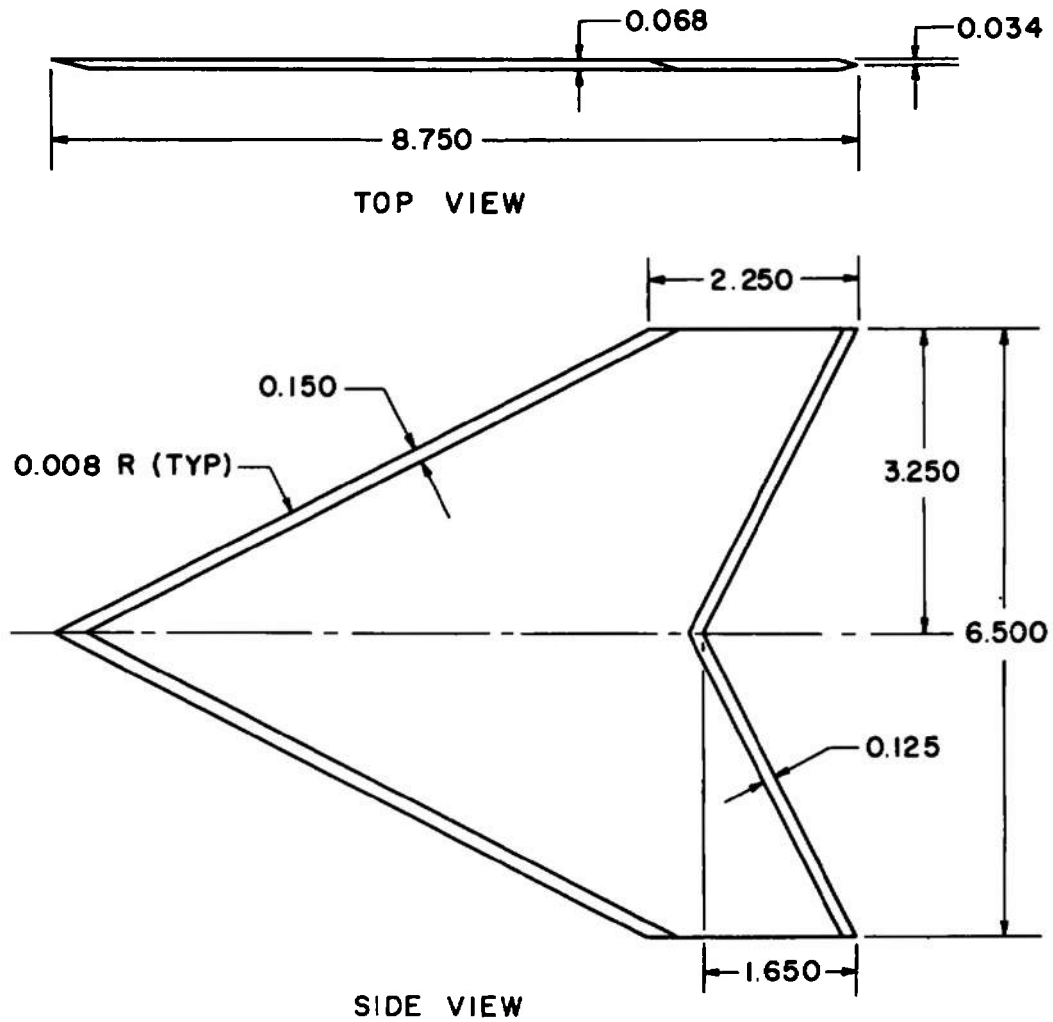
ALL DIMENSIONS IN INCHES
 ⊙ MOMENT REFERENCE
 REF. AREA = 0.0576 ft²
 REF LENGTH = 4.167 ft

a. Basic Hast I configuration
 Figure 3. Model details.



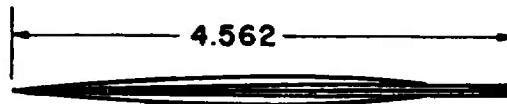
ALL DIMENSIONS IN INCHES

b. Wings
Figure 3. Continued.

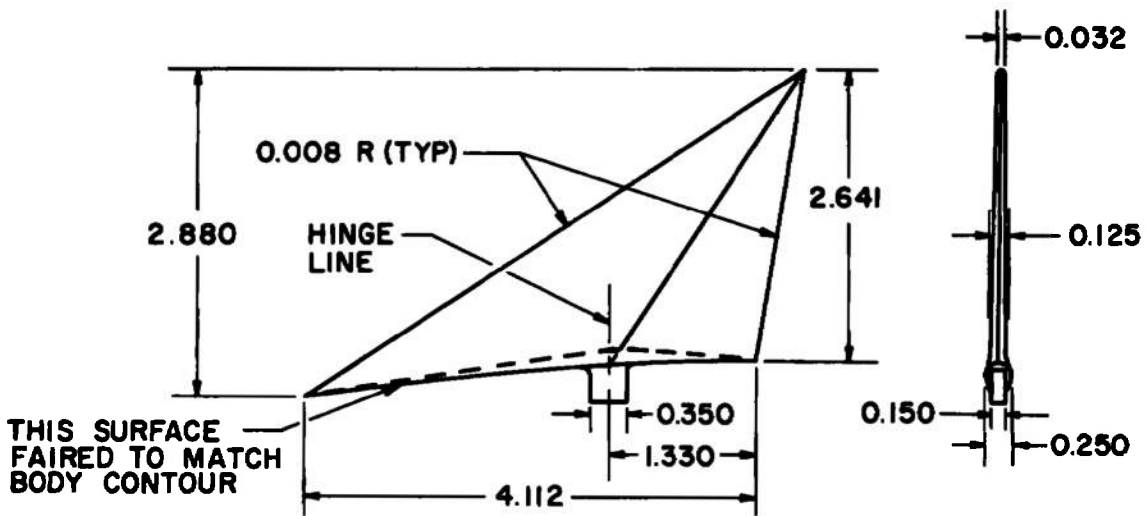


ALL DIMENSIONS IN INCHES

c. Vertical fins
Figure 3. Continued.



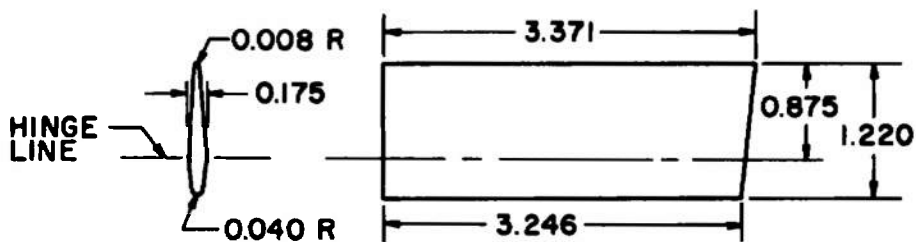
SIDE VIEW



TOP VIEW

REAR VIEW

CANARDS



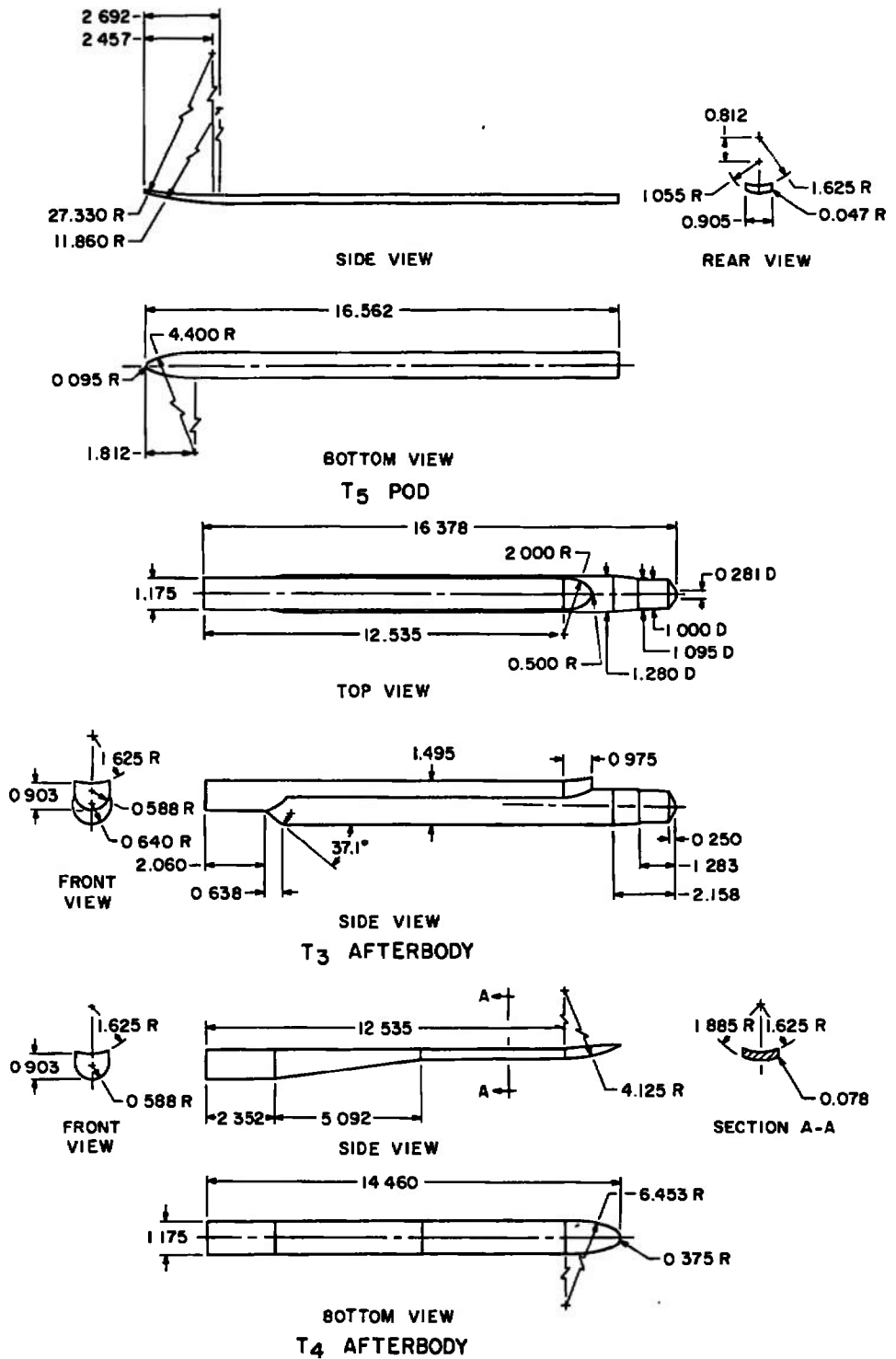
END VIEW

TOP VIEW

AILERONS

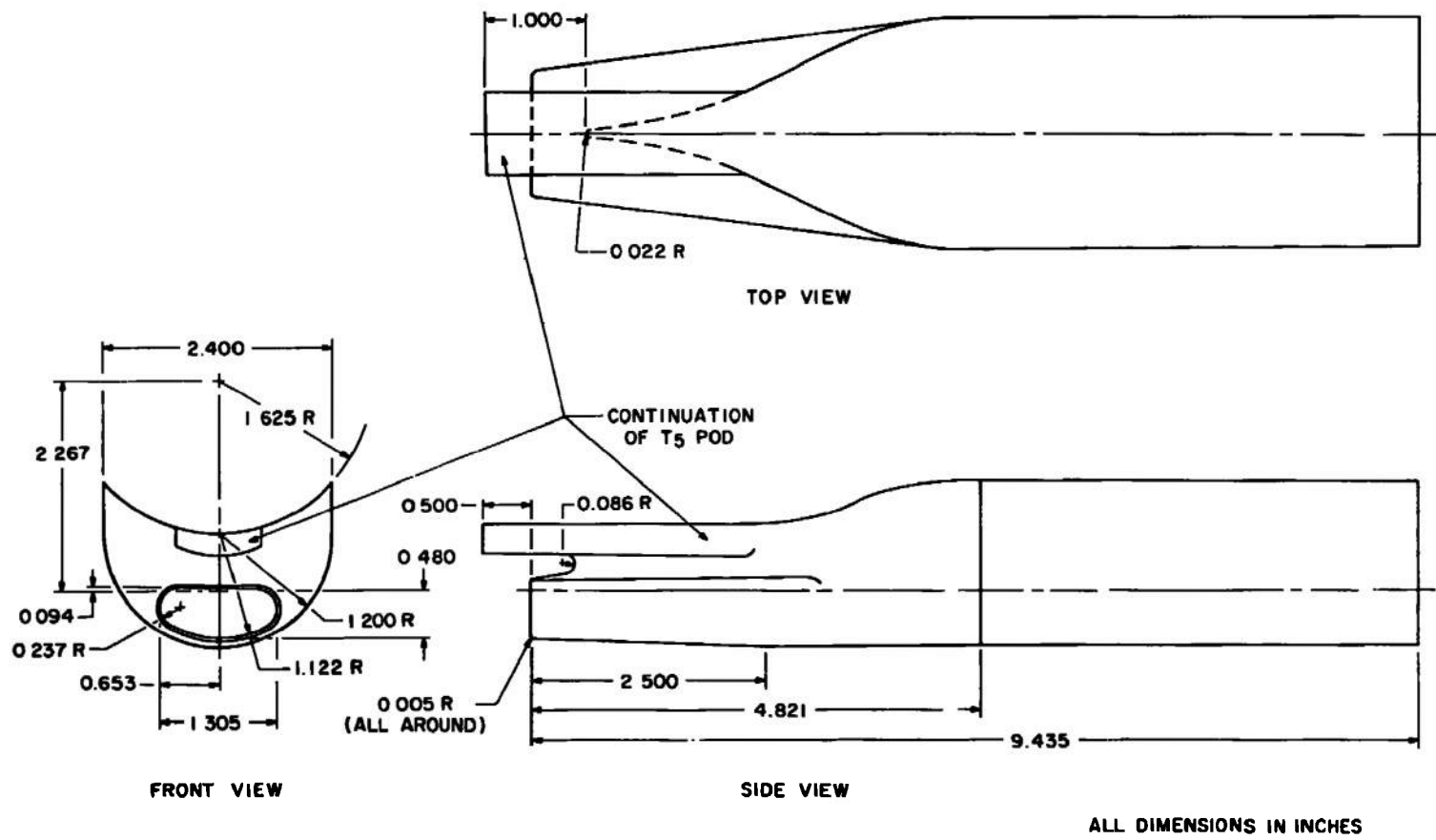
ALL DIMENSIONS IN INCHES

d. Canards and ailerons
Figure 3. Continued.

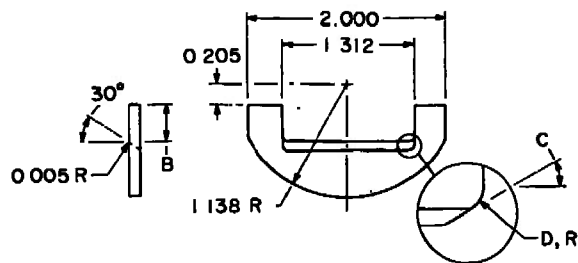


ALL DIMENSIONS IN INCHES

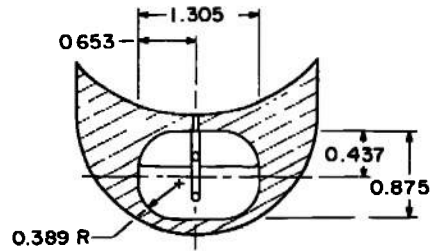
e. HAST I T₅ pod and afterbodies
Figure 3. Continued.



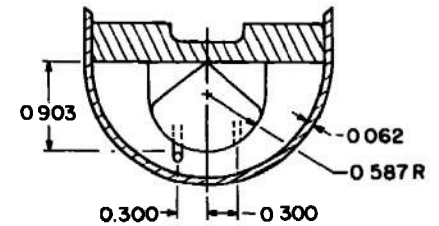
f. HAST I inlet (external)
Figure 3. Continued.



SIDE VIEW REAR VIEW
ORIFICE PLATES

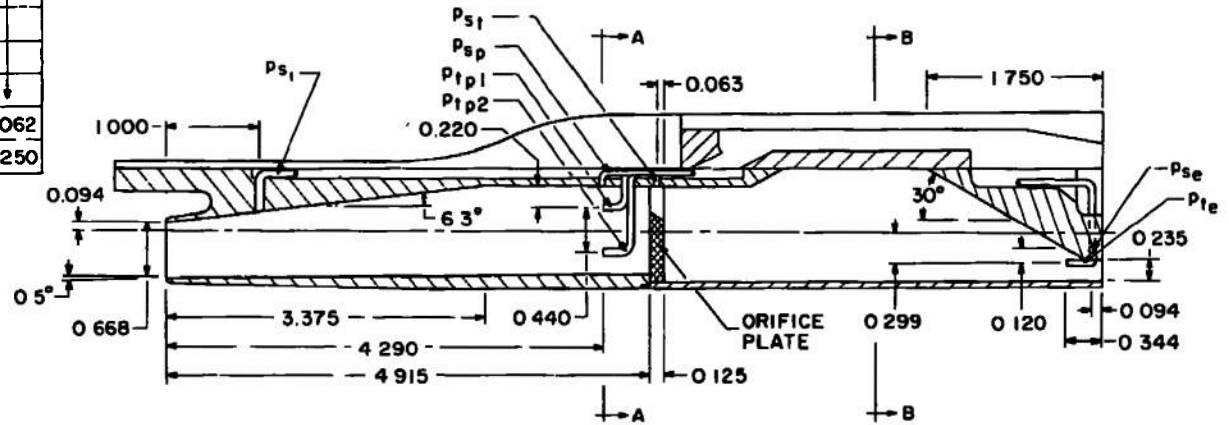


SECTION A-A



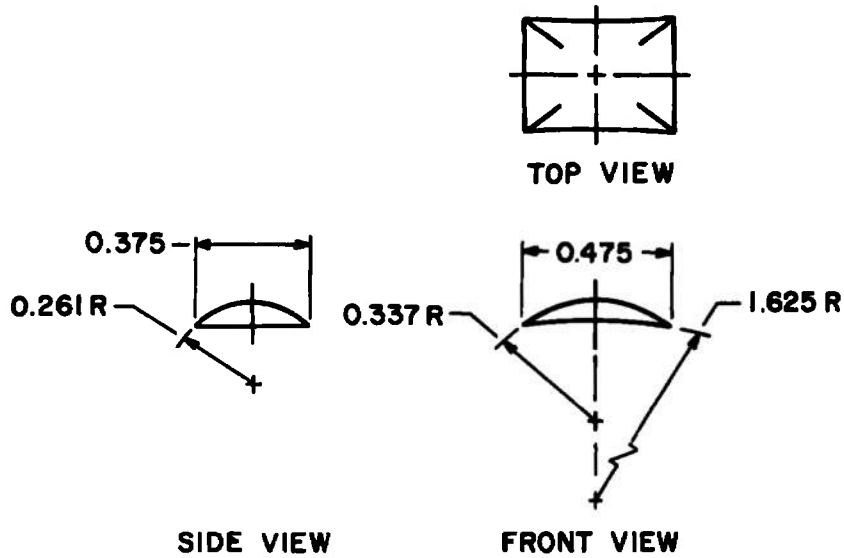
SECTION B-B

NO	A_t, in^2	B, in	C, deg	D, in
1	0.1011	0.112	0	0.032
2	0.2015	0.200		
3	0.3039	0.282		
4	0.4046	0.360		
5	0.5053	0.437		
6	0.6066	0.515		
7	0.7073	0.593		
8	0.8097	0.675	30	0.062
9	0.9101	0.763		0.250

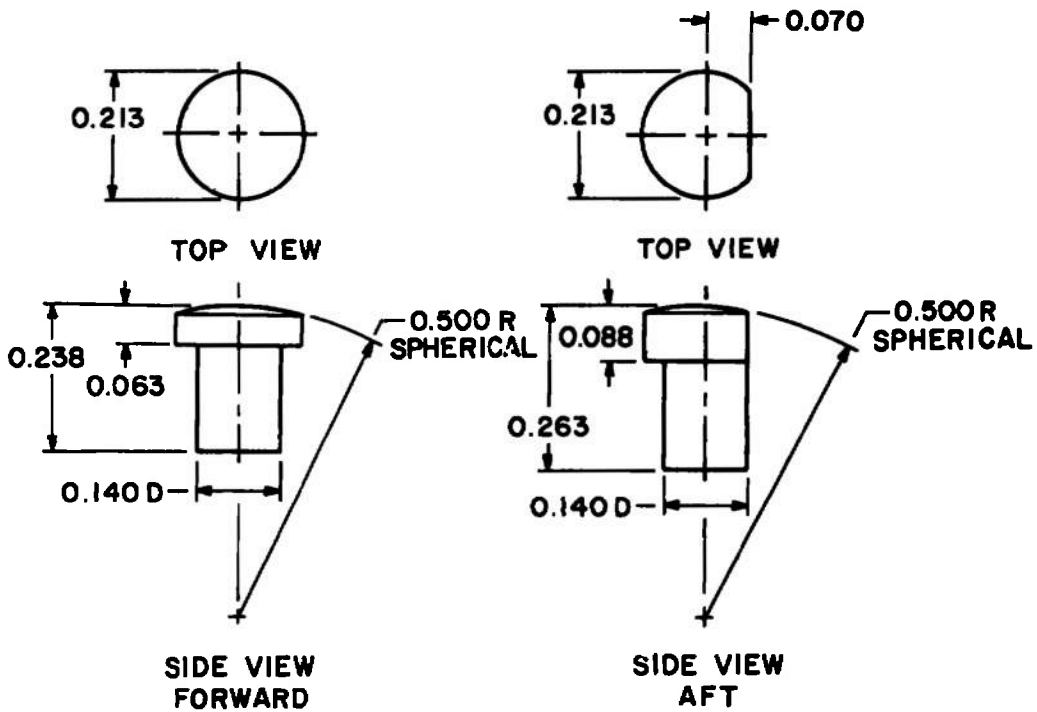


ALL DIMENSIONS IN INCHES

g. HAST I inlet (internal)
Figure 3. Continued.



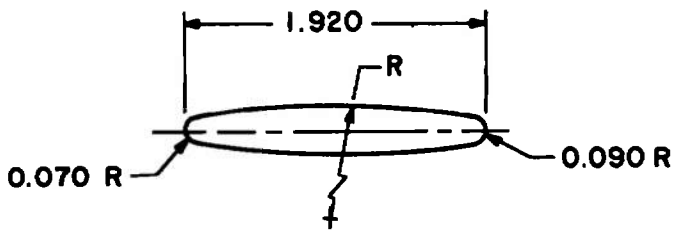
C BAND ANTENNAS



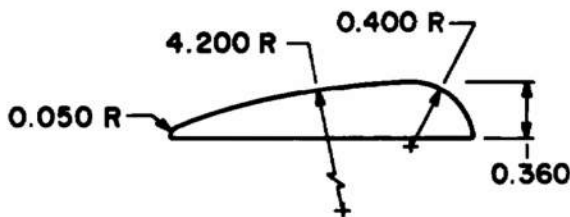
LAUNCH PINS

ALL DIMENSIONS IN INCHES

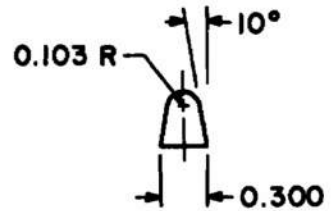
h. HAST I C-band antennas and launch pins
Figure 3. Continued.



TOP VIEW

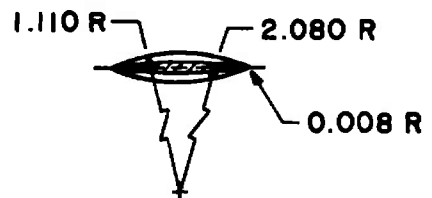


SIDE VIEW

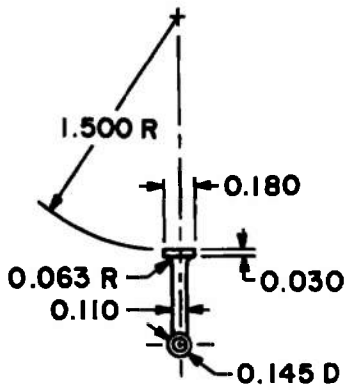


REAR VIEW

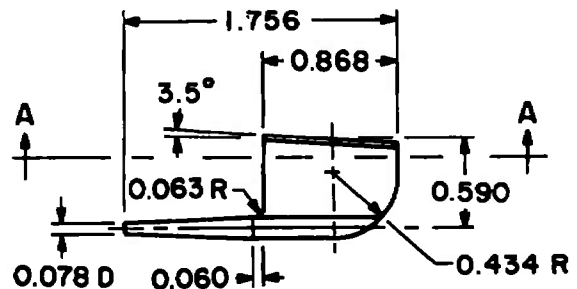
FOREBODY AND INLET ANTENNA



SECTION A-A



FRONT VIEW

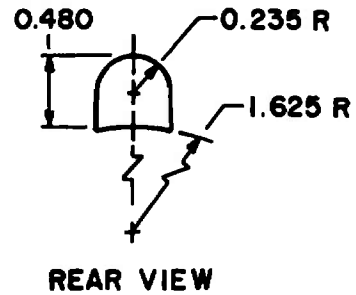
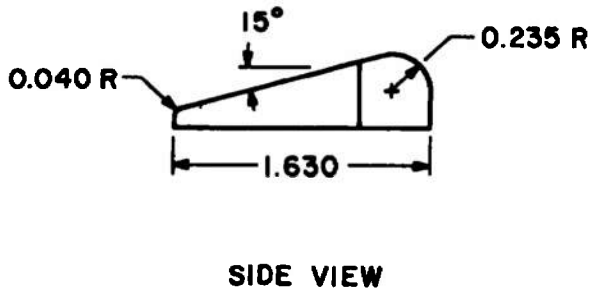
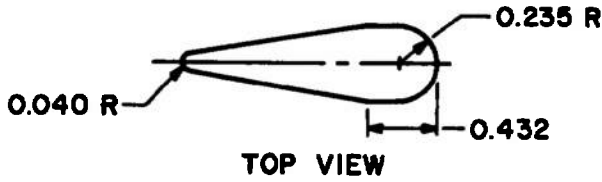


SIDE VIEW

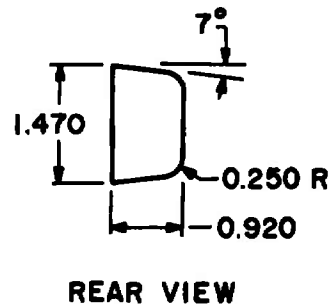
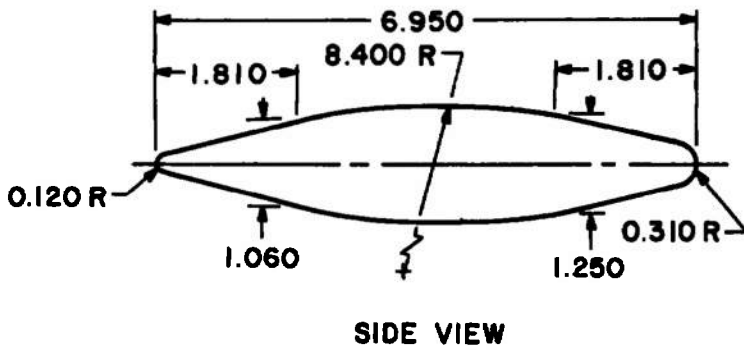
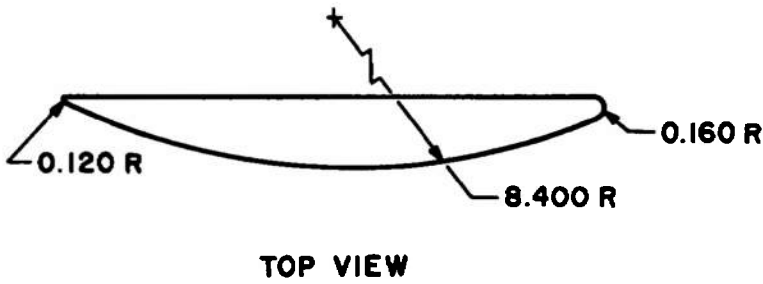
PITOT TUBE

ALL DIMENSIONS IN INCHES

- i. HAST I forebody (and inlet) antennas and pitot probe
Figure 3. Continued.



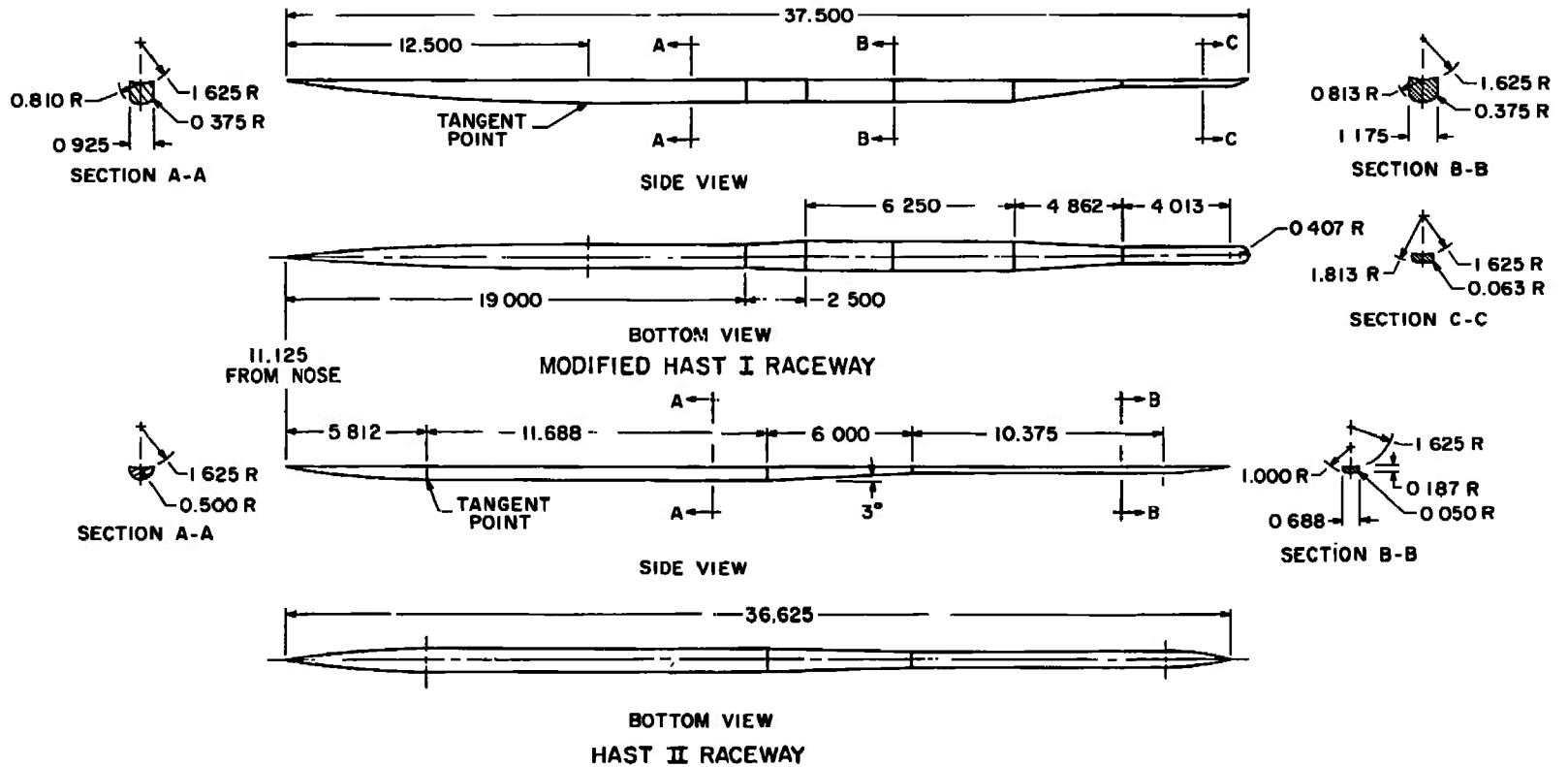
RADOME



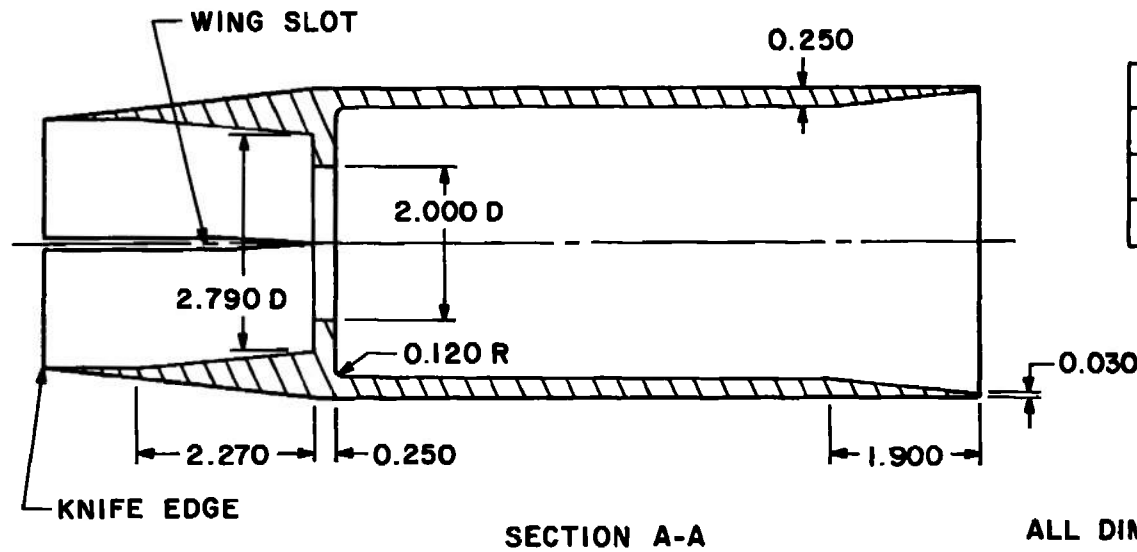
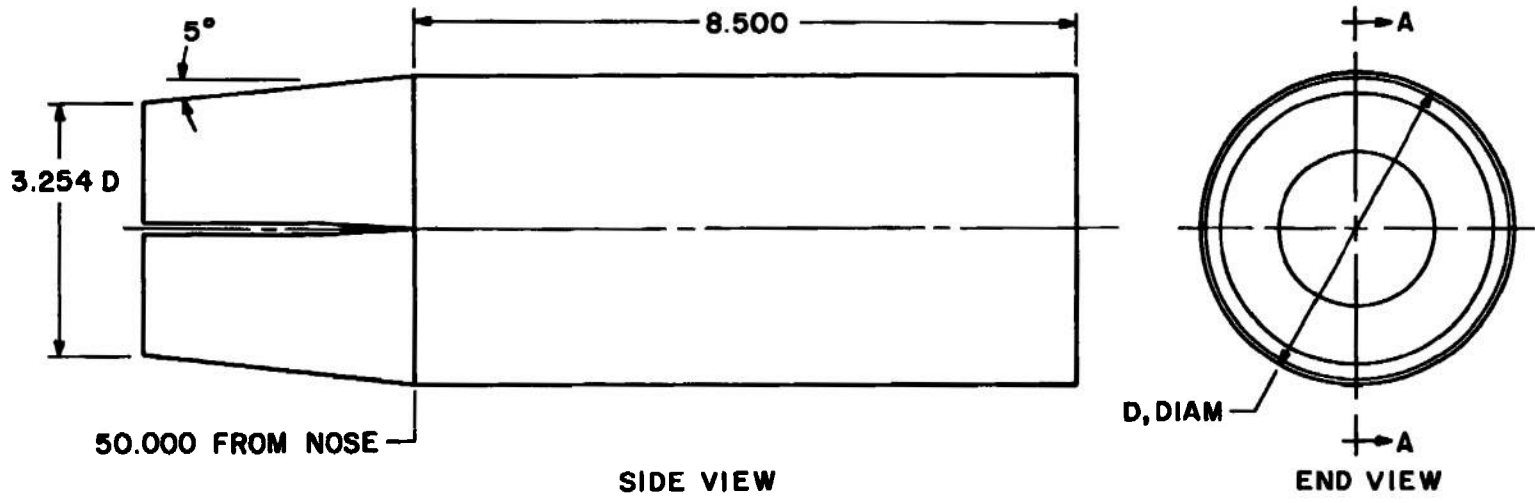
VDMI ANTENNA

ALL DIMENSIONS IN INCHES

- j. HAST I wing root radomes and VDMI antennas
Figure 3. Continued.



k. HAST II raceways
Figure 3. Continued.

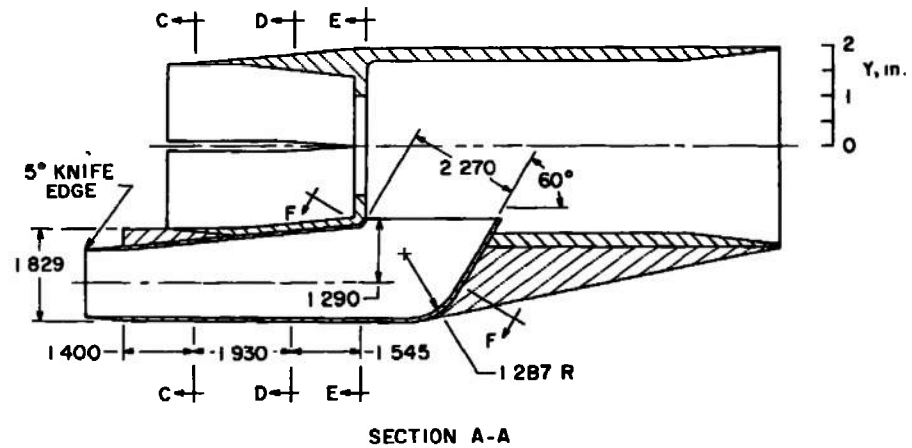
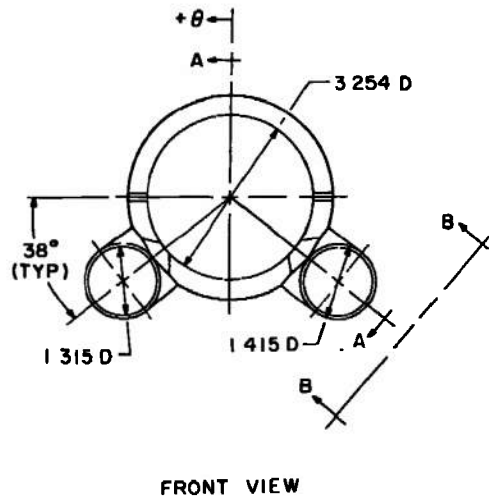
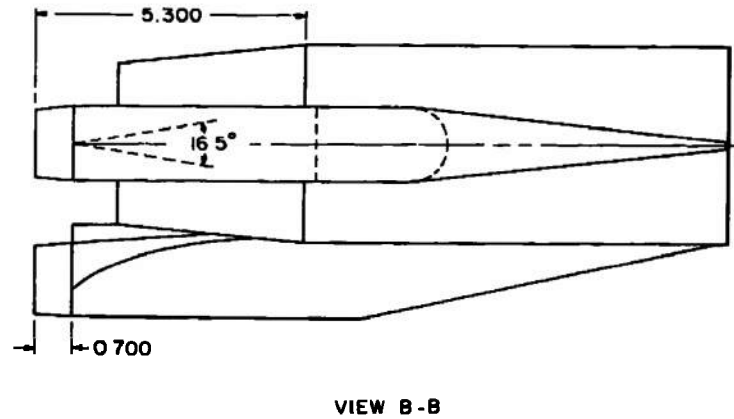
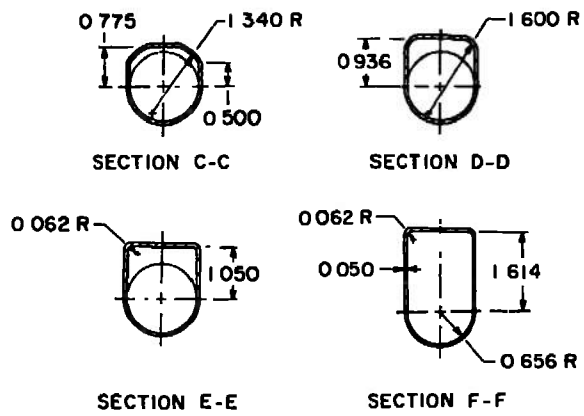


RAMBURNER	D, in.
1	3.875
2	3.625
3	4.125

SECTION A-A

ALL DIMENSIONS IN INCHES

2. HAST II ramburner tailpipes
Figure 3. Continued.



ALL DIMENSIONS IN INCHES

m. HAST II inlet
Figure 3. Concluded.

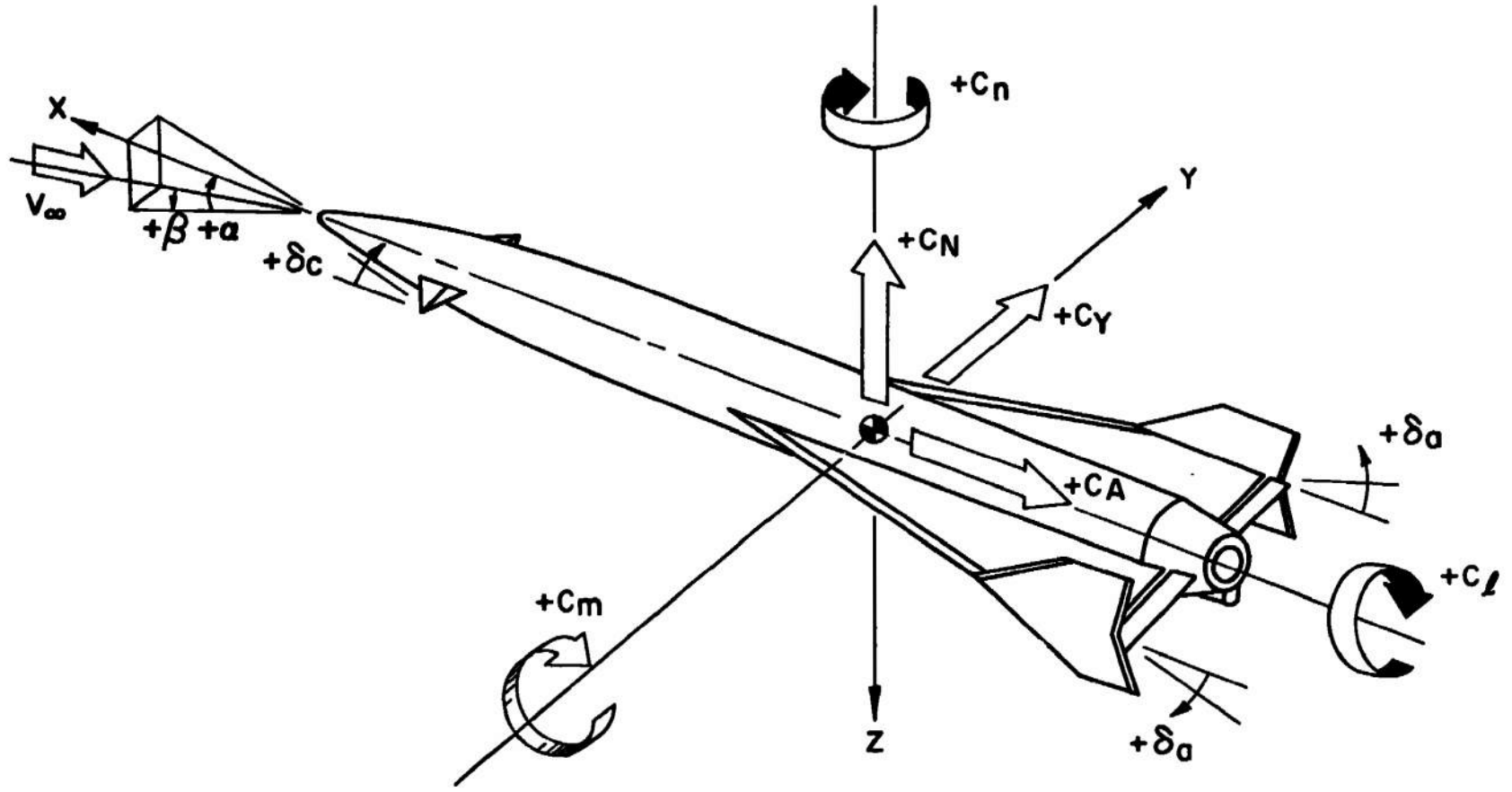


Figure 4. Sign convention and coordinate system.

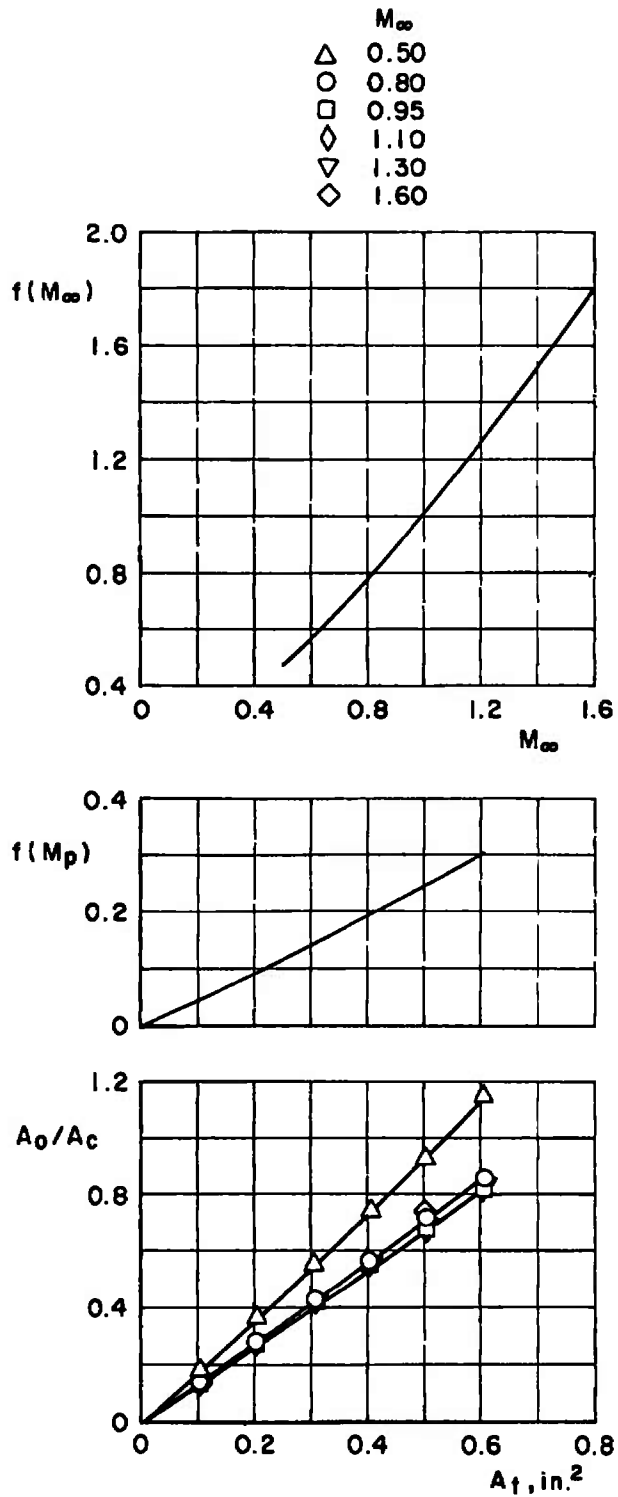


Figure 5. HAST I inlet mass flow functions, capture area ratios and throat areas.

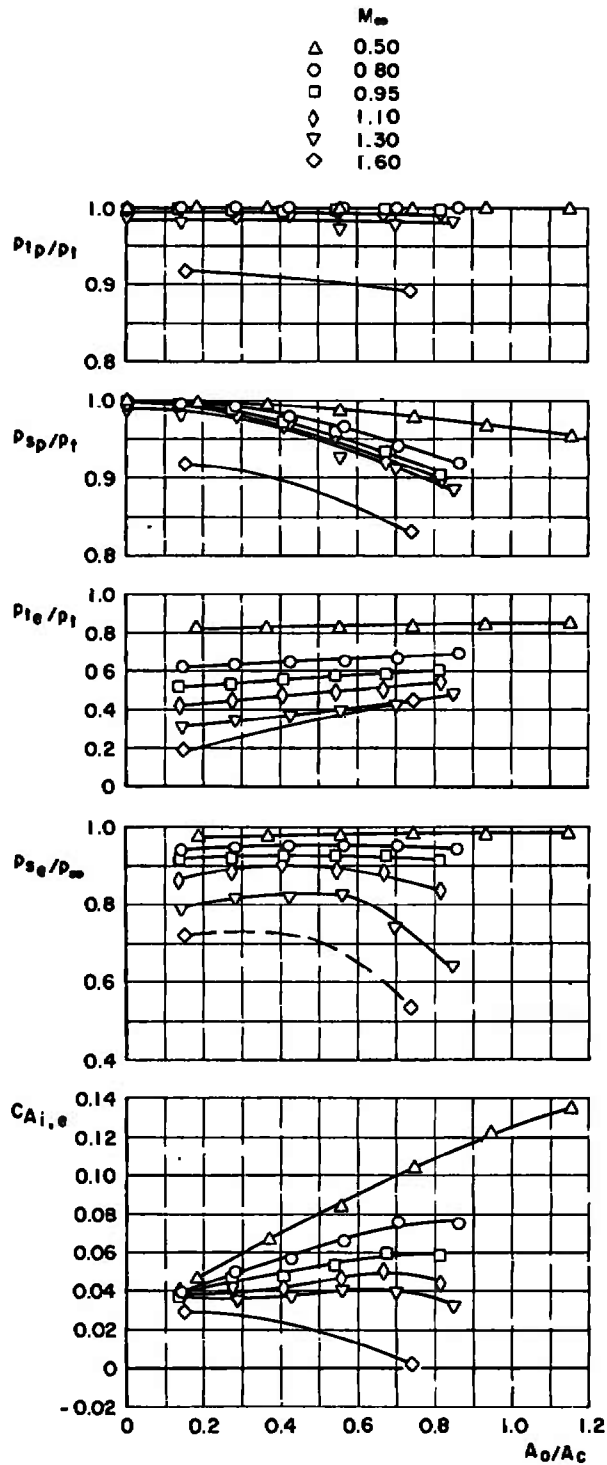


Figure 6. Variation of the inlet plenum pressures, exit pressures and axial-force coefficients with capture area ratio, configuration 2, $\delta_c = \delta_a = \alpha = \beta = 0$.

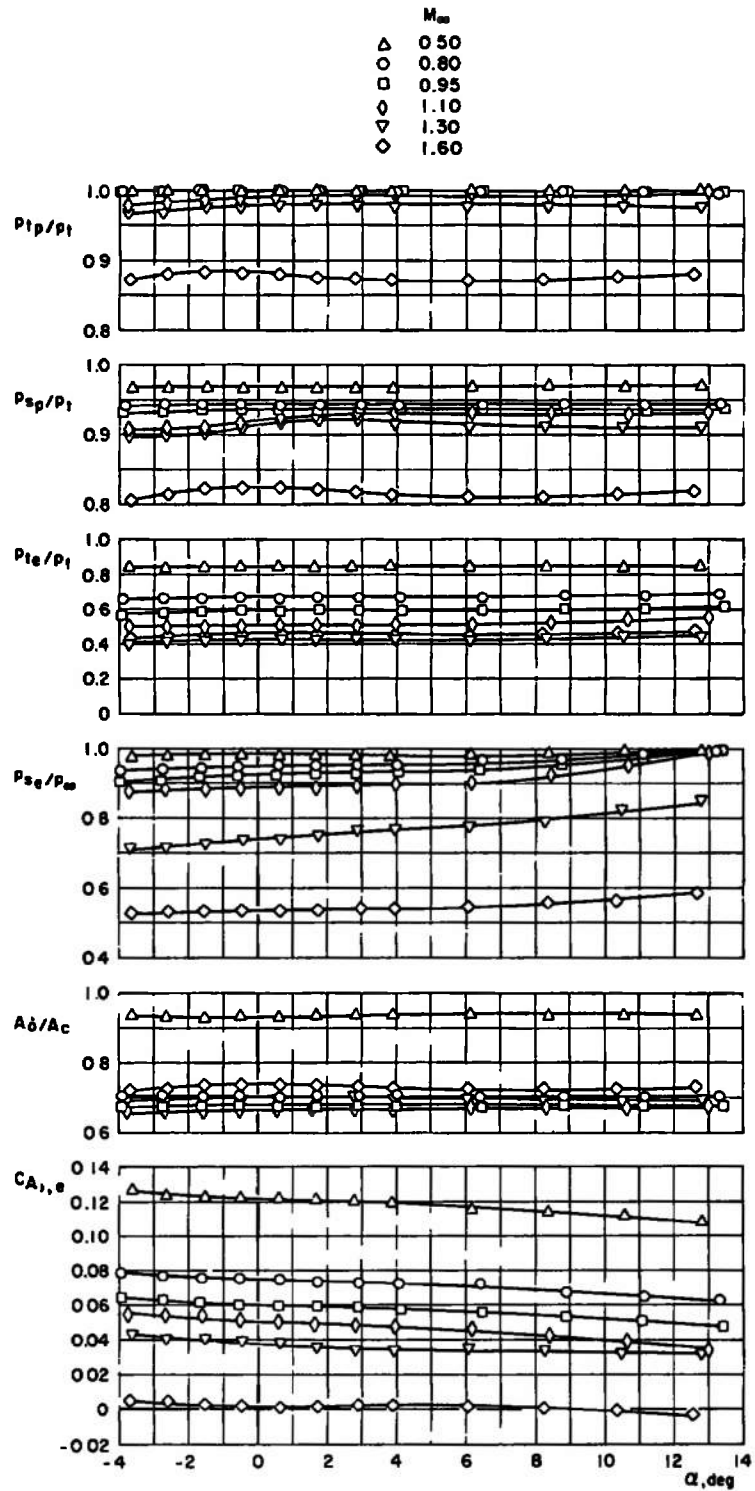


Figure 7. Effect of angle of attack on the inlet characteristics, $A_t = 0.505 \text{ in.}^2$, $\delta_c = \delta_s = \beta = 0$, configuration 2.

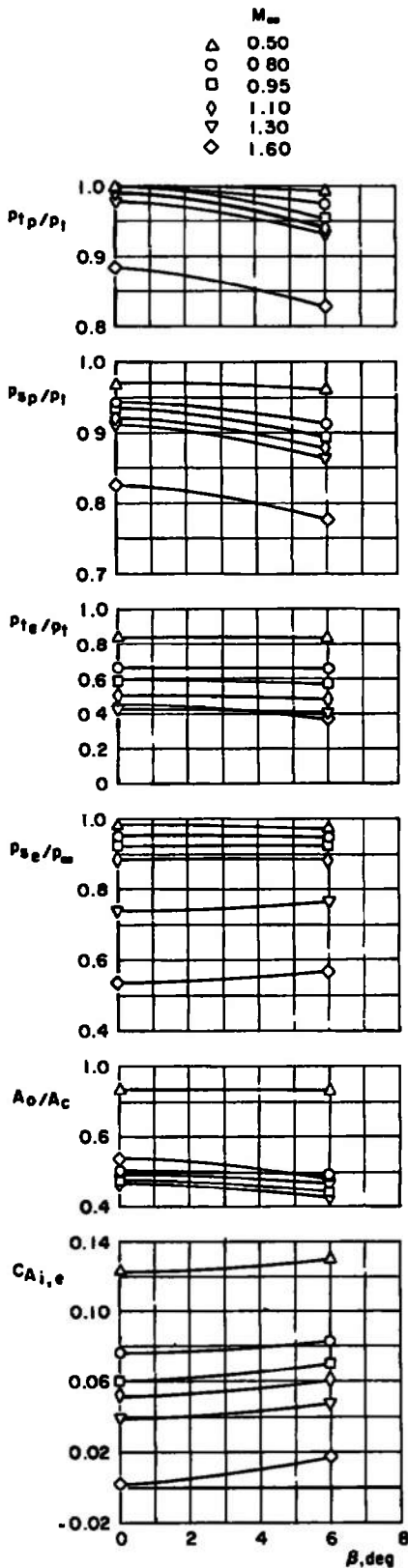


Figure 8. Effect of angle of sideslip on the inlet characteristics, $A_t = 0.505 \text{ in.}^2$, $\delta_c = \delta_a = \alpha = 0$, configuration 2.

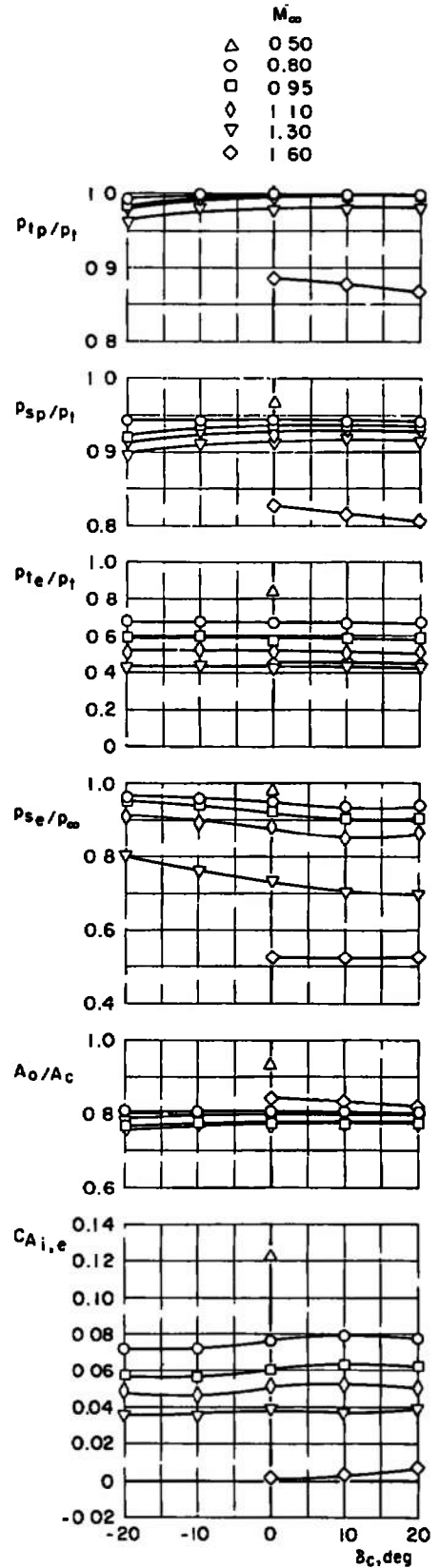


Figure 9. Effect of canard deflection on the inlet characteristics, $A_t = 0.505 \text{ in.}^2$, $\delta_a = \alpha = \beta = 0$.

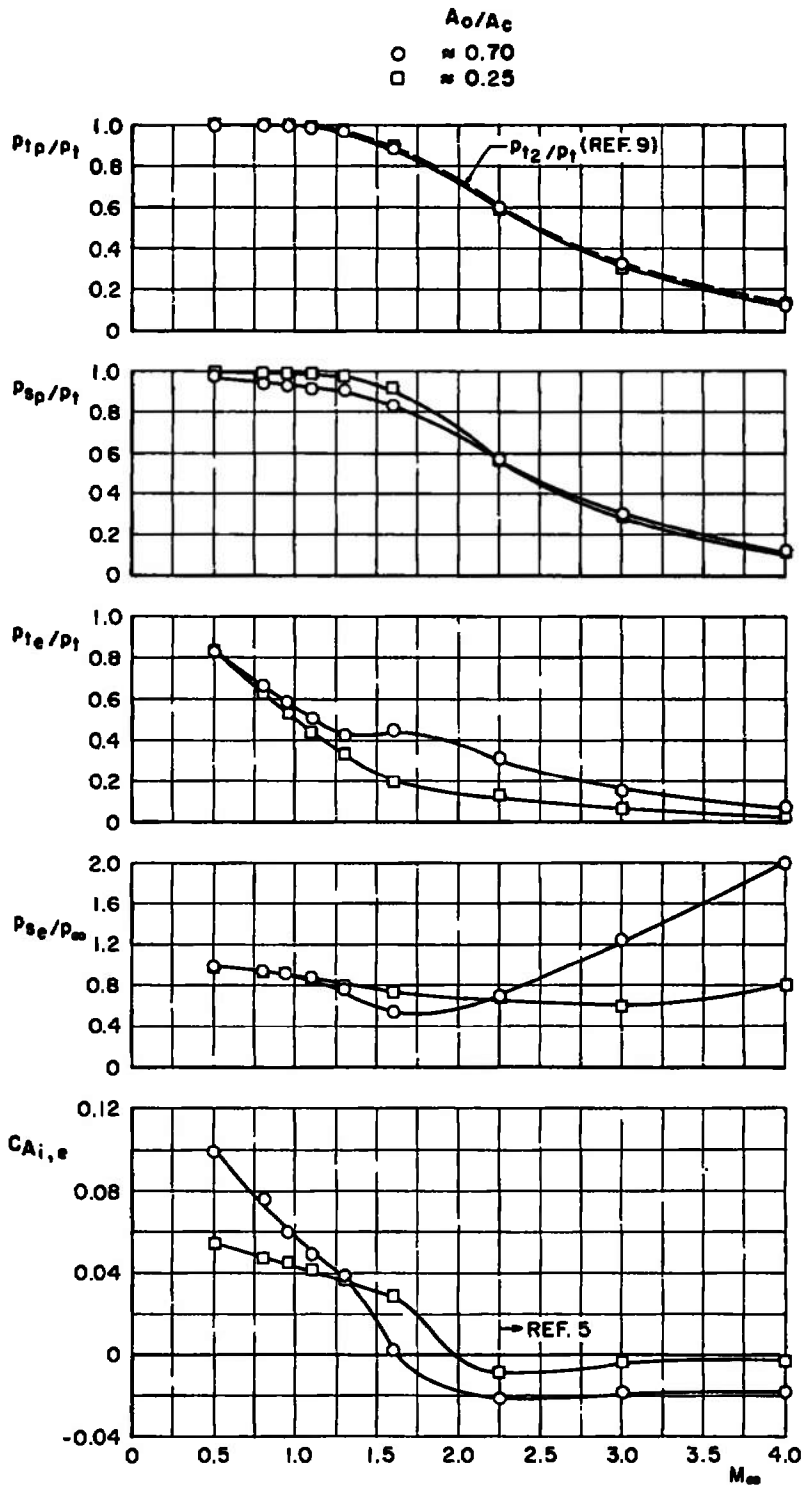


Figure 10. Variation of the inlet characteristics with Mach number, $\delta_c = \delta_a = \alpha = \beta = 0$, configuration 2.

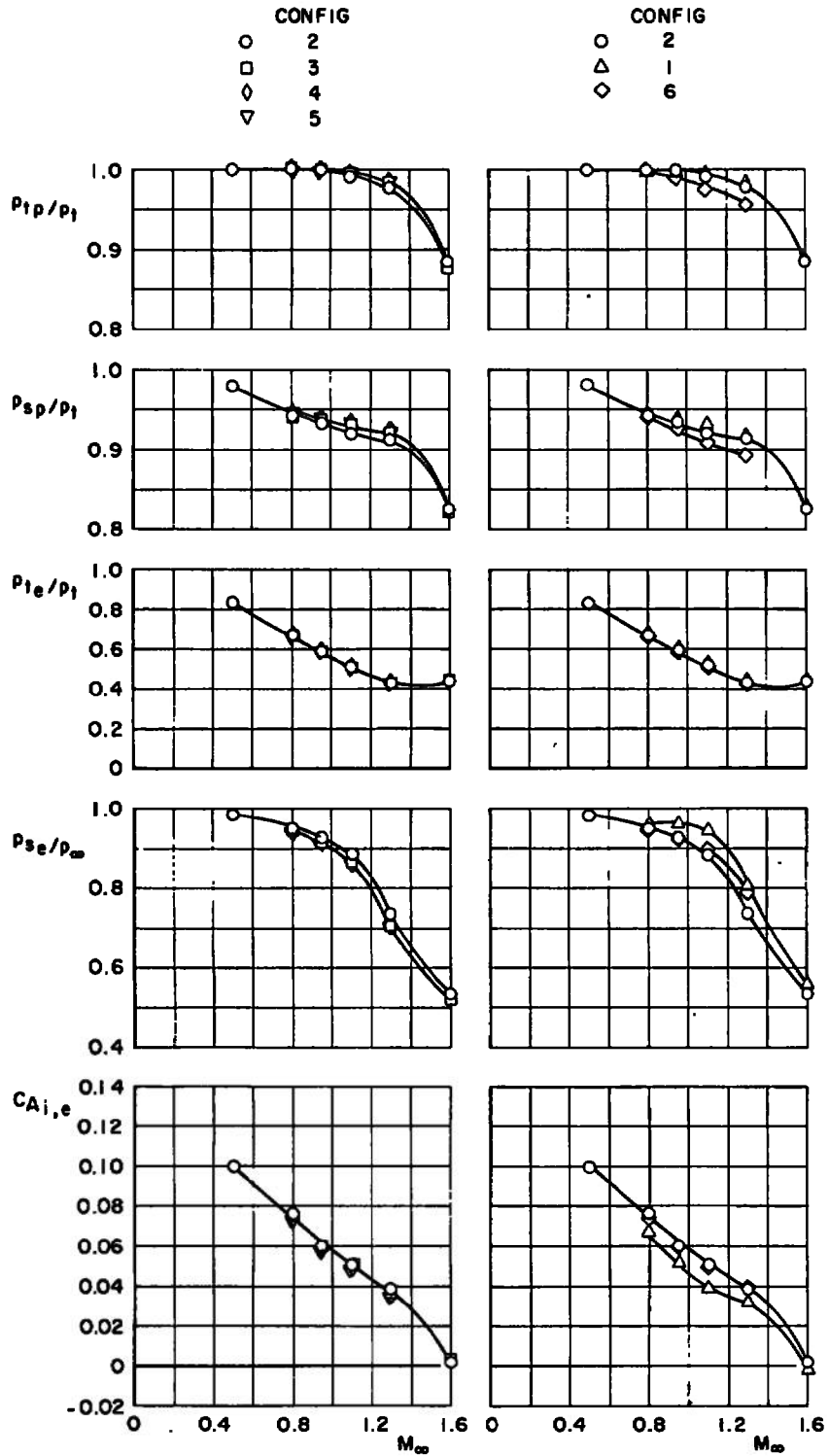
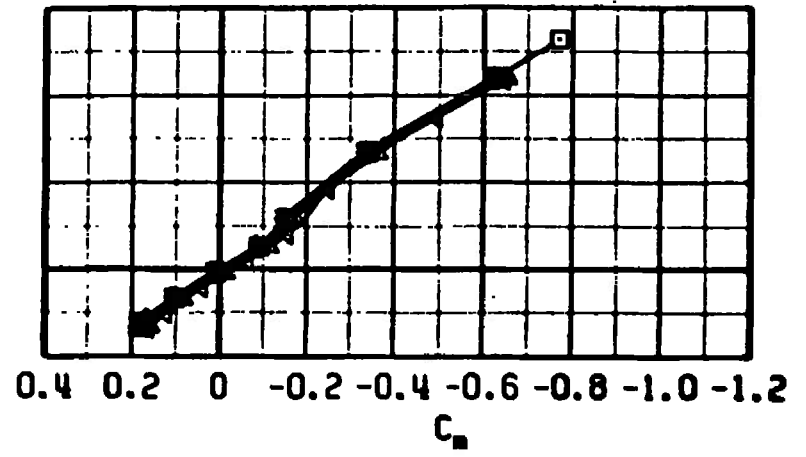
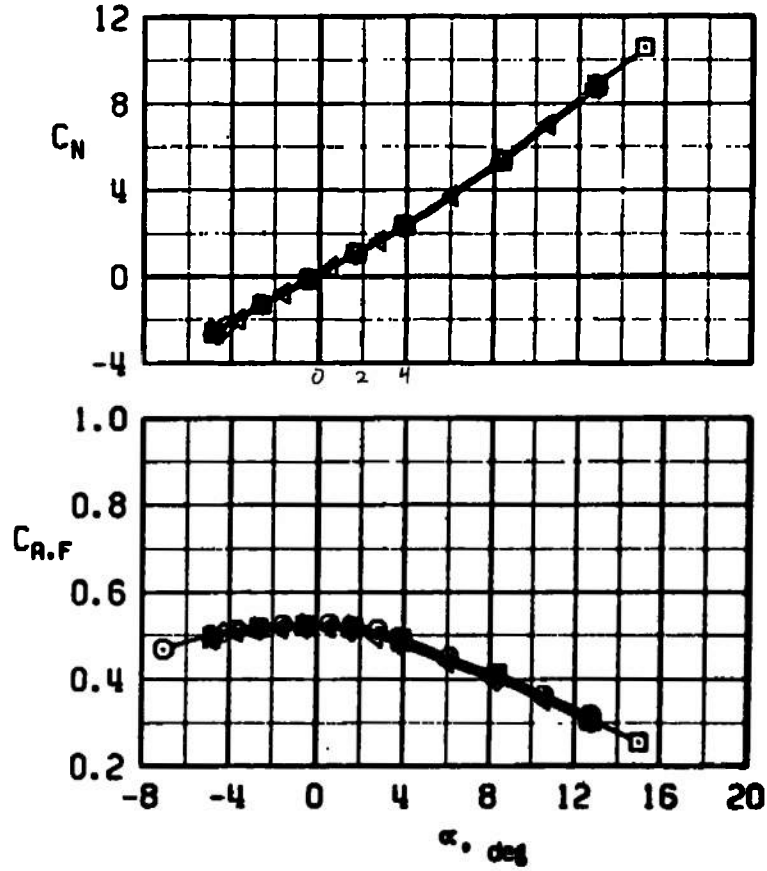


Figure 11. Variation of the inlet characteristics with model configuration, $\delta_c = \delta_n = \alpha = \beta = 0$, $A_o/A_c = 0.7$.

SYMBOL	M_{∞}	CONFIG	δ_c	δ_a	β	At	A_o/A_c
△	0.50	2	0	0	0	0	0
□						0.101	0.182
◀						0.202	0.367
◇						0.304	0.552
×						0.405	0.746
○						0.505	0.937
▽						0.607	1.157

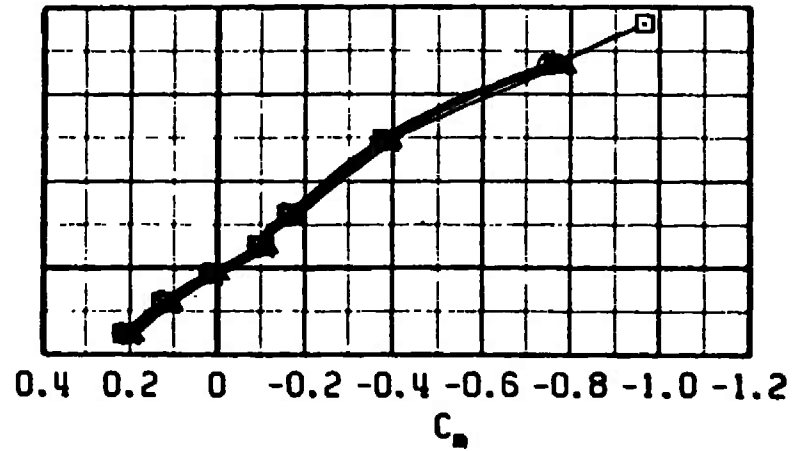
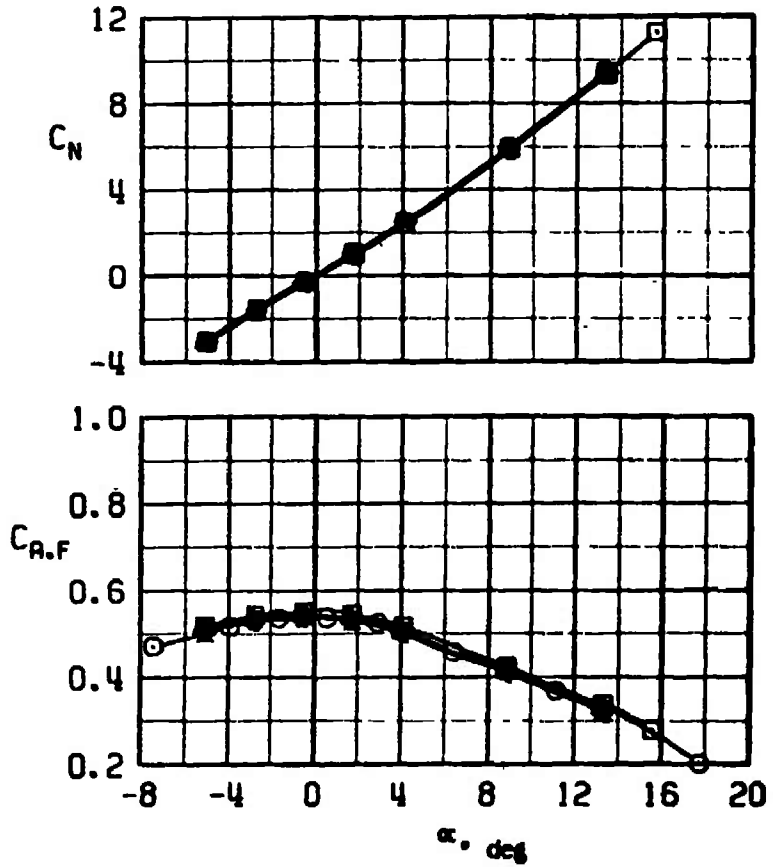
38



a. $M_{\infty} = 0.5$

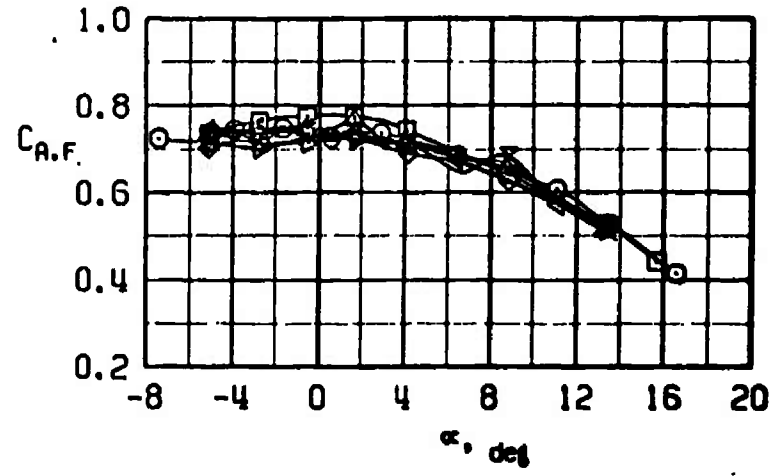
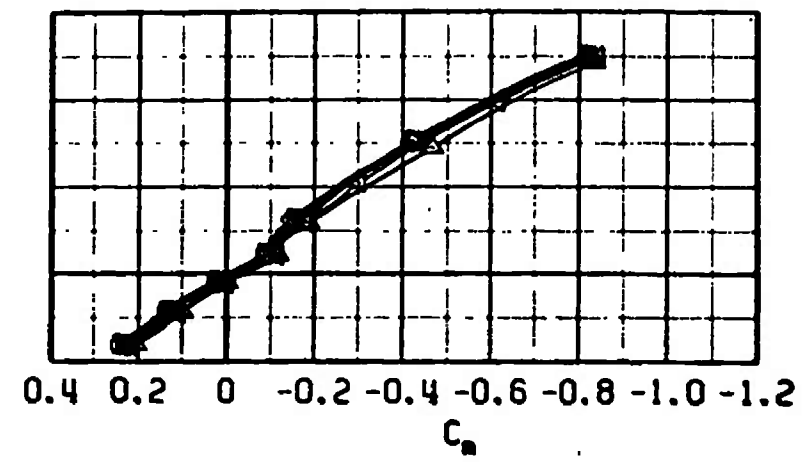
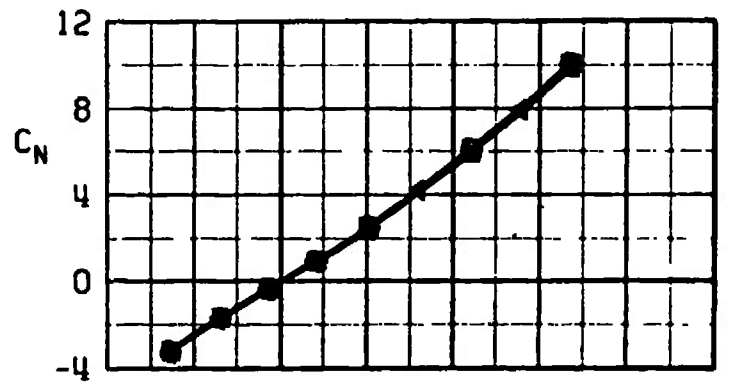
Figure 12. Effects of capture area ratio on the normal-force, pitching-moment, and axial-force coefficients, configuration 2, $\delta_c = \delta_a = \beta = 0$.

SYMBOL	M_{∞}	CONFIG	δ_c	δ_n	β	At	A_0/A_c
▲	0.80	2	0	0	0	0	0
◻						0.101	0.141
◄						0.202	0.283
◊						0.304	0.424
✕						0.405	0.568
○						0.505	0.705
▼						0.607	0.861



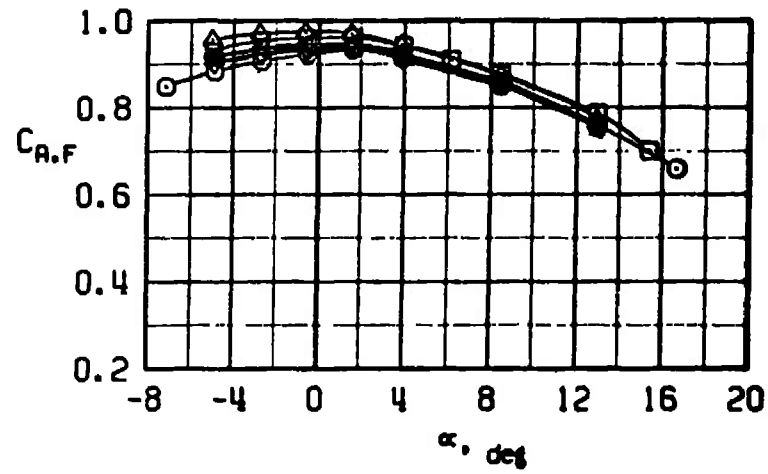
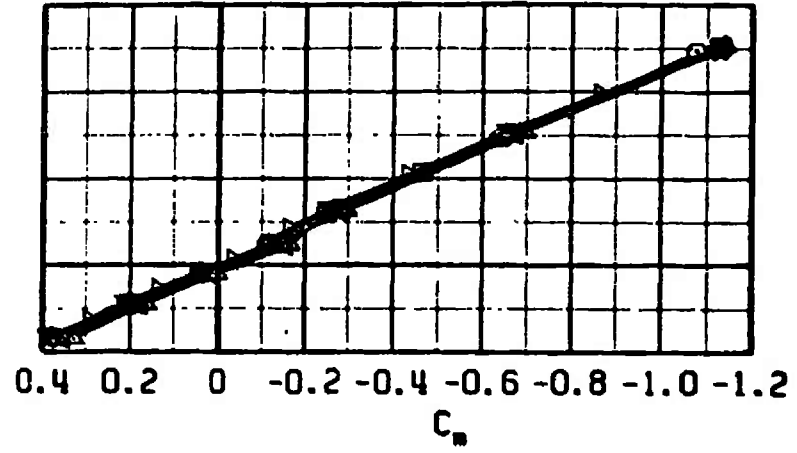
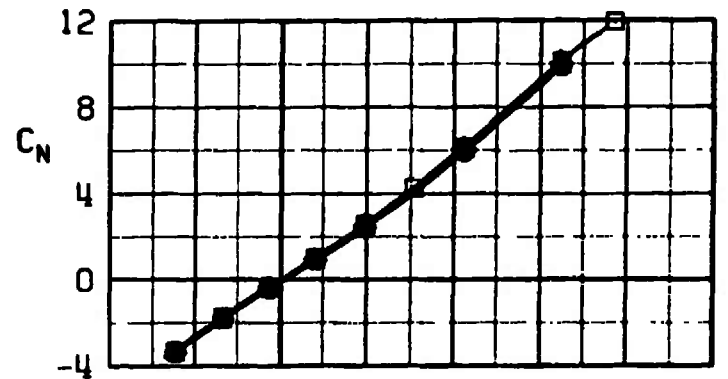
b. $M_{\infty} = 0.8$
Figure 12. Continued.

SYMBOL	M_∞	CONFIG	b_c	b_R	β	At	A_0/A_c
△	0.95	2	0	0	0	0	0
□						0.101	0.136
▽						0.202	0.272
◇						0.304	0.406
×						0.405	0.543
○						0.505	0.675
△						0.607	0.817



c. $M_\infty = 0.95$
Figure 12. Continued.

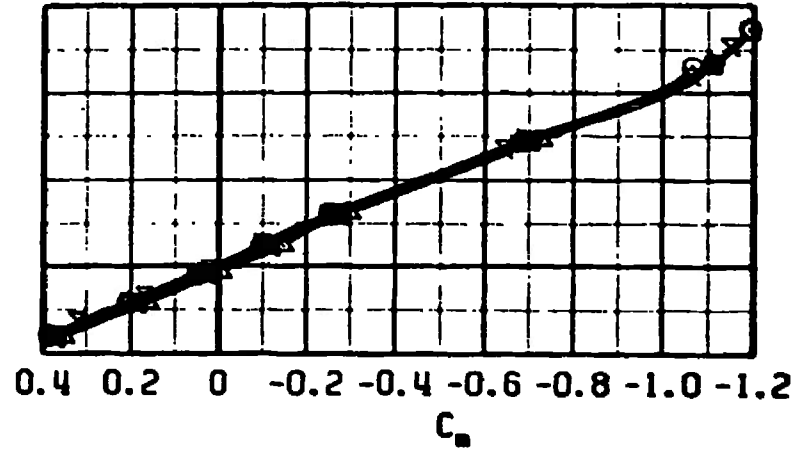
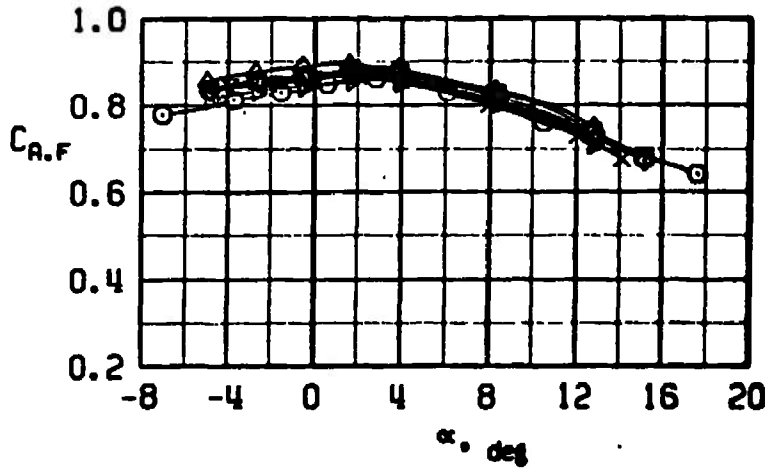
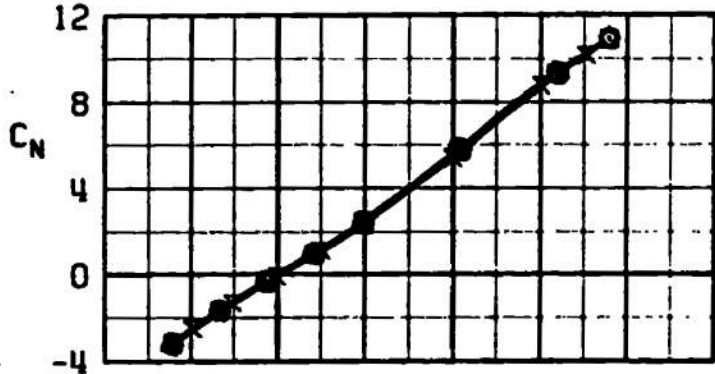
SYMBOL	M_∞	CONFIG	δ_c	δ_n	β	Rt	A_0/A_c
\triangle	1.10	2	0	0	0	0	0
\square						0.101	0.136
\triangle						0.202	0.273
\diamond						0.304	0.405
\times						0.405	0.544
\circ						0.505	0.667
∇						0.607	0.818



d. $M_\infty = 1.1$
Figure 12. Continued.

SYMBOL	M_{∞}	CONFIG	t_c	t_n	β	At	A_0/A_c
△	1.30	2	0	0	0	0	0
□						0.101	0.142
▽						0.202	0.287
◇						0.304	0.428
X						0.405	0.558
○						0.505	0.699
▽						0.607	0.850

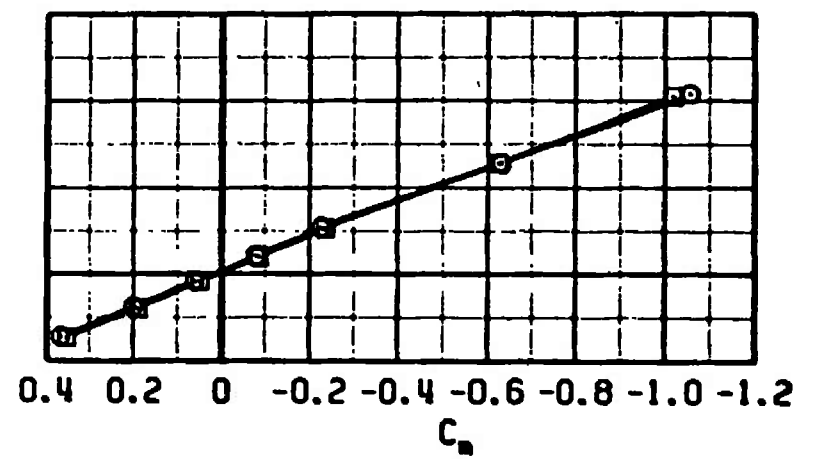
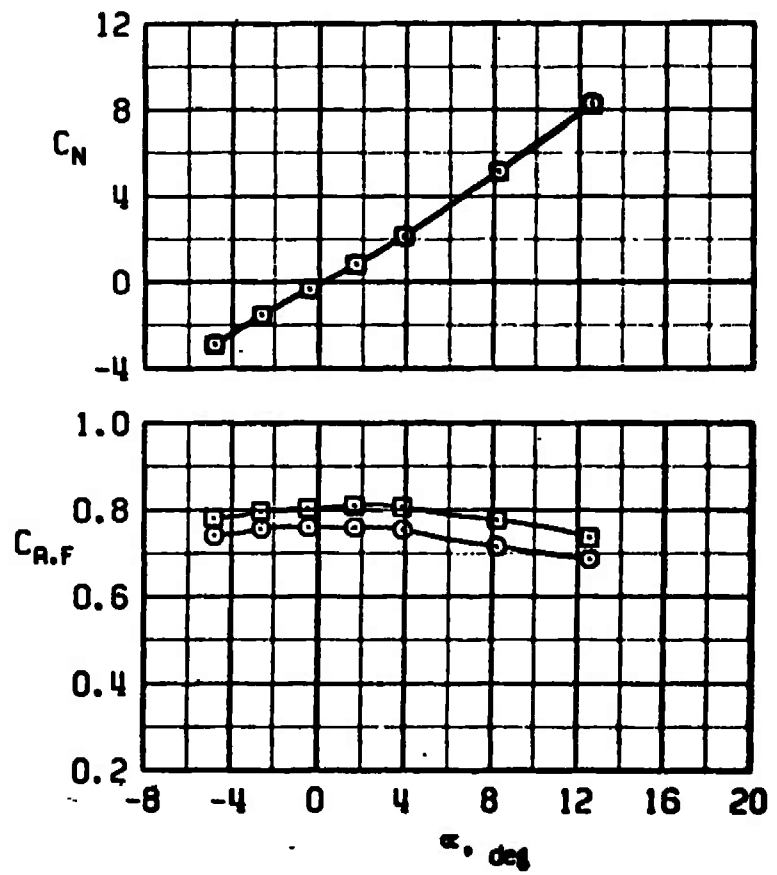
42



e. $M_{\infty} = 1.3$
Figure 12. Continued.

SYMBOL	M_{∞}	CONFIG	b_c	b_n	β	At	A_0/A_c
□	1.60	2	0	0	0	0.101	0.135
○	↓	↓	↓	↓	↓	0.505	0.739

43



f. $M_{\infty} = 1.6$
Figure 12. Concluded.

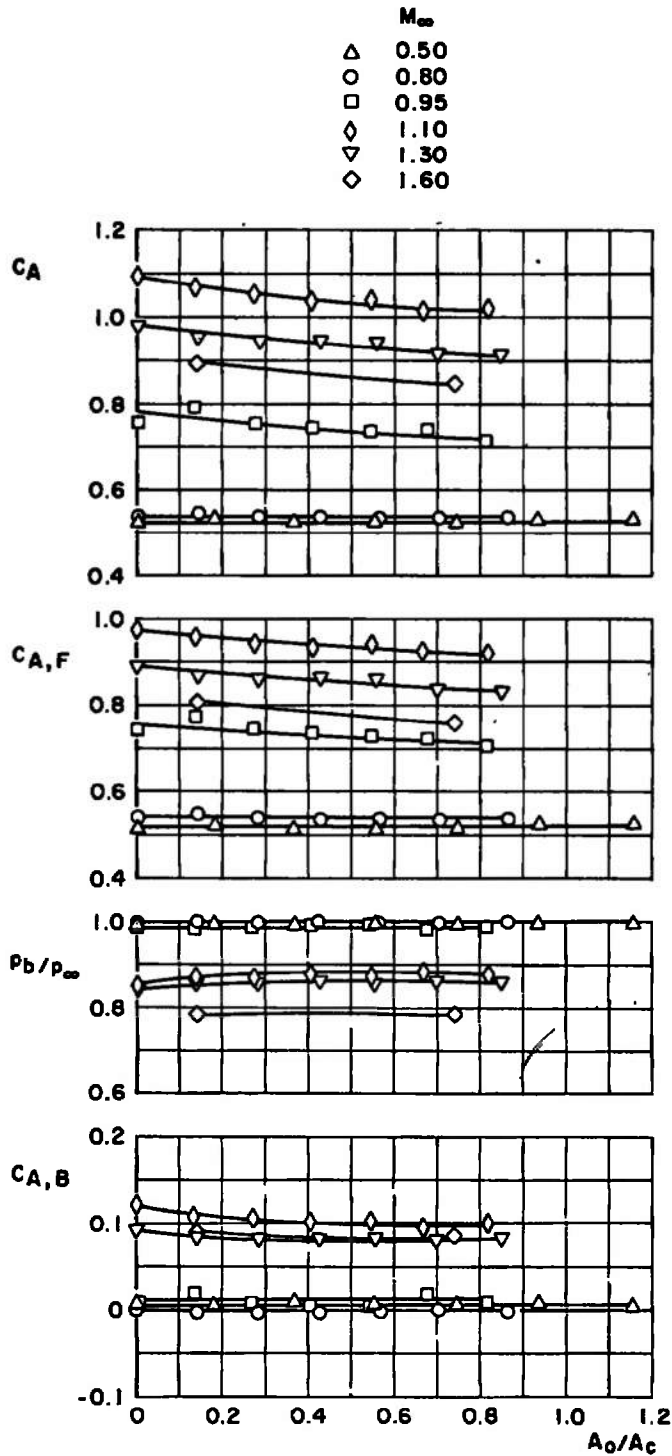
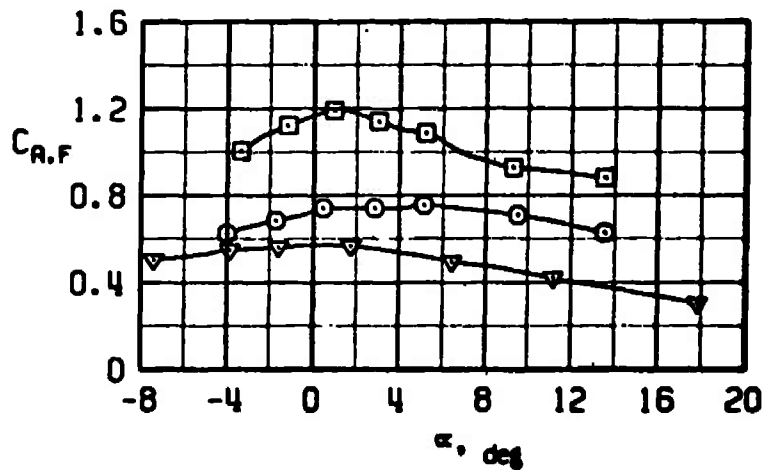
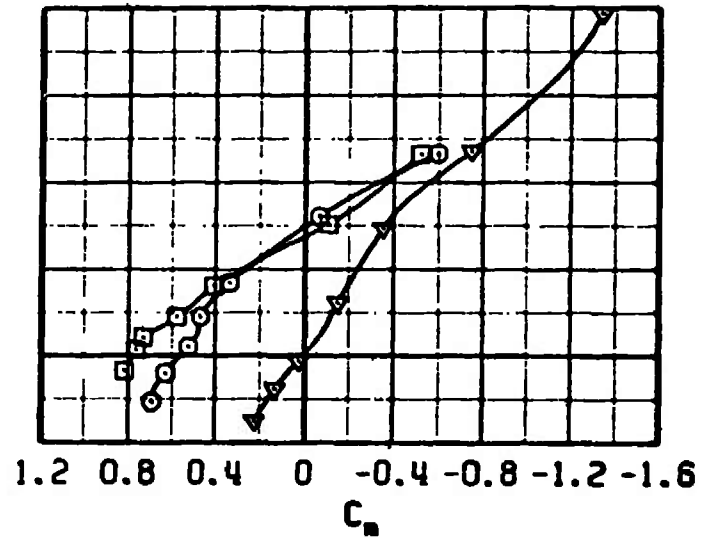
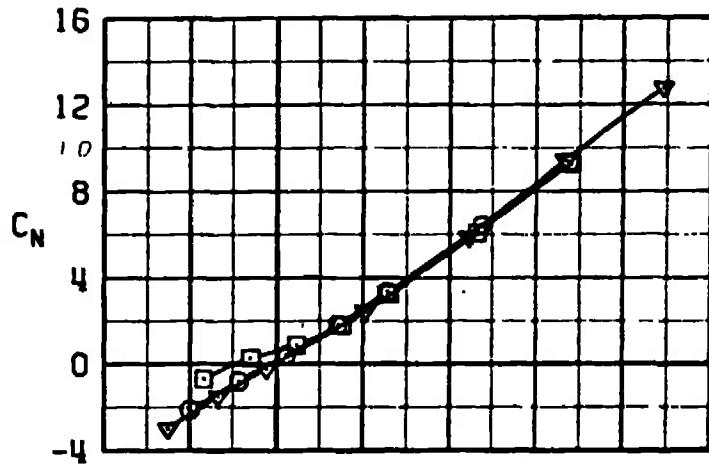


Figure 13. Variation of the axial-force and base pressure characteristics with capture area ratio at zero angle of attack, configuration 2, $\delta_c = \delta_a = \beta = 0$.

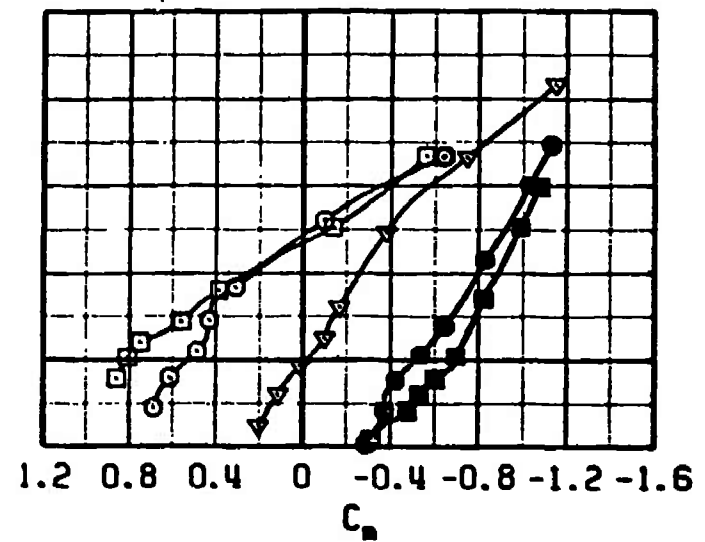
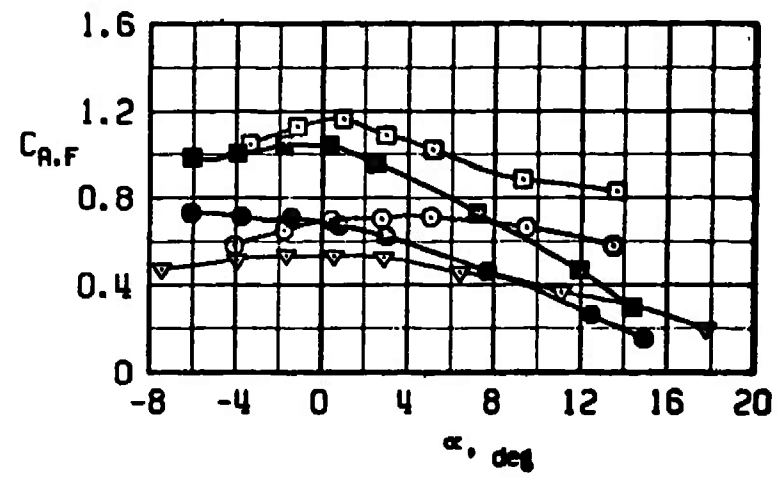
SYMBOL	M_{cc}	CONFIG	δ_c	δ_n	β
▽	0.80	1	0	0	0
○	↓	↓	10	↓	↓
□	↓	↓	20	↓	↓



a. Configuration 1

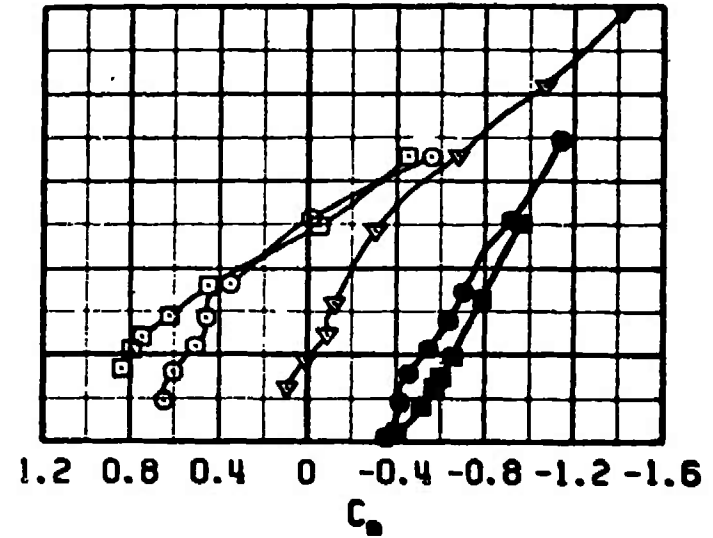
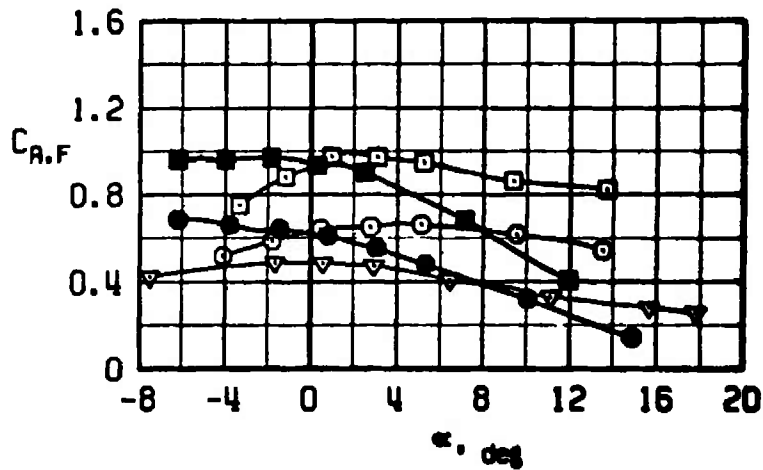
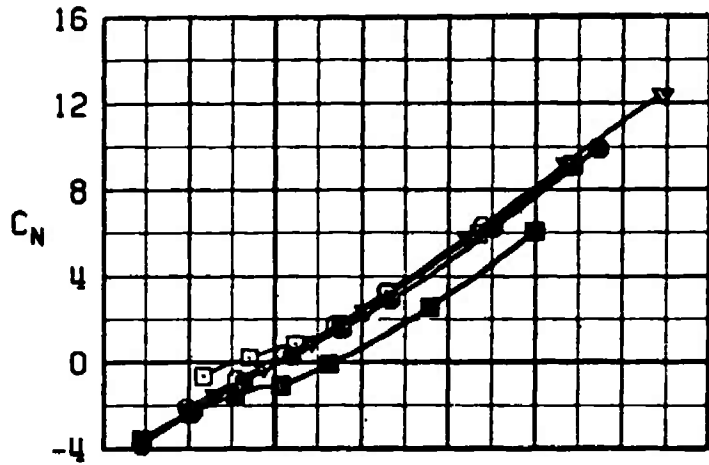
Figure 14. Effects of canard deflection on the normal-force, pitching-moment and axial-force coefficients, $M_{\infty} = 0.8$, $A_t = 0.505 \text{ in.}^2$, $\delta_n = \beta = 0$.

SYMBOL	Mach	CONFIG	ξ_c	ξ_e	β
■	0.80	2	-20	0	0
●			-10		
▼			0		
○			10		
□			20		



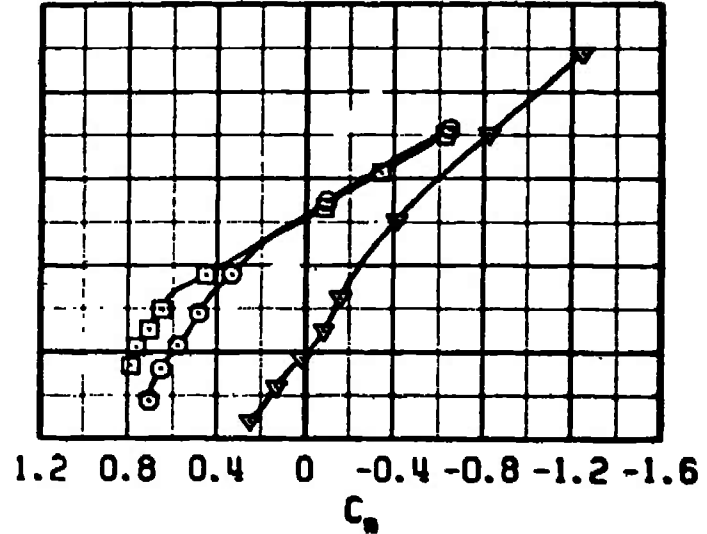
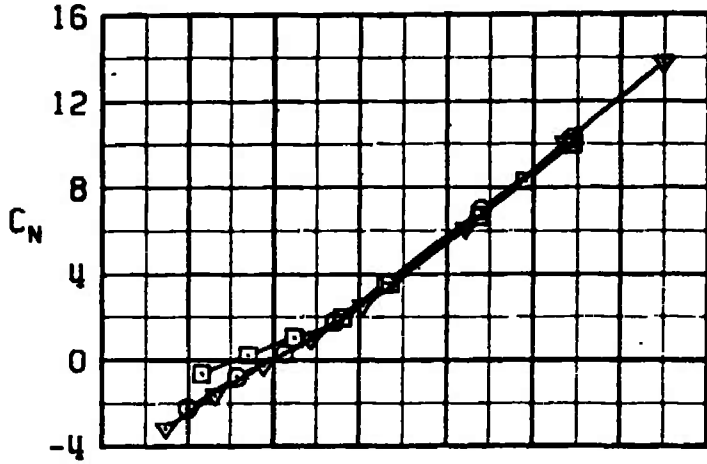
b. Configuration 2
Figure 14. Continued.

SYMBOL	M_∞	CONFIG	ϵ_c	ϵ_w	β
■	0.80	3	-20	0	0
●			-10		
▼			0		
○			10		
□			20		



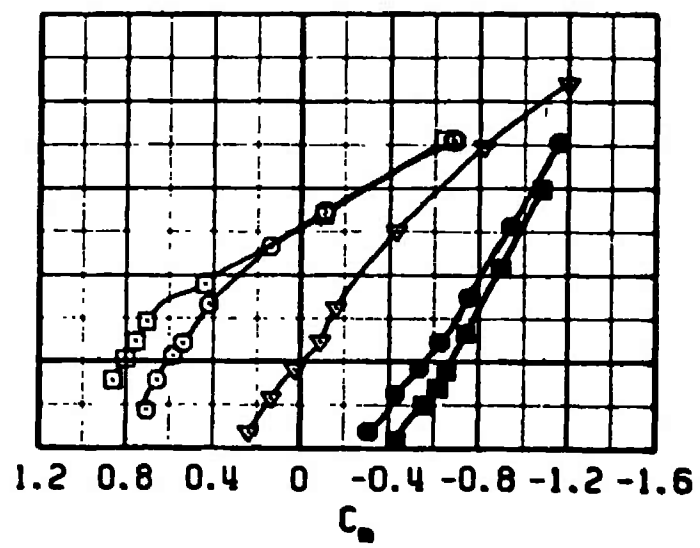
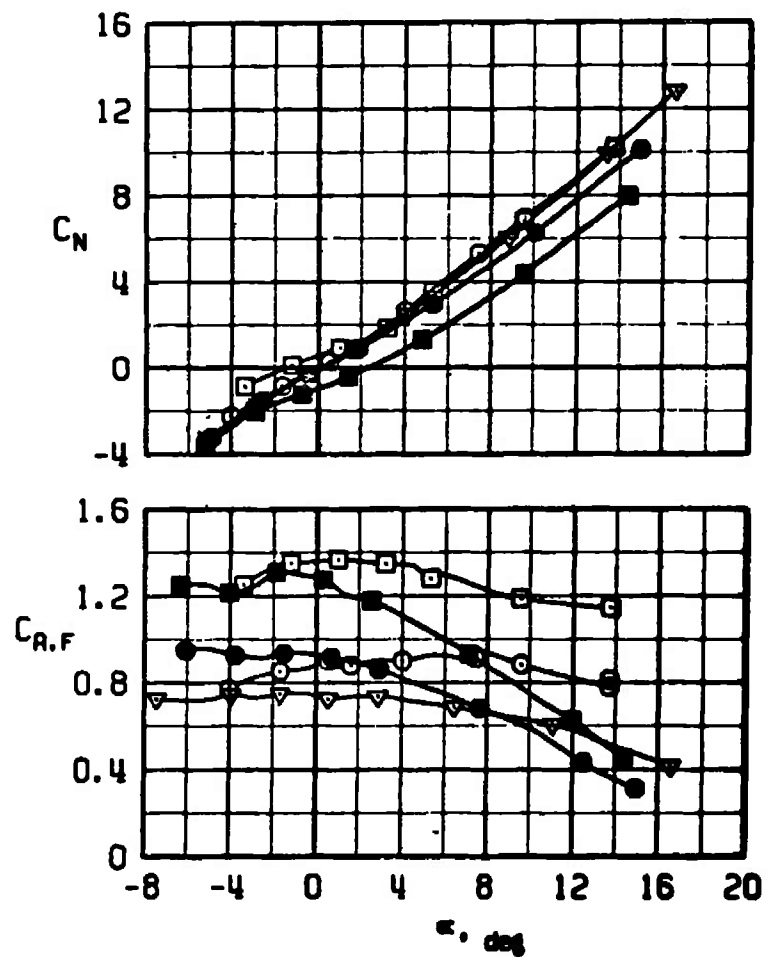
c. Configuration 3
Figure 14. Concluded.

SYMBOL	M_∞	CONFIG	δ_c	δ_a	β
▼	0.95	1	0	0	0
○	↓	↓	10	↓	↓
□	↓	↓	20	↓	↓



a. Configuration 1
 Figure 15. Effects of canard deflection on the normal-force, pitching-moment, and axial-force coefficients, $M_\infty = 0.95$, $A_t = 0.505 \text{ in.}^2$, $\delta_a = \beta = 0$.

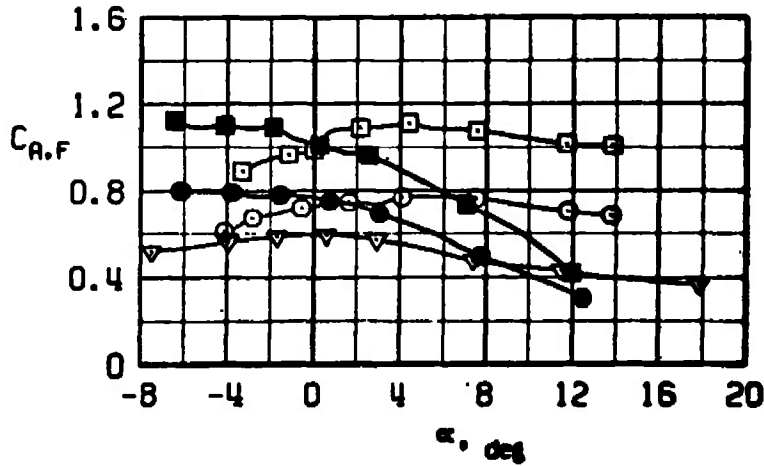
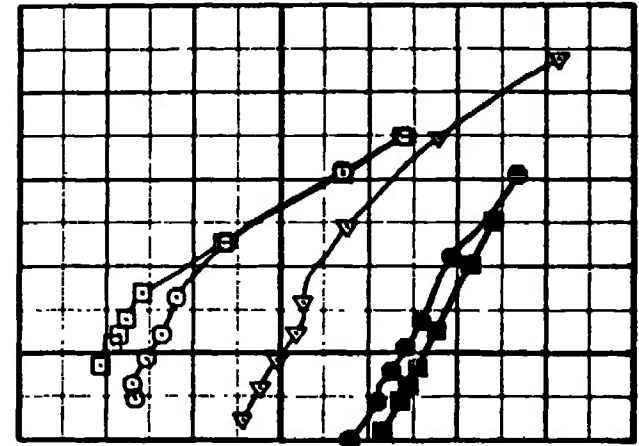
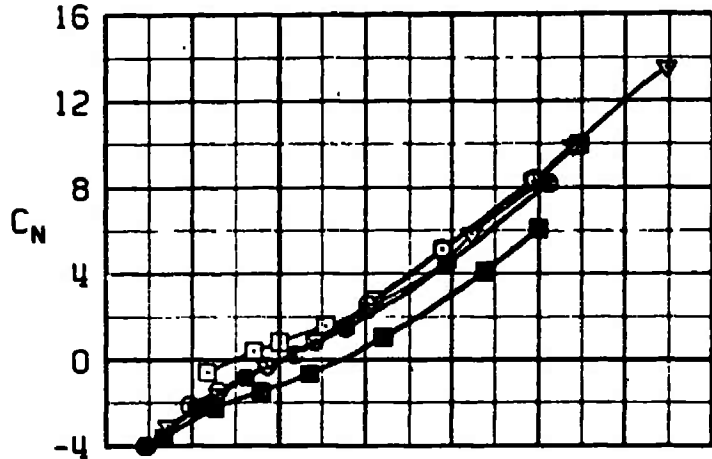
SYMBOL	M _∞	CONFIG	ϵ_c	ϵ_n	β
■	0.95	2	-20	0	0
●			-10		
▼			0		
○			10		
□			20		



b. Configuration 2
Figure 15. Continued.

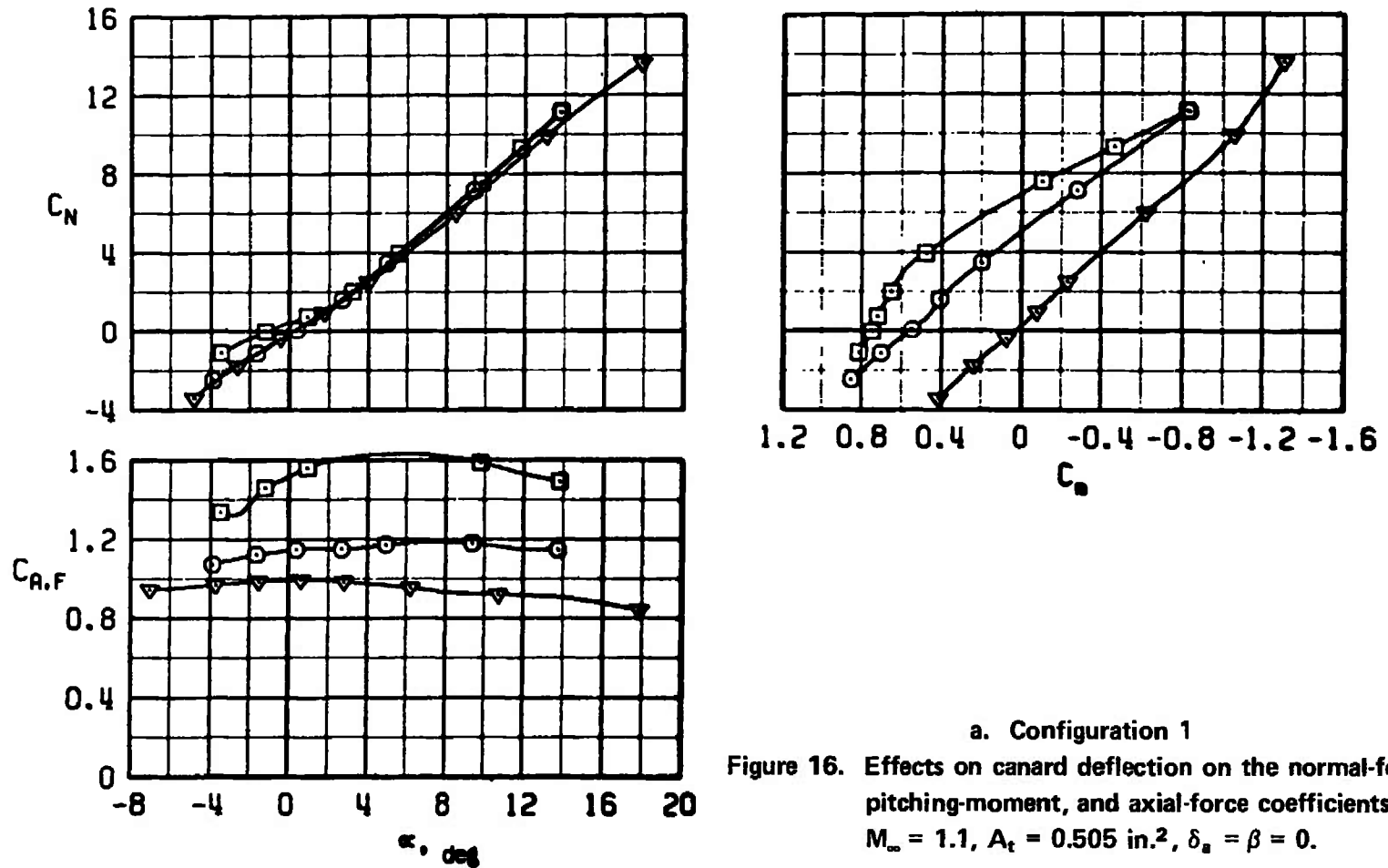
SYMBOL	M _∞	CONFIG	δ _c	δ _a	β
■	0.95	3	-20	0	0
●			-10		
▼			0		
○			10		
□			20		

50

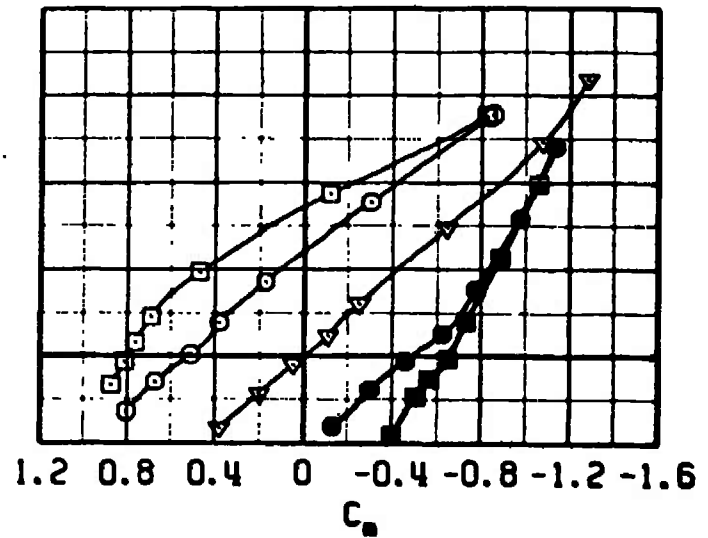
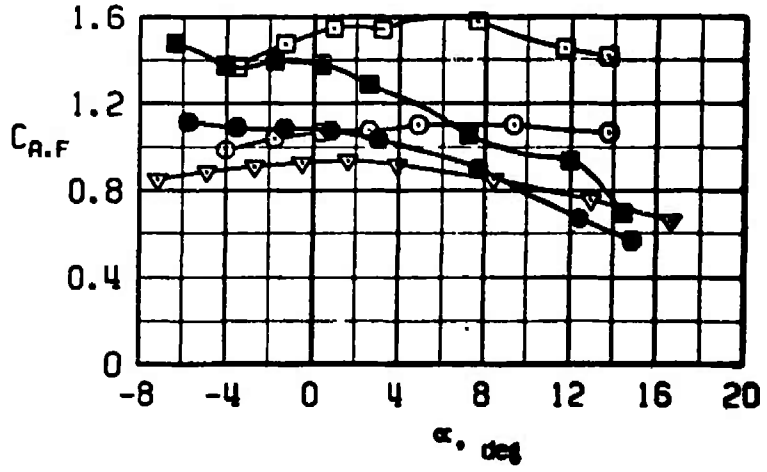


c. Configuration 3
Figure 15. Concluded.

SYMBOL	M_{∞}	CONFIG	δ_c	δ_n	β
▽	1.10	1	0	0	0
○	↓	↓	10	↓	↓
□	↓	↓	20	↓	↓

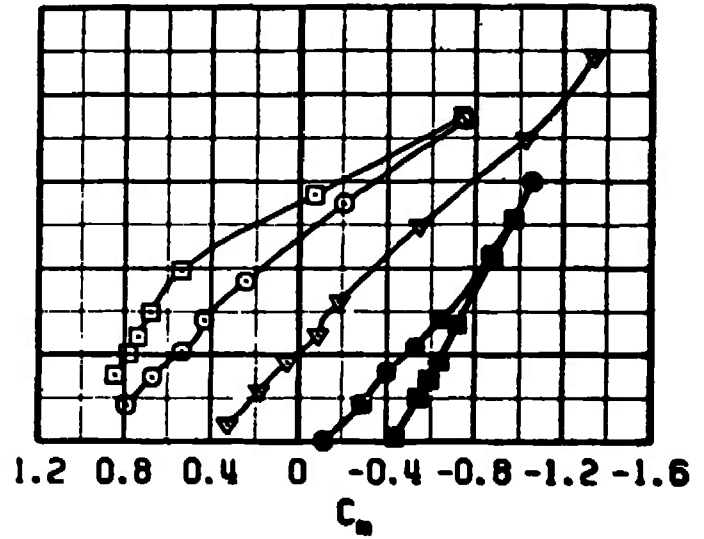
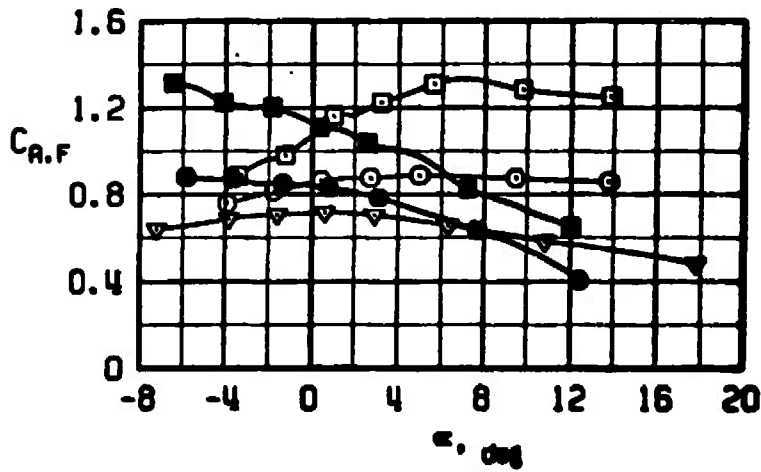


SYMBOL	M_{∞}	CONFIG	δ_c	δ_R	β
■	1.10	2	-20	0	0
●			-10		
▼			0		
○			10		
□			20		



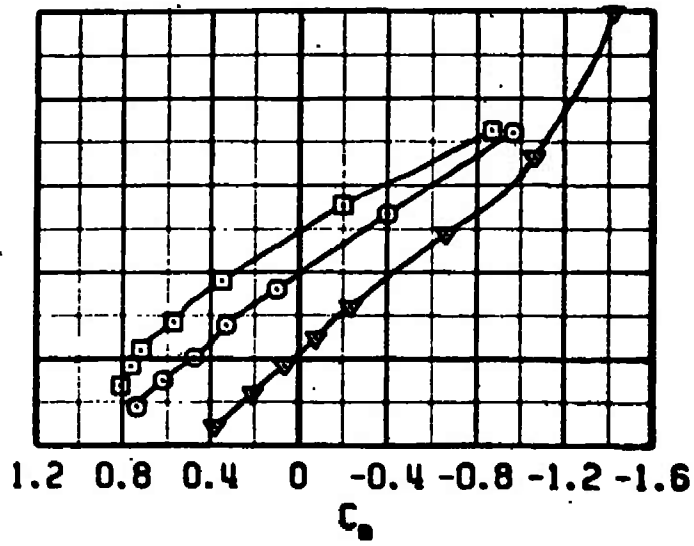
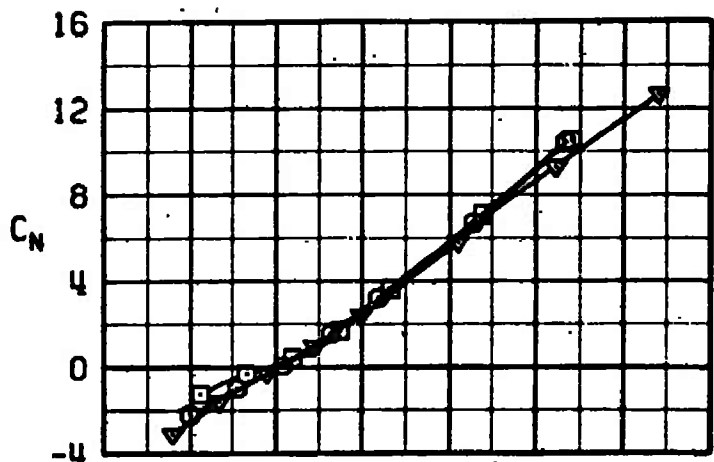
b. Configuration 2
Figure 16. Continued.

SYMBOL	M_{∞}	CONFIG	α_r	α_n	β
■	1.10	3	-20	0	0
●			-10		
▼			0		
○			10		
□			20		



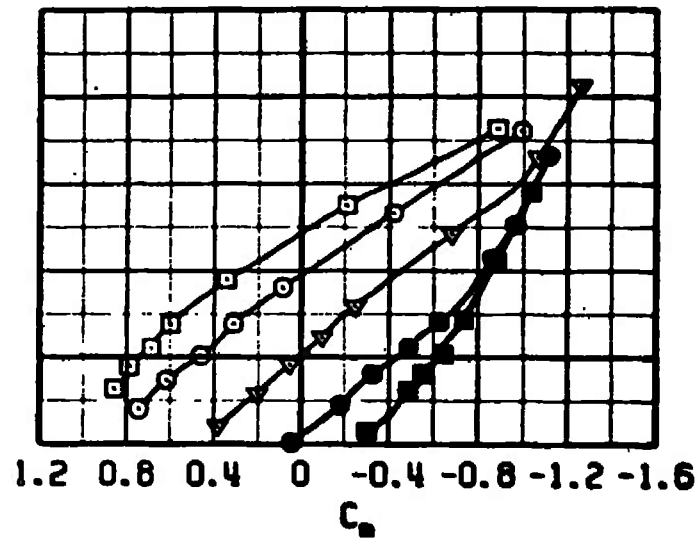
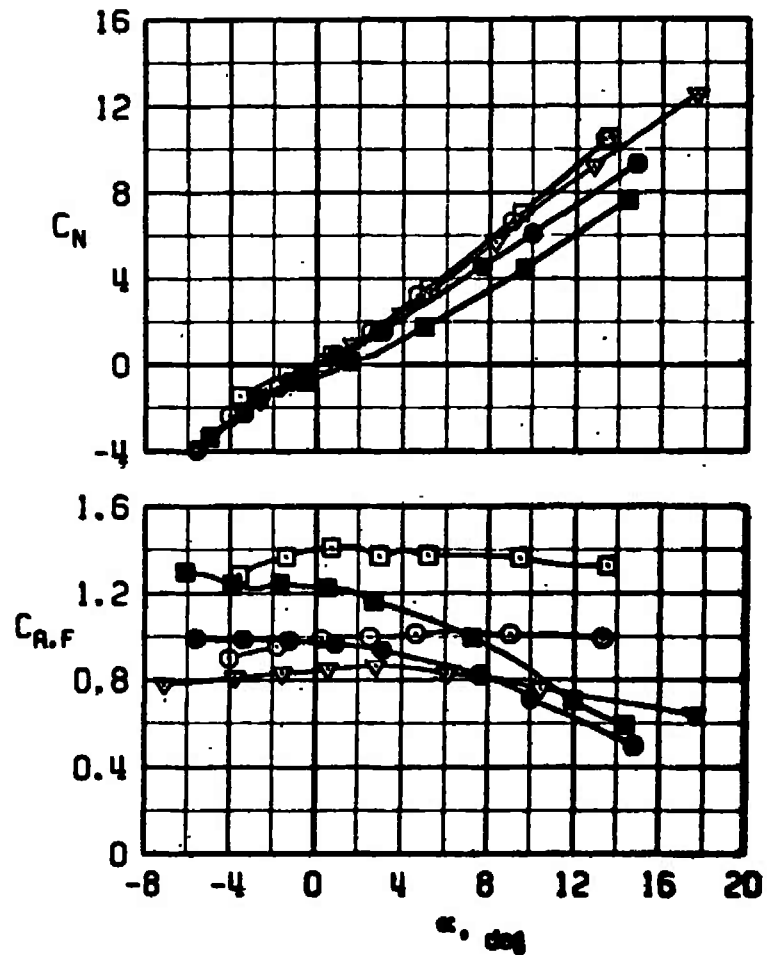
c. Configuration 3
Figure 16. Concluded.

SYMBOL	M_{∞}	CONFIG	δ_c	δ_a	β
▼	1.30	1	0	0	0
○	↓	↓	10	↓	↓
□	↓	↓	20	↓	↓



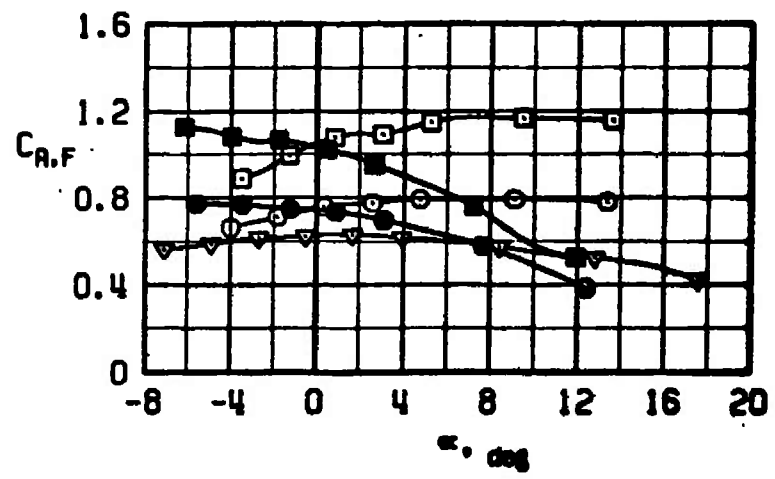
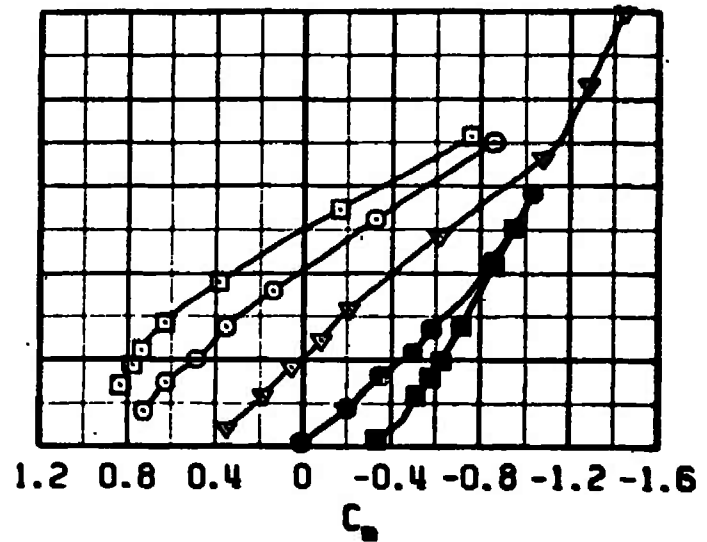
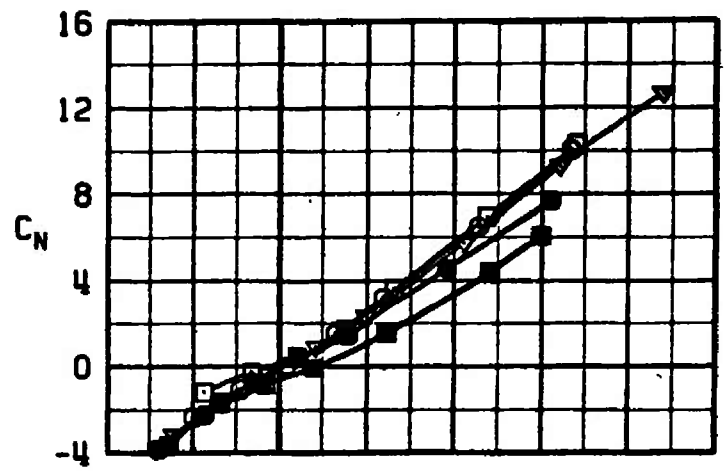
a. Configuration 1
 Figure 17. Effects of canard deflection on the normal-force, pitching-moment, and axial-force coefficients, $M_{\infty} = 1.3$, $A_t = 0.505 \text{ in.}^2$, $\delta_a = \beta = 0$.

SYMBOL	M_{∞}	CONFIG	ϵ_c	ϵ_n	β
■	1.30	2	-20	0	0
●			-10		
▼			0		
○			10		
□			20		



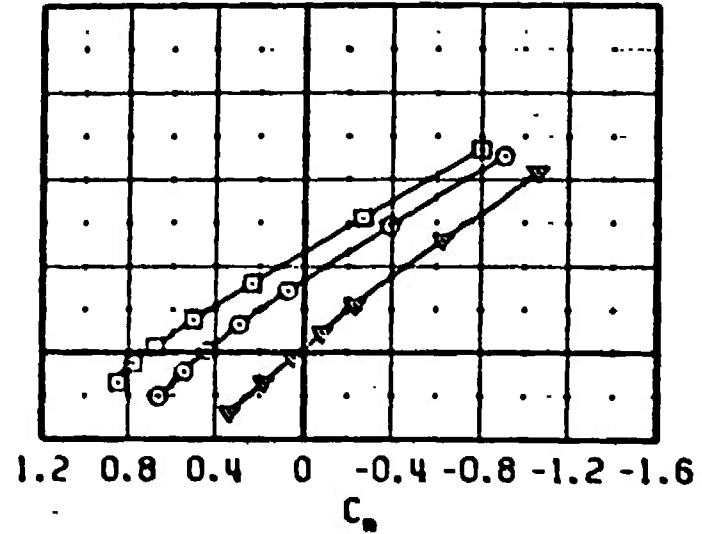
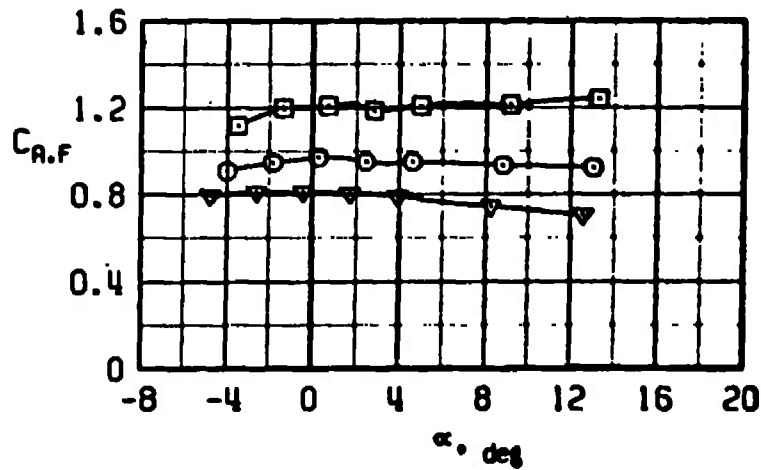
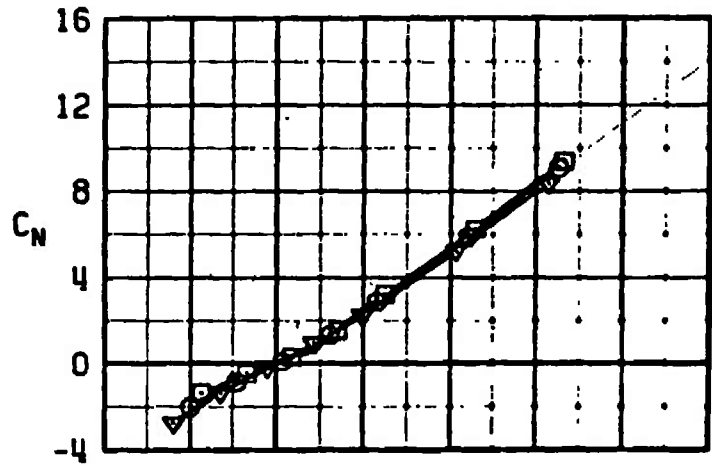
b. Configuration 2
Figure 17. Continued.

SYMBOL	M_∞	CONFIG	δ_c	δ_e	δ
■	1.30	3	-20	0	0
●			-10		
▼			0		
○			10		
□			20		



c. Configuration 3
Figure 17. Concluded.

SYMBOL	M_∞	CONFIG	δ_c	δ_n	β
▽	1.60	1	0	0	0
○			10		
□			20		

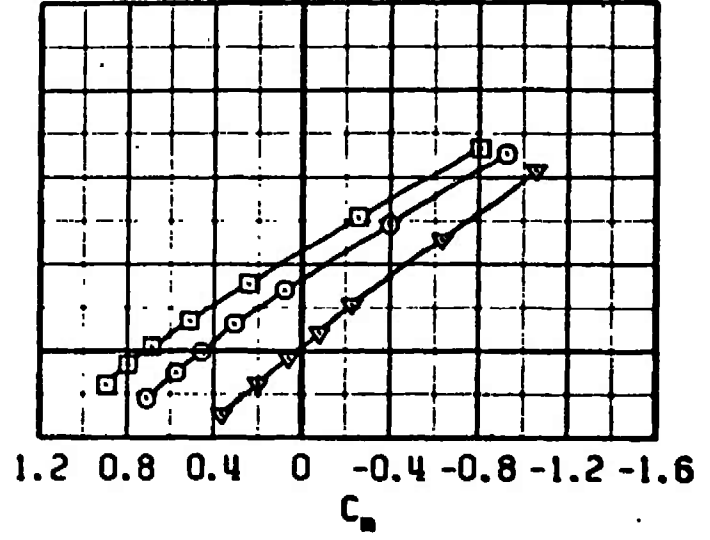
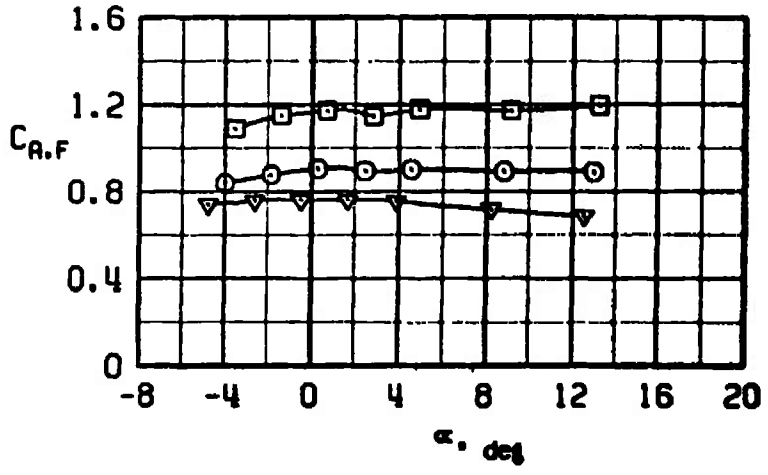
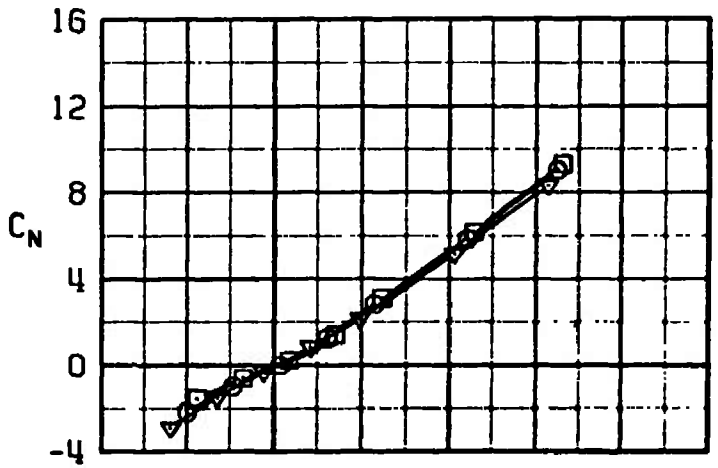


a. Configuration 1

Figure 18. Effects of canard deflection on the normal-force, pitching-moment, and axial-force coefficients, $M_\infty = 1.6$, $A_t = 0.505 \text{ in.}^2$, $\delta_n = \beta = 0$.

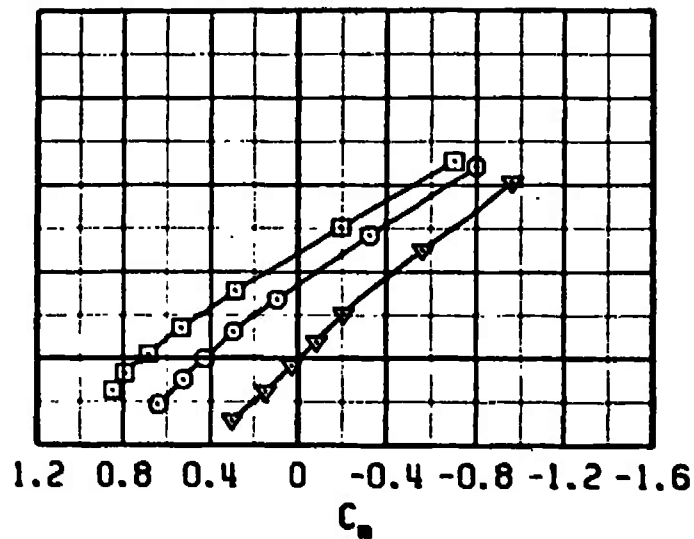
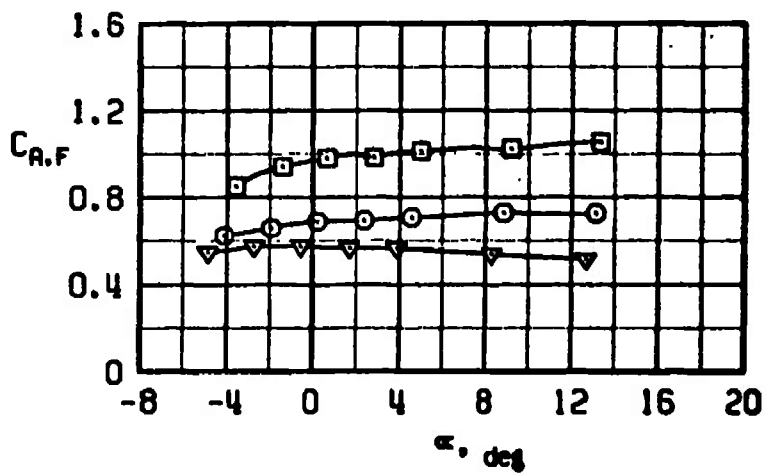
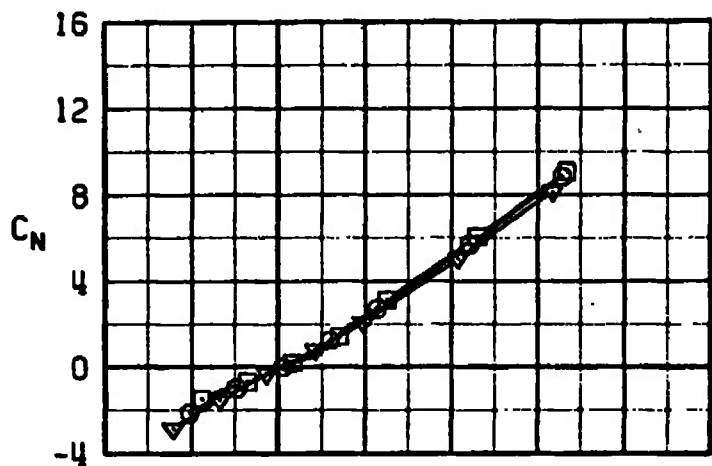
SYMBOL	M_{∞}	CONFIG	δ_c	δ_n	β
▽	1.60	2	0	0	0
○	↓	↓	10	↓	↓
□	↓	↓	20	↓	

58



b. Configuration 2
Figure 18. Continued.

SYMBOL	M_∞	CONFIG	δ_c	δ_n	β
▽	1.60	3	0	0	0
○	↓	↓	10	↓	↓
□	↓	↓	20	↓	↓



c. Configuration 3
Figure 18. Concluded.

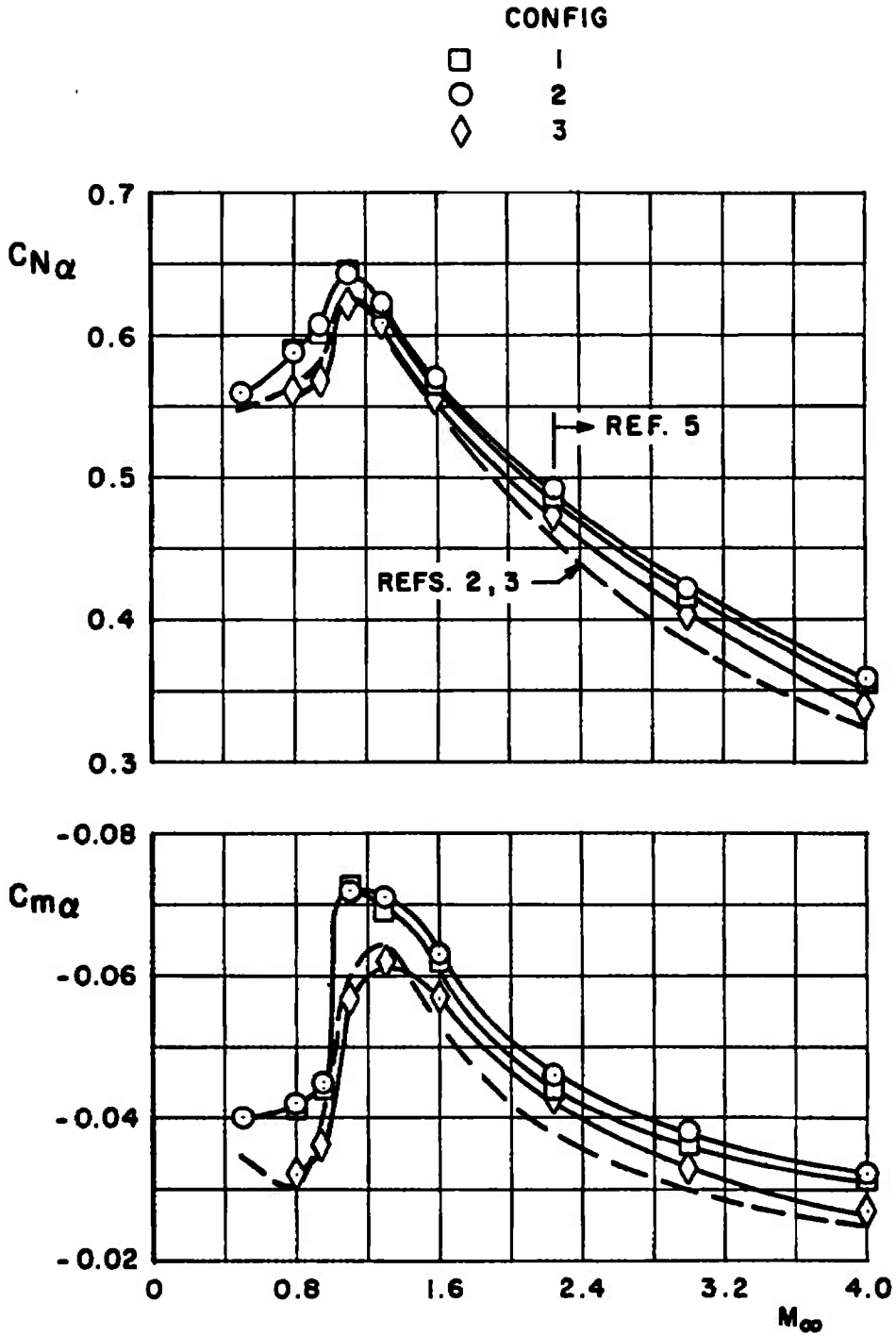


Figure 19. Effects of afterbody and antennas on $C_{N\alpha}$ and $C_{m\alpha}$,
 $A_t = 0.505 \text{ in.}^2$, $\delta_c = \delta_a = \alpha = \beta = 0$.

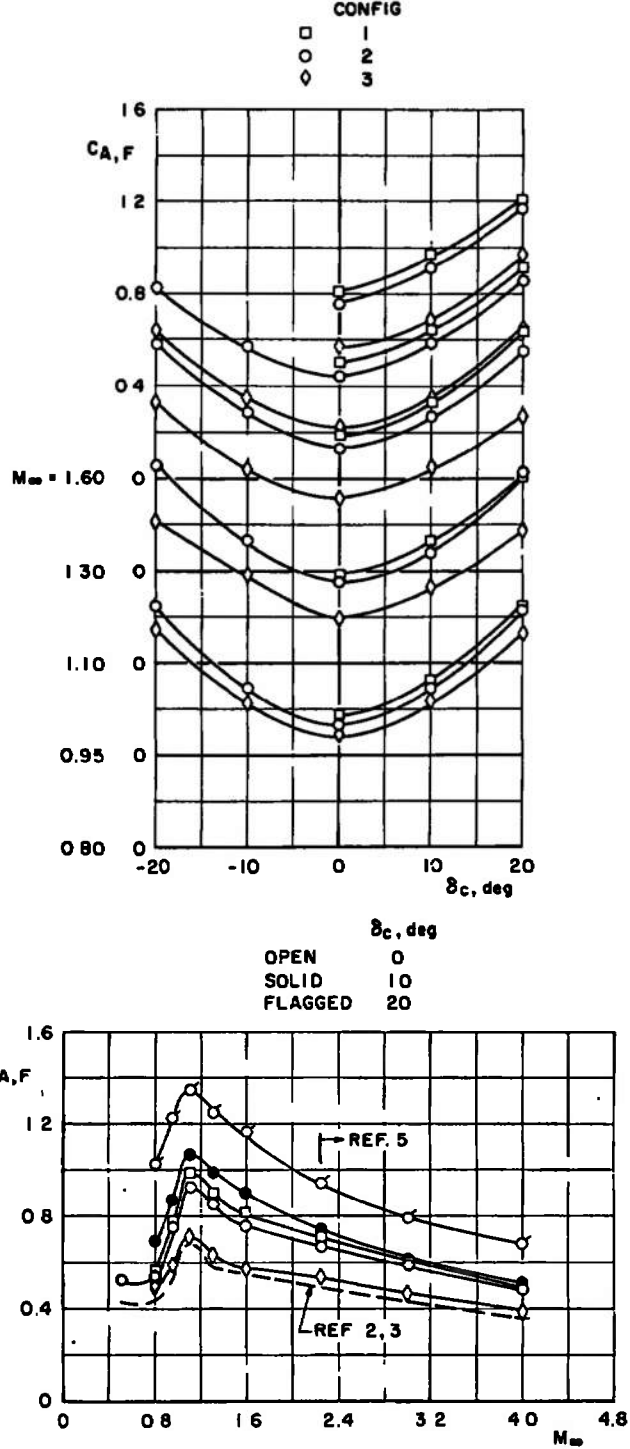
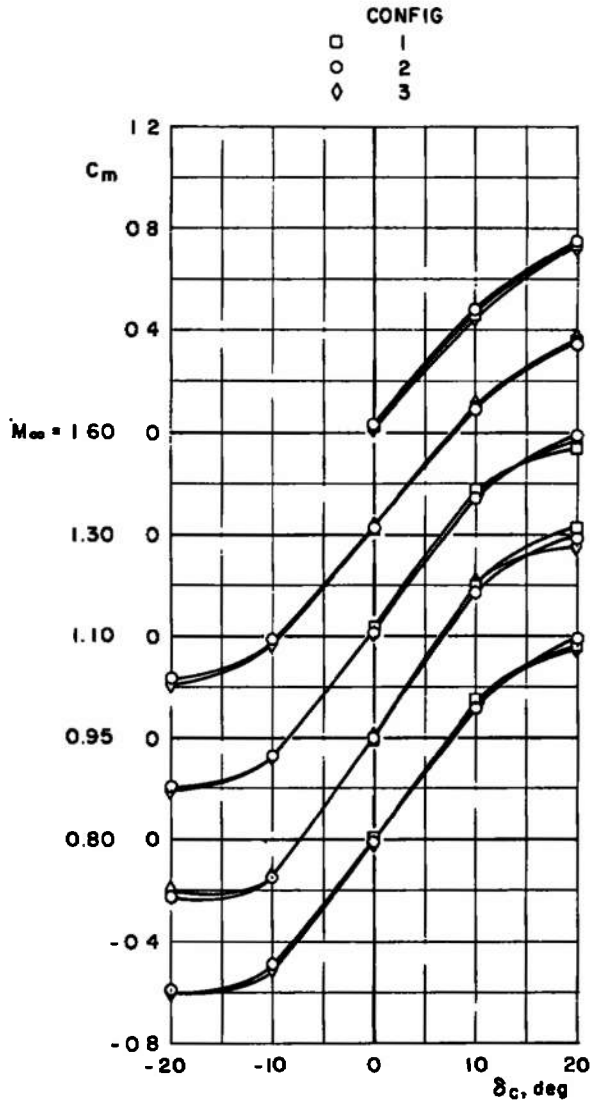
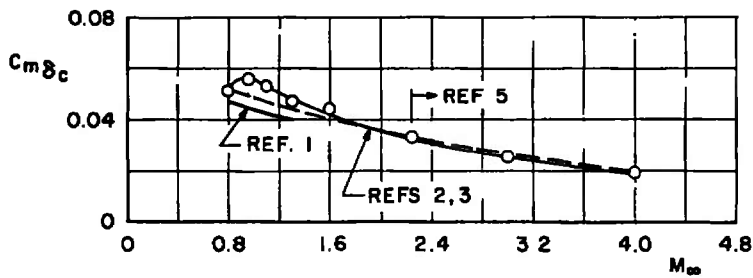


Figure 20. Effects of canards, afterbody, and antennas on $C_{A,F}$, $A_t = 0.505 \text{ in.}^2$, $\delta_a = \alpha = \beta = 0$.



a. C_m versus δ_c , $\alpha = 0$



b. $C_m \delta_c$ versus M_∞ , $\alpha = 0$, configuration 2

Figure 21. Variations of canard effectiveness and trim angle with Mach number, $A_c = 0.505 \text{ in.}^2$, $\delta_a = \beta = 0$.

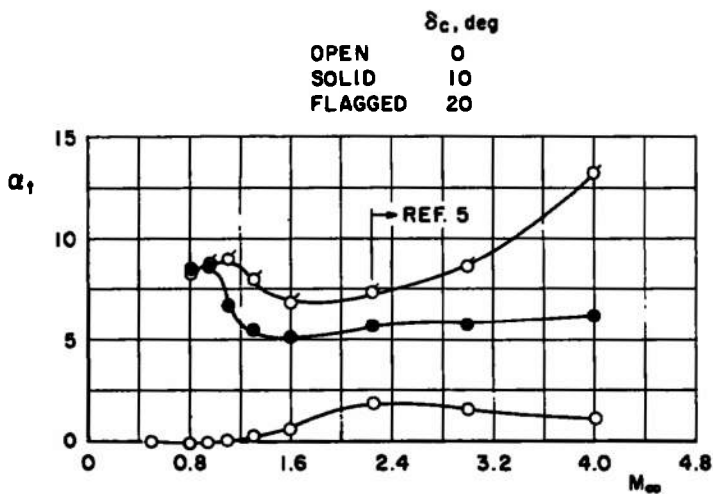
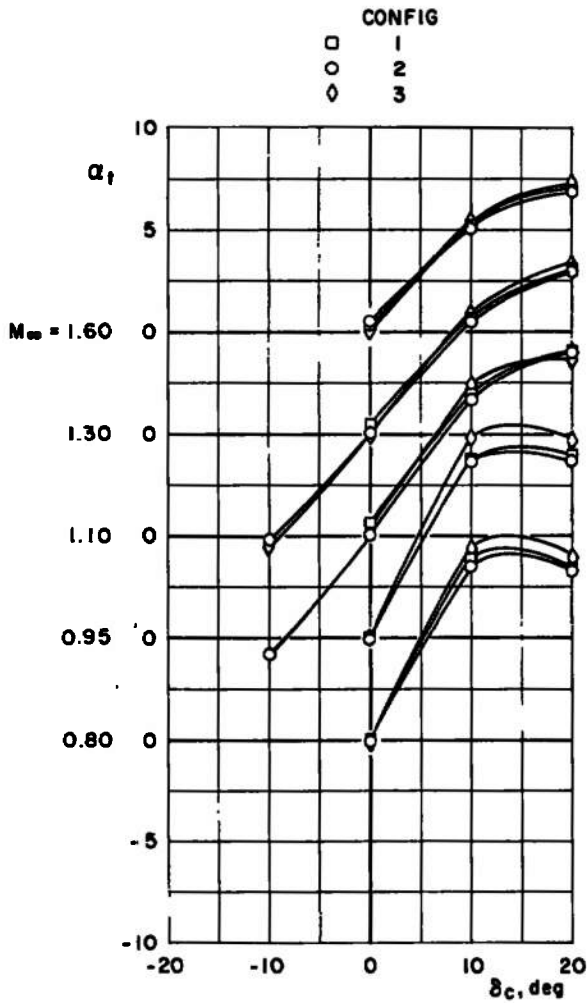
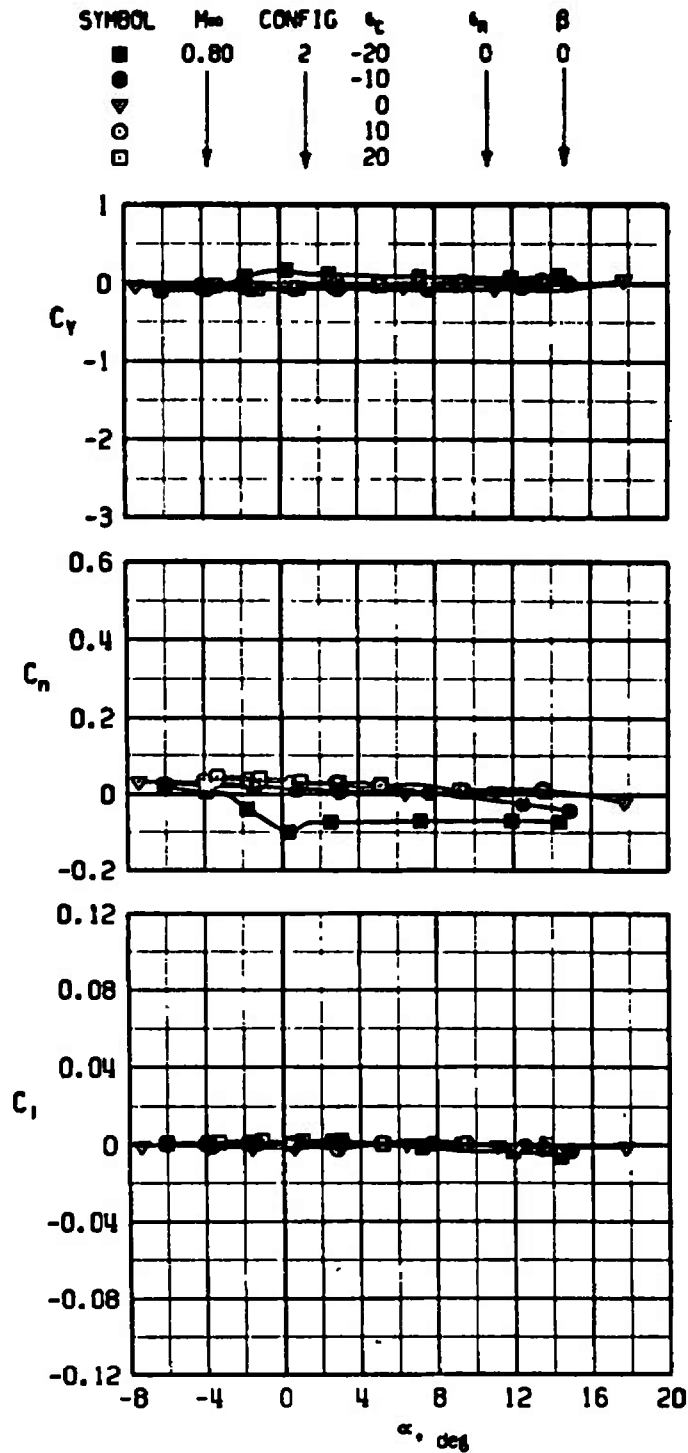


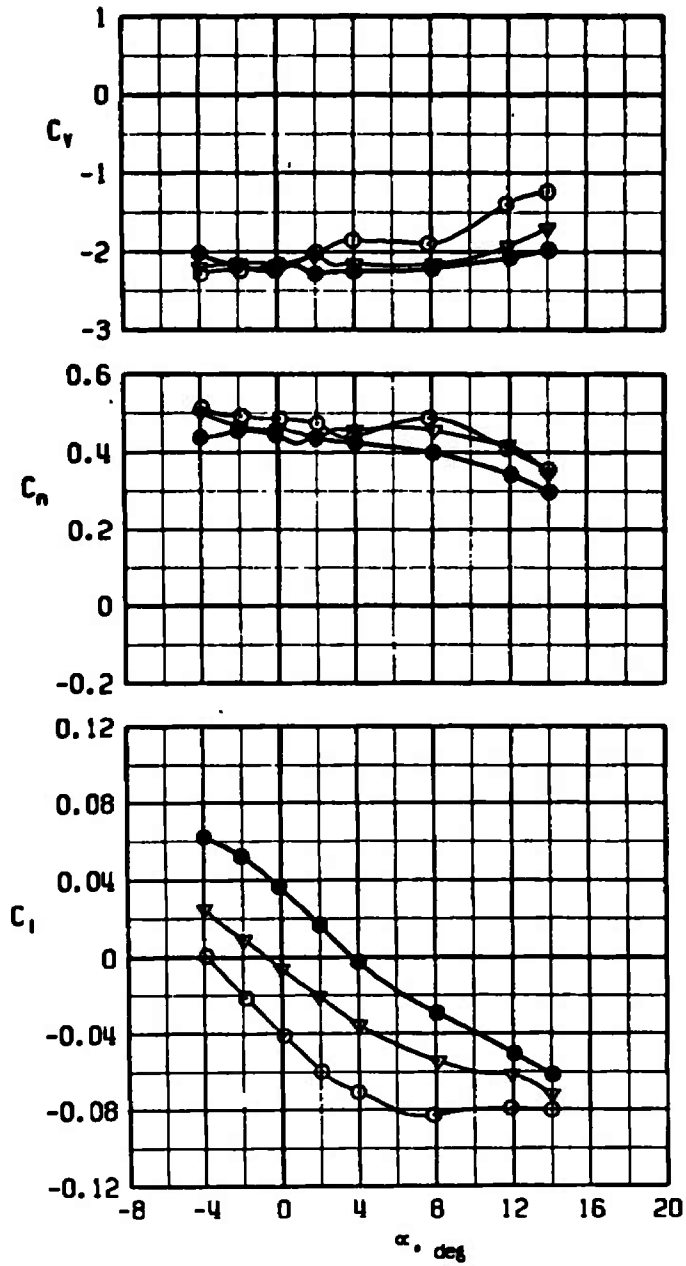
Figure 21. Concluded.



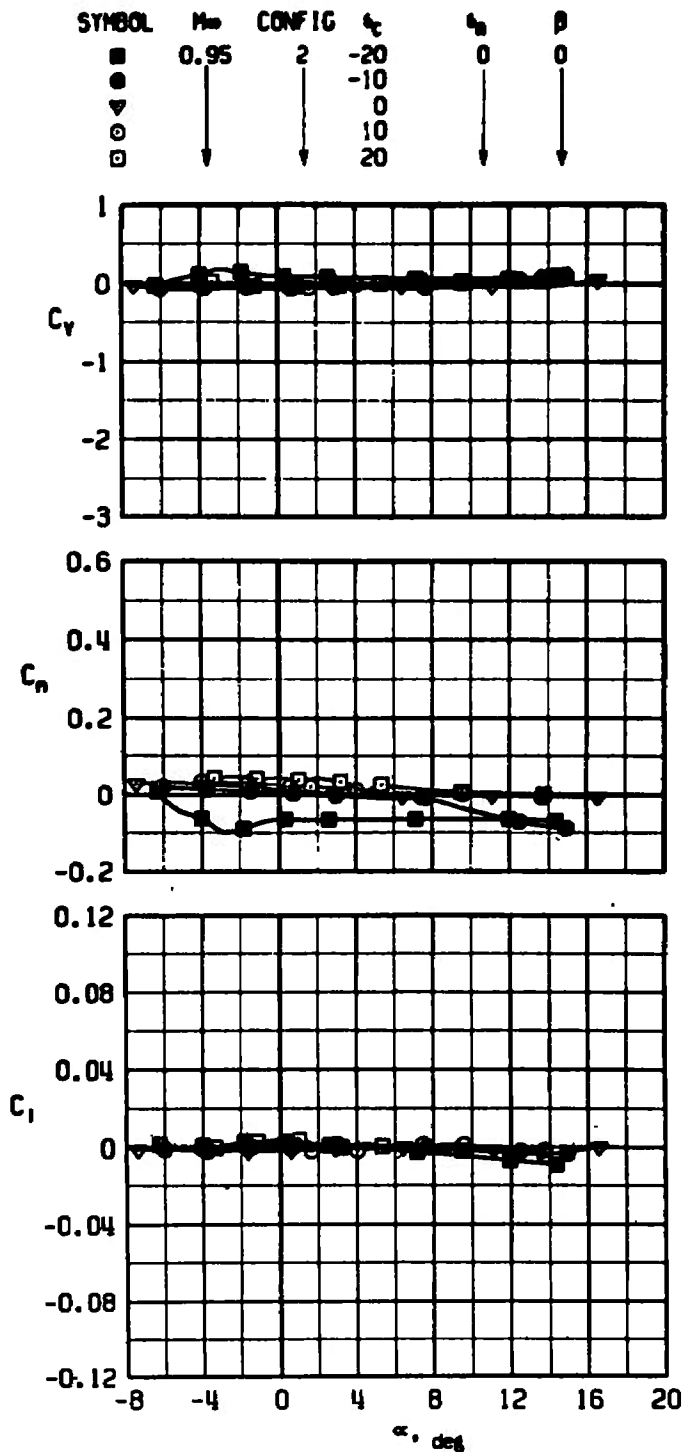
a. $\beta = 0$

Figure 22. Effects of canard deflection on the side-force, yawing-moment, and rolling-moment coefficients, $M_{\infty} = 0.8$, $A_c = 0.505 \text{ in.}^2$, $\delta_a = 0$, configuration 2.

SYMBOL	M _∞	CONFIG	ϵ_z	ϵ_n	β
●	0.80	2	-10	0	6
▼	↓	↓	0	↓	↓
○	↓	↓	10	↓	↓



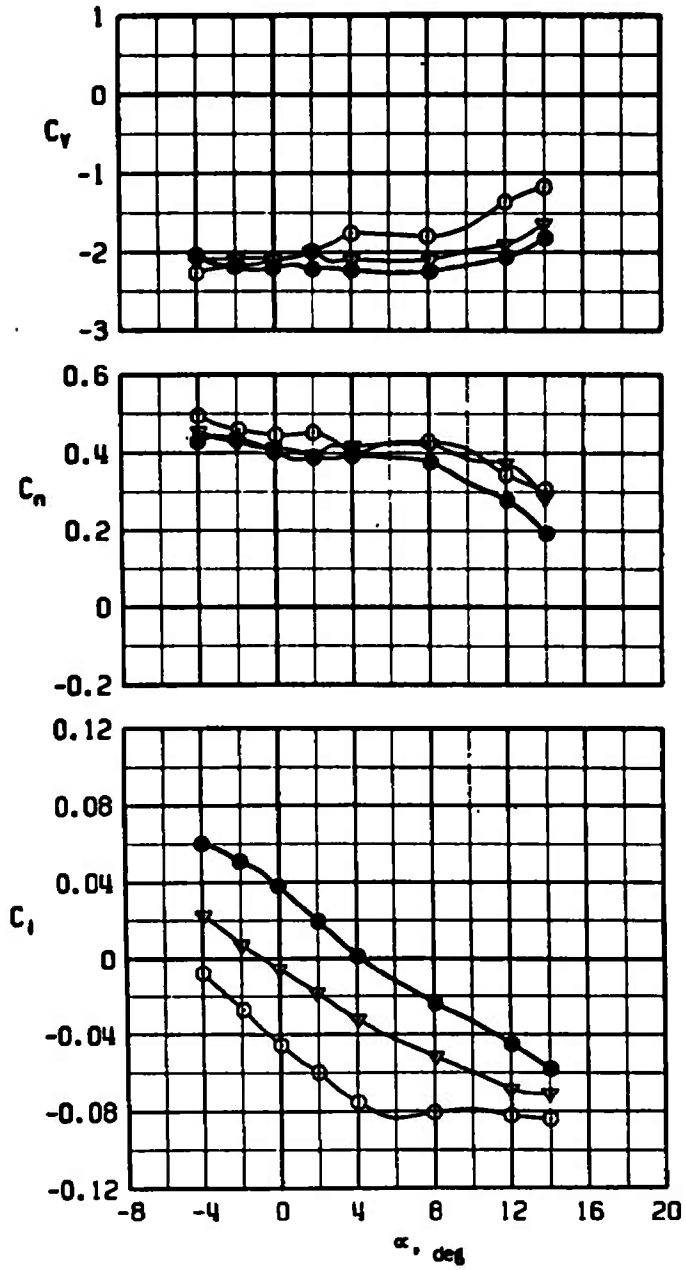
b. $\beta = 6$ deg
 Figure 22. Concluded.



a. $\beta = 0$

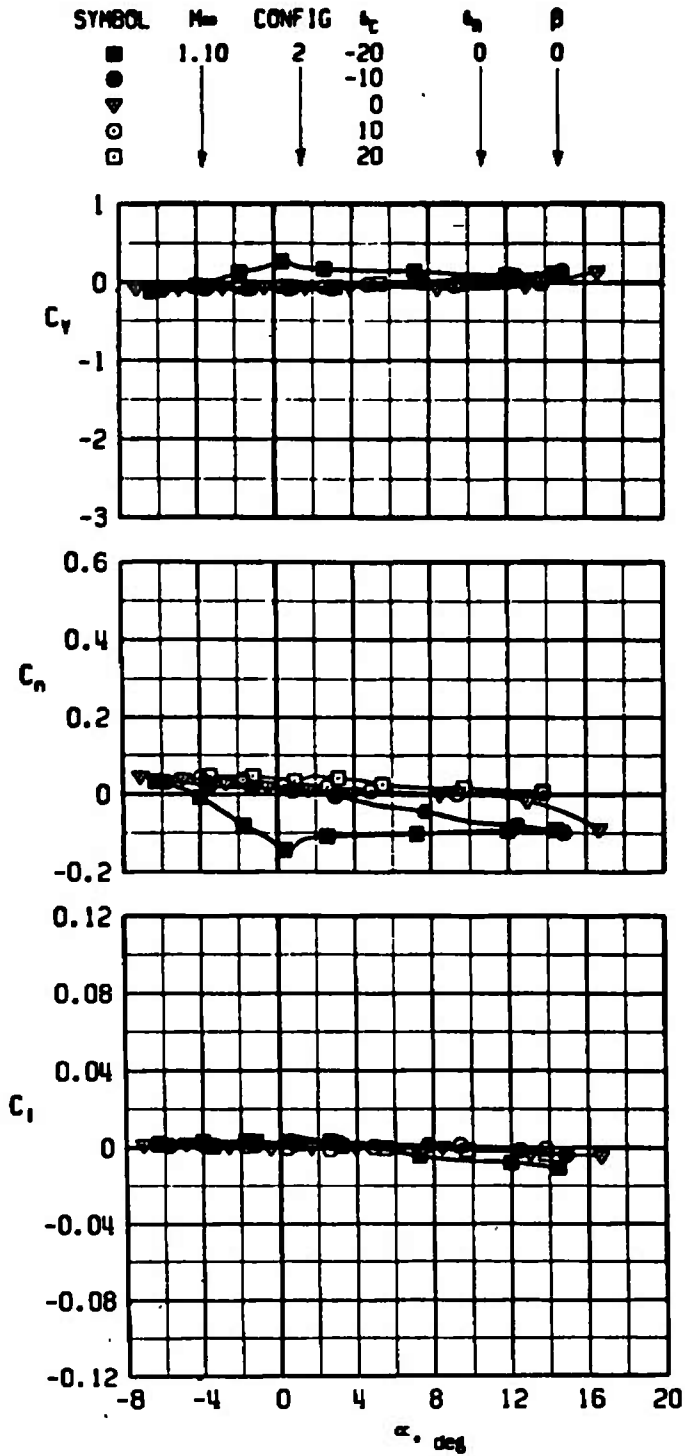
Figure 23. Effects of canard deflection on the side-force, yawing-moment, and rolling-moment coefficients, $M_\infty = 0.95$, $A_t = 0.505 \text{ in.}^2$, $\delta_s = 0$, configuration 2.

SYMBOL	M _∞	CONFIG	α _c	α _n	β
●	0.95	2	-10	0	6
▼	↓	↓	0	↓	↓
○	↓	↓	10	↓	↓



δ_{α_c}
 $\beta = 6$

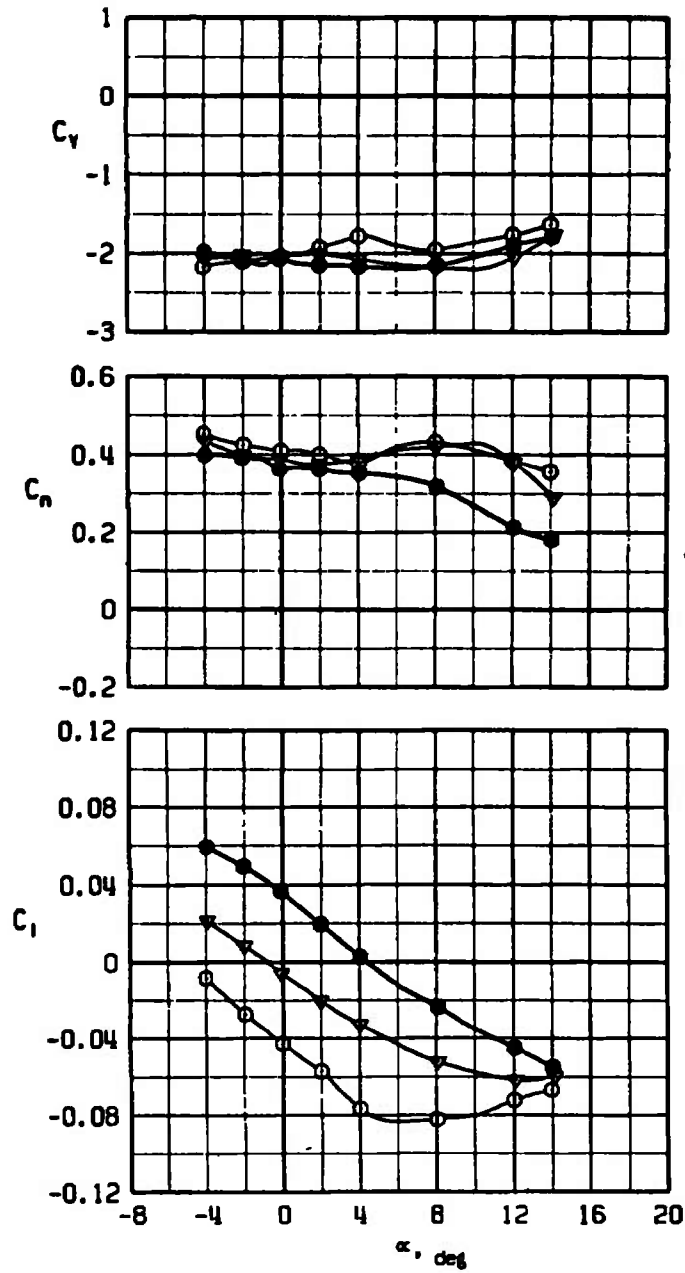
b. $\beta = 6$ deg
 Figure 23. Concluded.



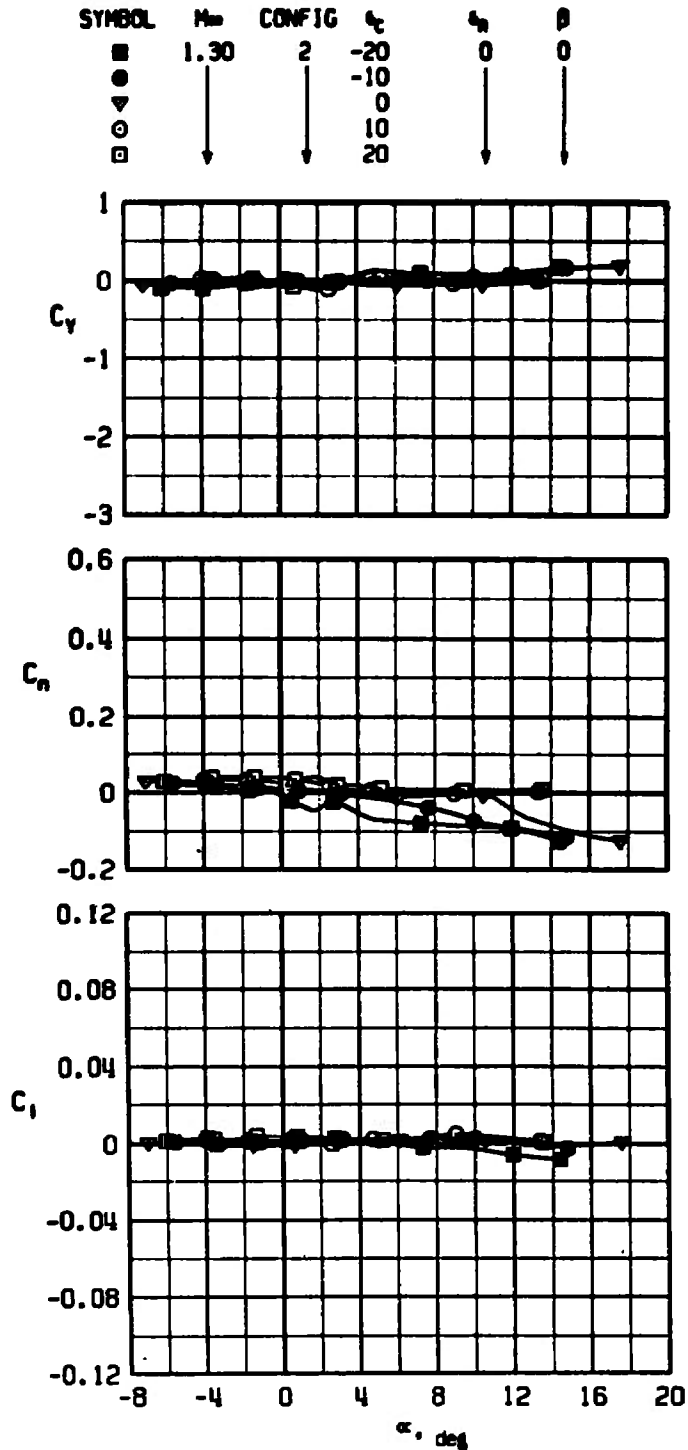
a. $\beta = 0$

Figure 24. Effects of canard deflection on the side-force, yawing-moment, and rolling-moment coefficients, $M_\infty = 1.1$, $A_t = 0.505 \text{ in.}^2$, $\delta_a = 0$, configuration 2.

SYMBOL	M _∞	CONFIG	α _c	α _n	β
●	1.10	2	-10	0	6
▽	↓	↓	0	↓	↓
○	↓	↓	10	↓	↓



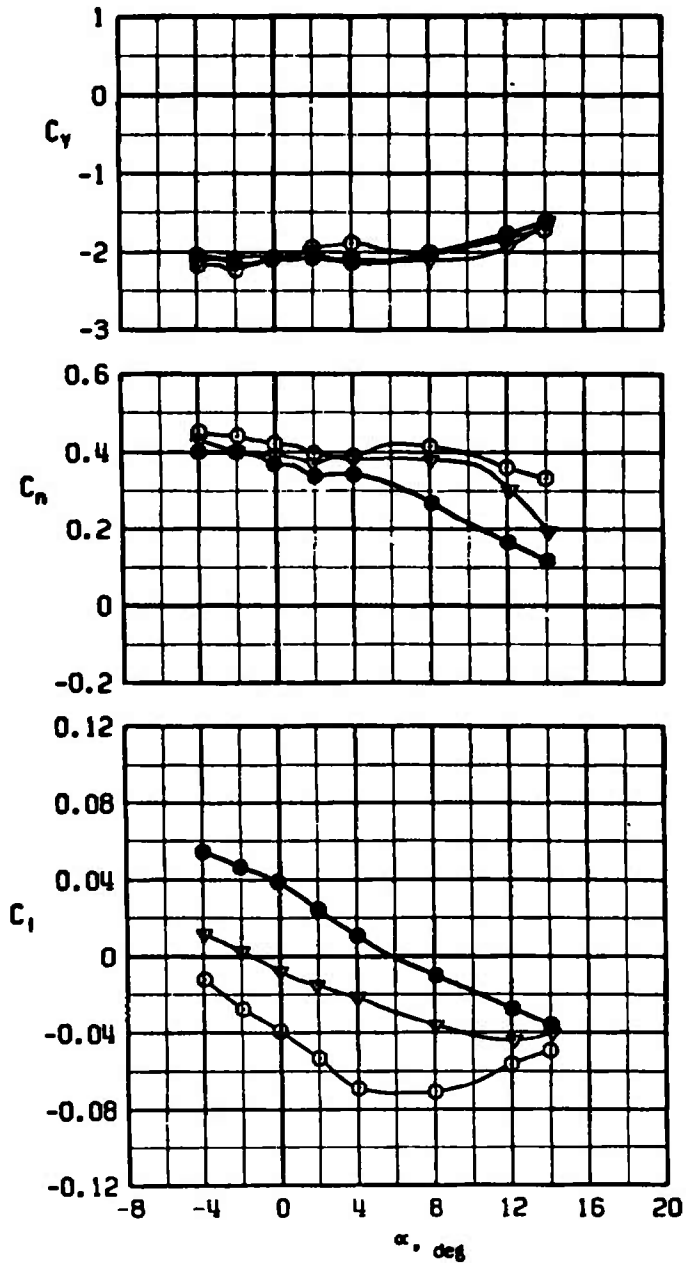
b. $\beta = 6$ deg
 Figure 24. Concluded.



a. $\beta = 0$

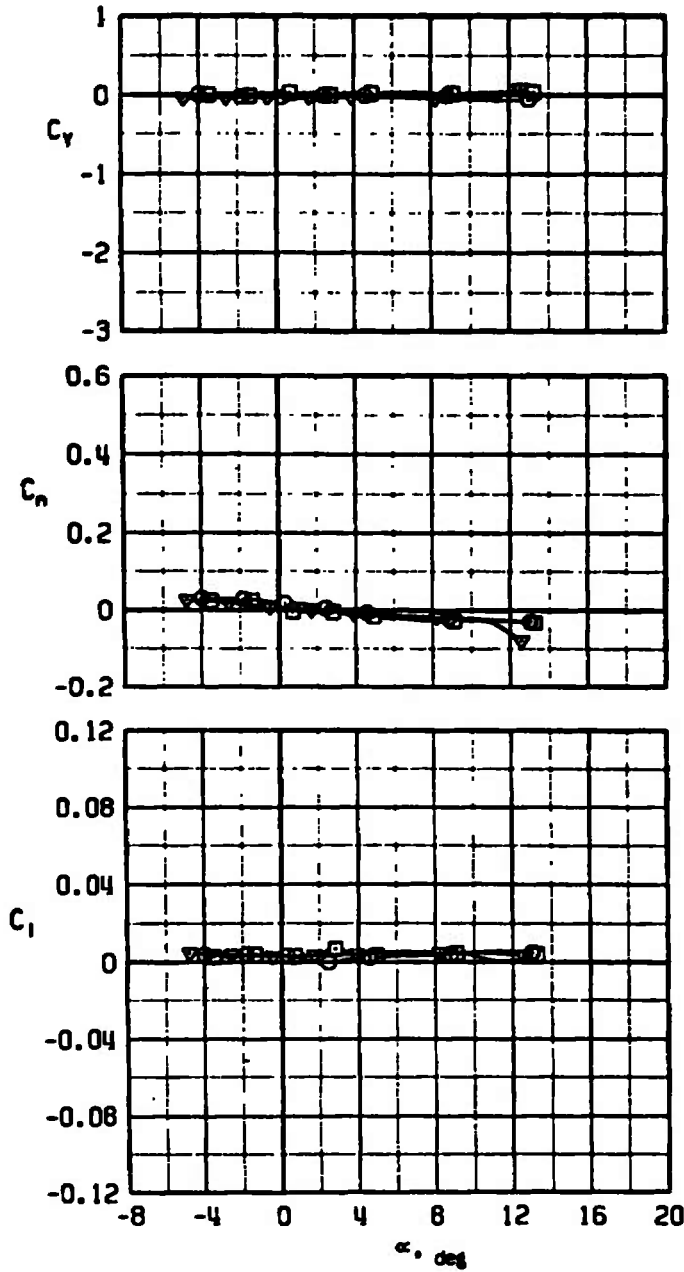
Figure 25. Effects of canard deflection on the side-force, yawing-moment, and rolling-moment coefficients, $M_\infty = 1.3$, $A_t = 0.505 \text{ in.}^2$, $\delta_a = 0$, configuration 2.

SYMBOL	M _∞	CONFIG	α _c	α _n	β
●	1.30	2	-10	0	6
▽	↓	↓	0	↓	↓
○	↓	↓	10	↓	↓



b. $\beta = 6$ deg
 Figure 25. Concluded.

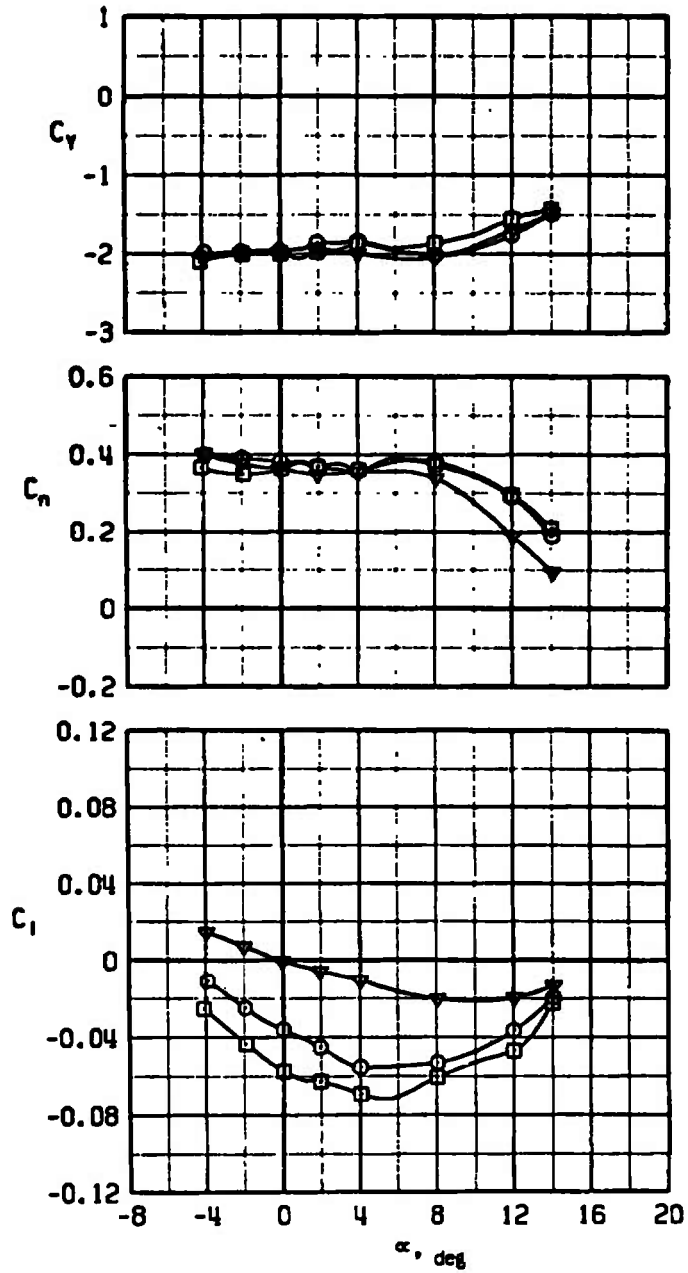
SYMBOL	M_{∞}	CONFIG	t_c	t_n	β
▽	1.60	2	0	0	0
○	↓	↓	10	↓	↓
□	↓	↓	20	↓	



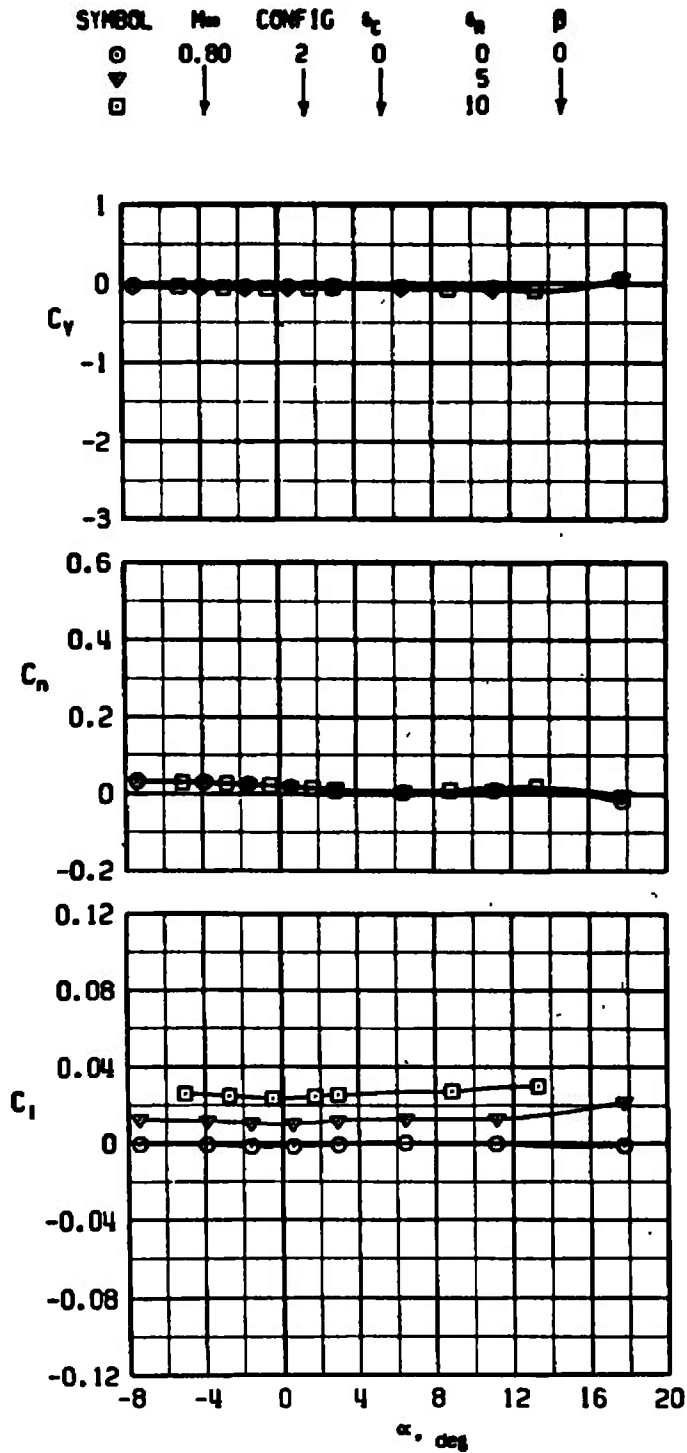
a. $\beta = 0$

Figure 26. Effects of canard deflection on the side-force, yawing-moment, and rolling-moment coefficients, $M_{\infty} = 1.6$, $A_t = 0.505 \text{ in.}^2$, $\delta_s = 0$, configuration 2.

SYMBOL	M _∞	CONFIG	t _c	t _w	β
▽	1.60	2	0	0	6
○	↓	↓	10	↓	↓
□	↓	↓	20	↓	↓



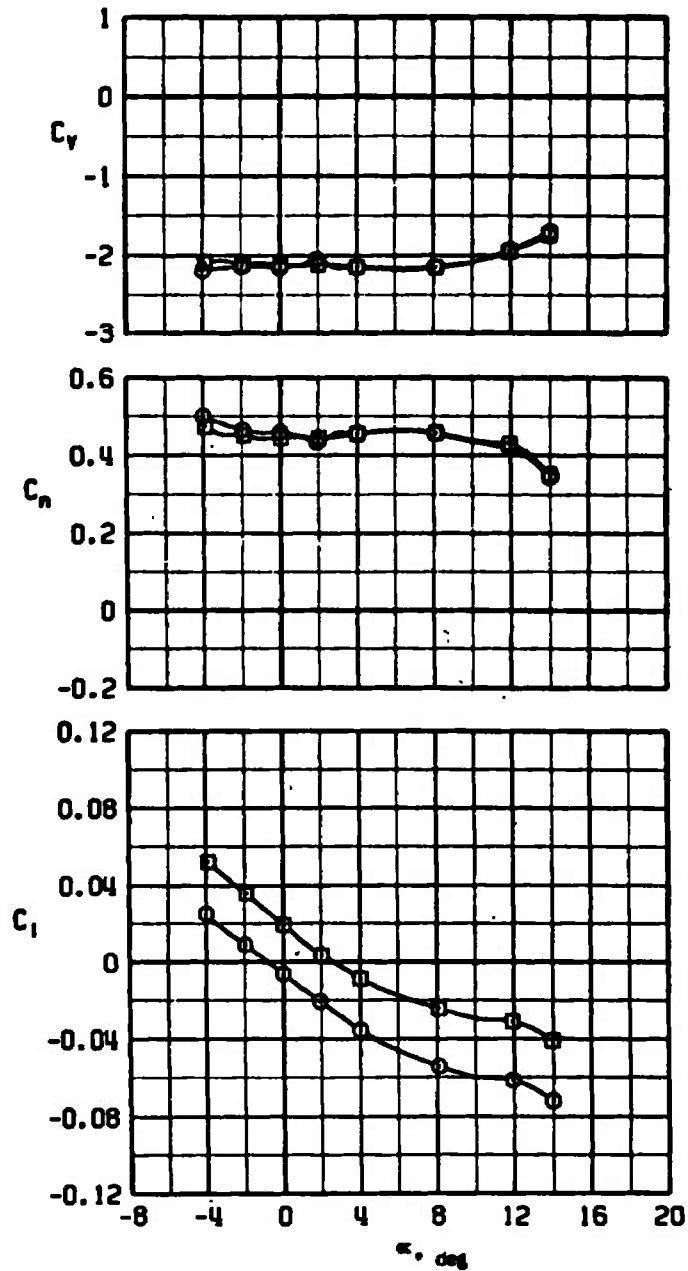
b. $\beta = 6$ deg
 Figure 26. Concluded.



a. $\beta = 0$

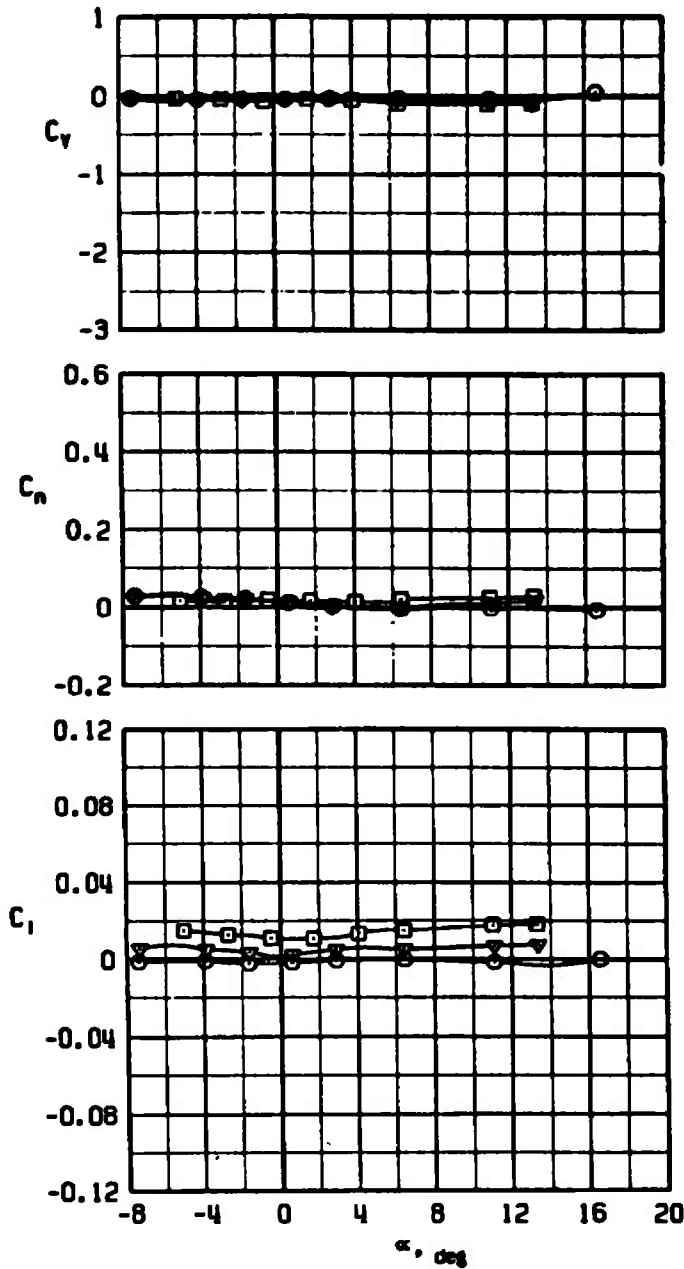
Figure 27. Effects of aileron deflection on the side-force, yawing-moment, and rolling-moment coefficients, $M_{\infty} = 0.8$, $A_t = 0.505 \text{ in.}^2$, $\delta_c = 0$, configuration 2.

SYMBOL	M _∞	CONFIG	t _c	t _n	β
○	0.80	2	0	0	6
□	↓	↓	↓	10	↓



b. $\beta = 6$ deg
 Figure 27. Concluded.

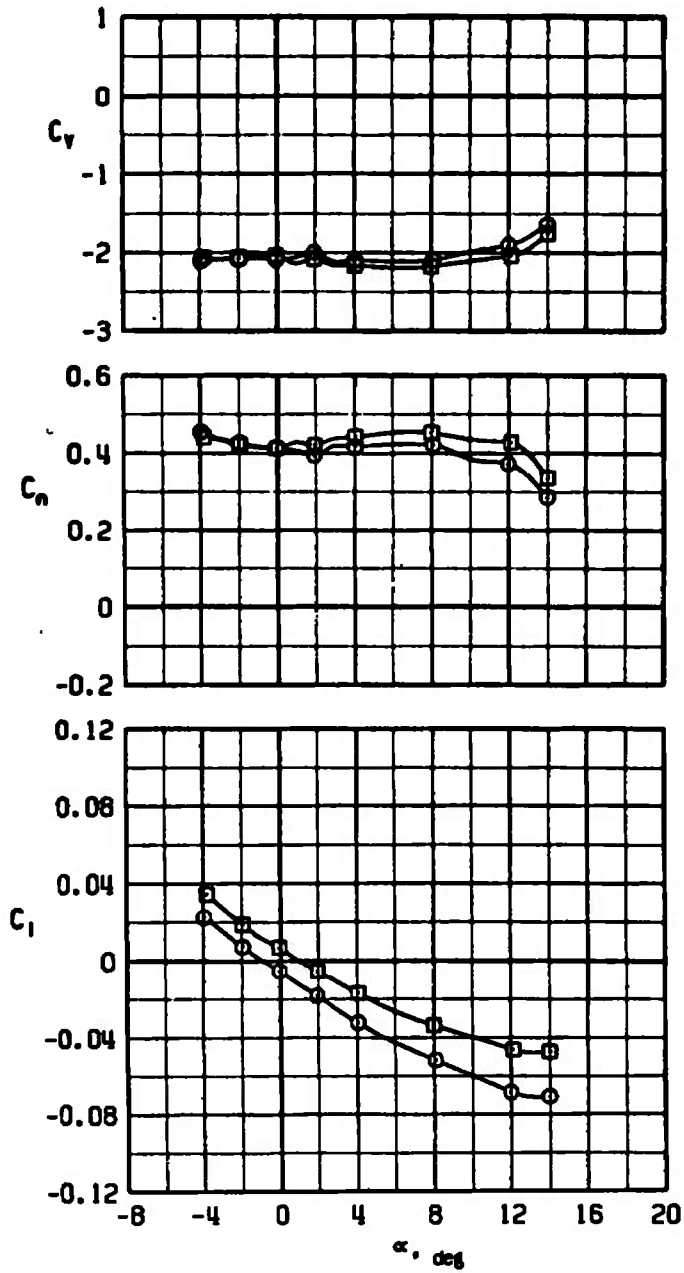
SYMBOL	M_∞	CONFIG	δ_c	A_t	β
○	0.95	2	0	0	0
▼	↓	↓	↓	5	↓
□	↓	↓	↓	10	↓



a. $\beta = 0$

Figure 28. Effects of aileron deflection on the side-force, yawing-moment, and rolling-moment coefficients, $M_\infty = 0.95$, $A_t = 0.505 \text{ in.}^2$, $\delta_c = 0$, configuration 2.

SYMBOL	M _∞	CONFIG	t _c	t _n	β
○	0.95	2	0	0	6
□	↓	↓	↓	10	↓



b. $\beta = 6$ deg
 Figure 28. Concluded.

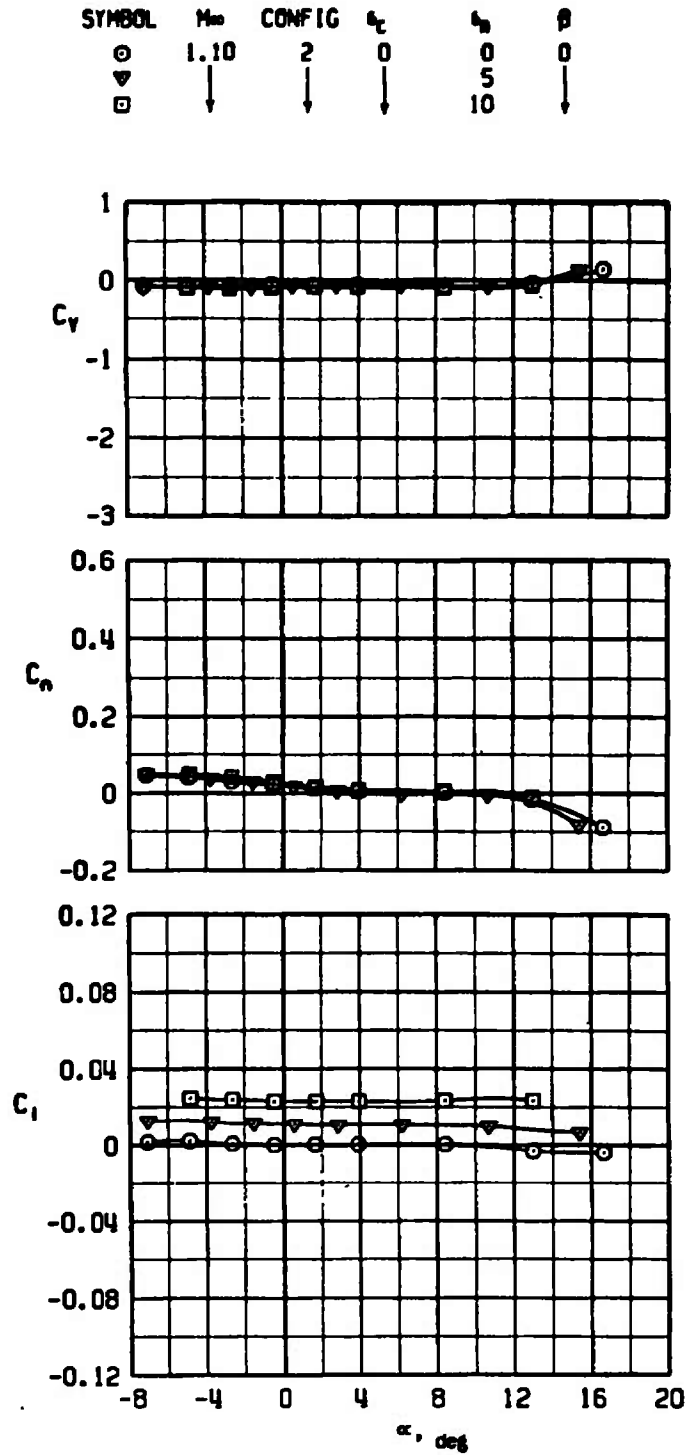
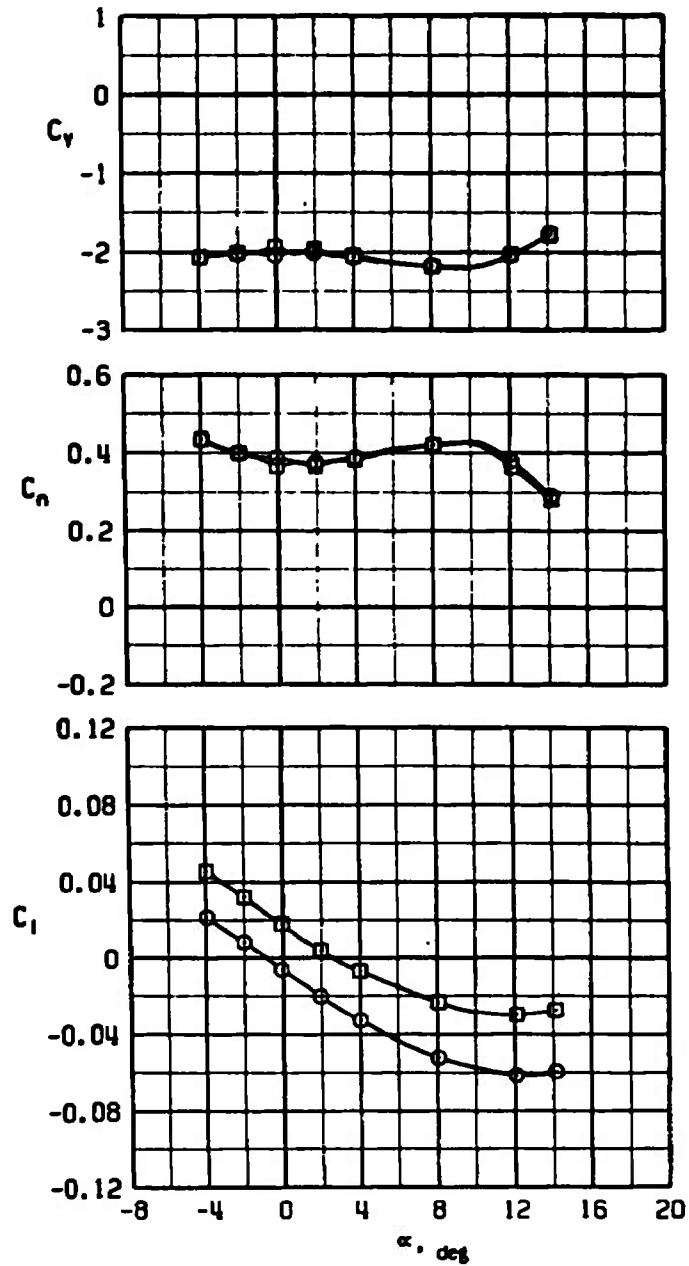


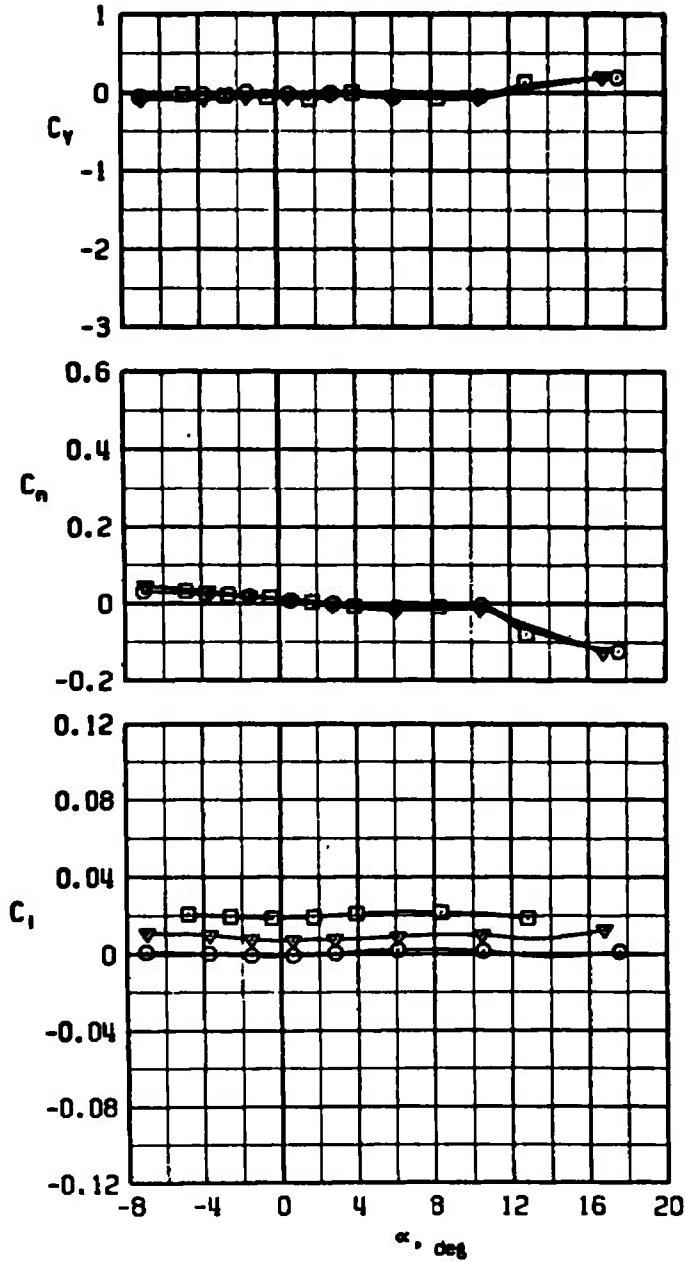
Figure 29. Effects of aileron deflection on the side-force, yawing-moment, and rolling-moment coefficients, $M_{\infty} = 1.1$, $A_t = 0.505 \text{ in.}^2$, $\delta_c = 0$, configuration 2.

SYMBOL	M _∞	CONFIG	ϵ_c	ϵ_n	β
○	1.10	2	0	0	6
□	↓	↓	↓	10	↓



b. $\beta = 6$ deg
 Figure 29. Concluded.

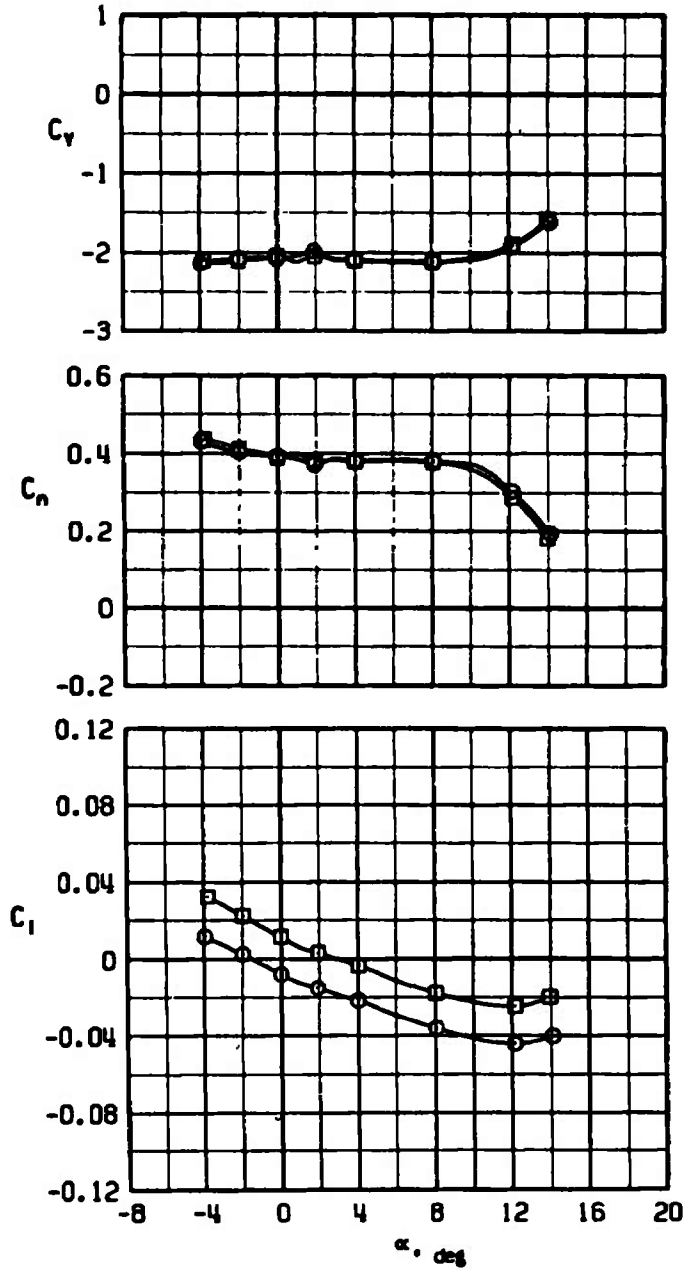
SYMBOL	M_∞	CONFIG	δ_c	A_t	β
○	1.30	2	0	0	0
▽	↓	↓	↓	5	↓
□	↓	↓	↓	10	↓



a. $\beta = 0$

Figure 30. Effects of aileron deflection on the side-force, yawing-moment, and rolling-moment coefficients, $M_\infty = 1.3$, $A_t = 0.505 \text{ in.}^2$, $\delta_c = 0$, configuration 2.

SYMBOL	M _∞	CONFIG	ε _c	ε _m	β
○	1.30	2	0	0	6
□	↓	↓	↓	10	↓



b. $\beta = 6$ deg
 Figure 30. Concluded.

SYMBOL	M_{∞}	CONFIG	δ_c	δ_n	β
○	1.60	2	0	0	0
□	↓	↓	↓	10	↓

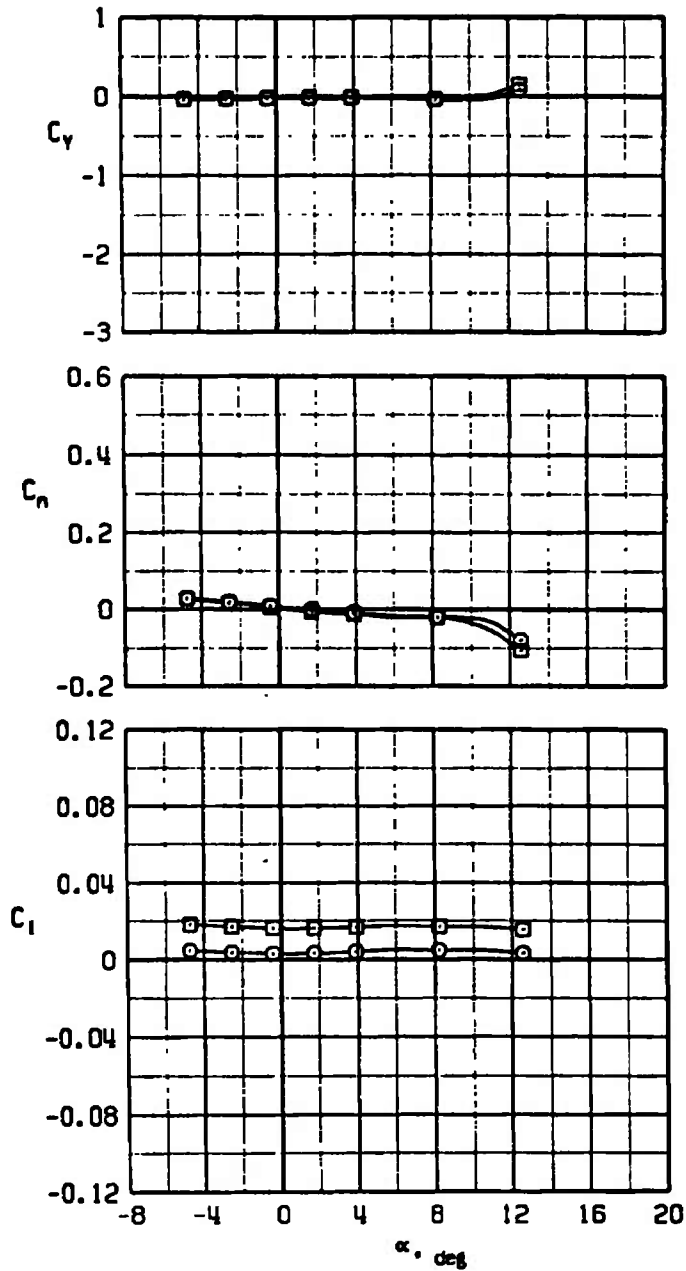


Figure 31. Effects of aileron deflection on the side-force, yawing-moment, and rolling-moment coefficients, $M_{\infty} = 1.6$, $A_t = 0.505 \text{ in.}^2$, $\delta_c = \beta = 0$, configuration 2.

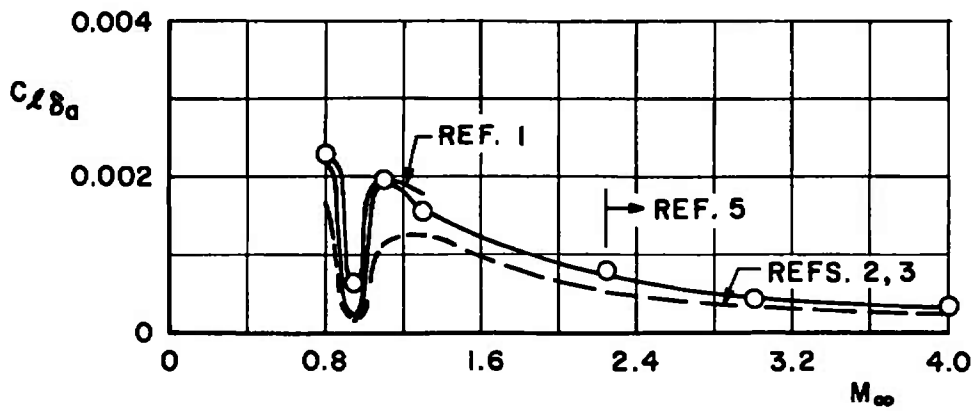
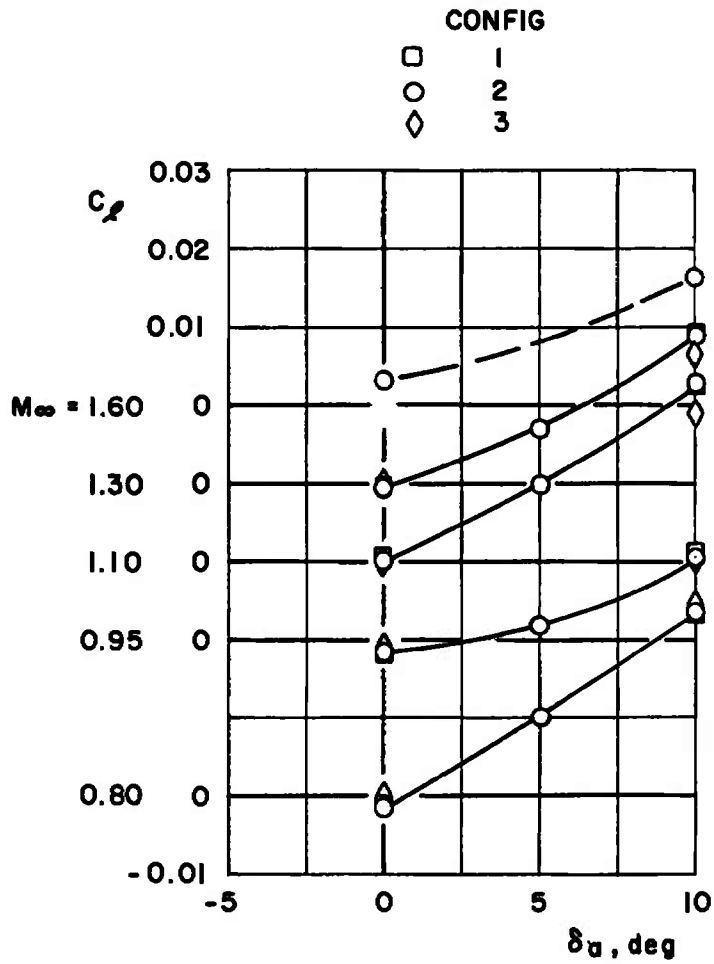
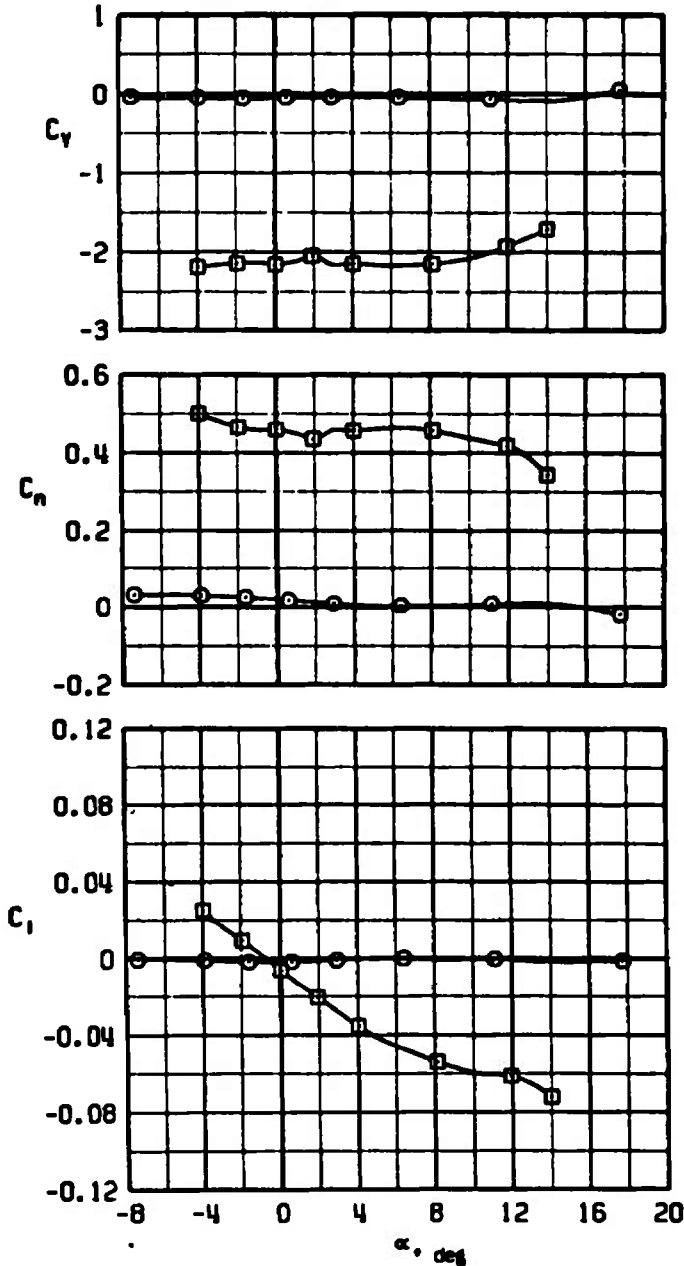


Figure 32. Variation of aileron effectiveness with Mach number, $A_t = 0.505 \text{ in.}^2$, $\delta_c = \alpha = \beta = 0$.

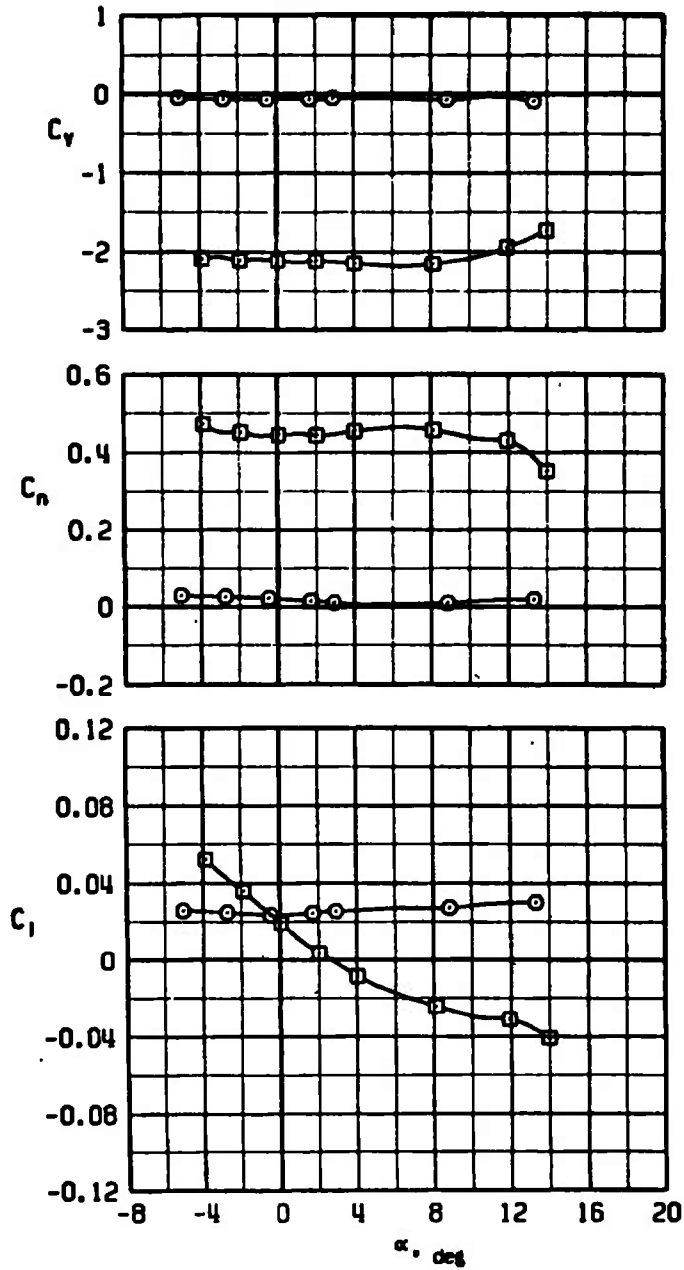
SYMBOL	M_{∞}	CONFIG	δ_c	δ_n	β
○	0.80	2	0	0	0
□	↓	↓	↓	↓	6



a. $\delta_a = 0$

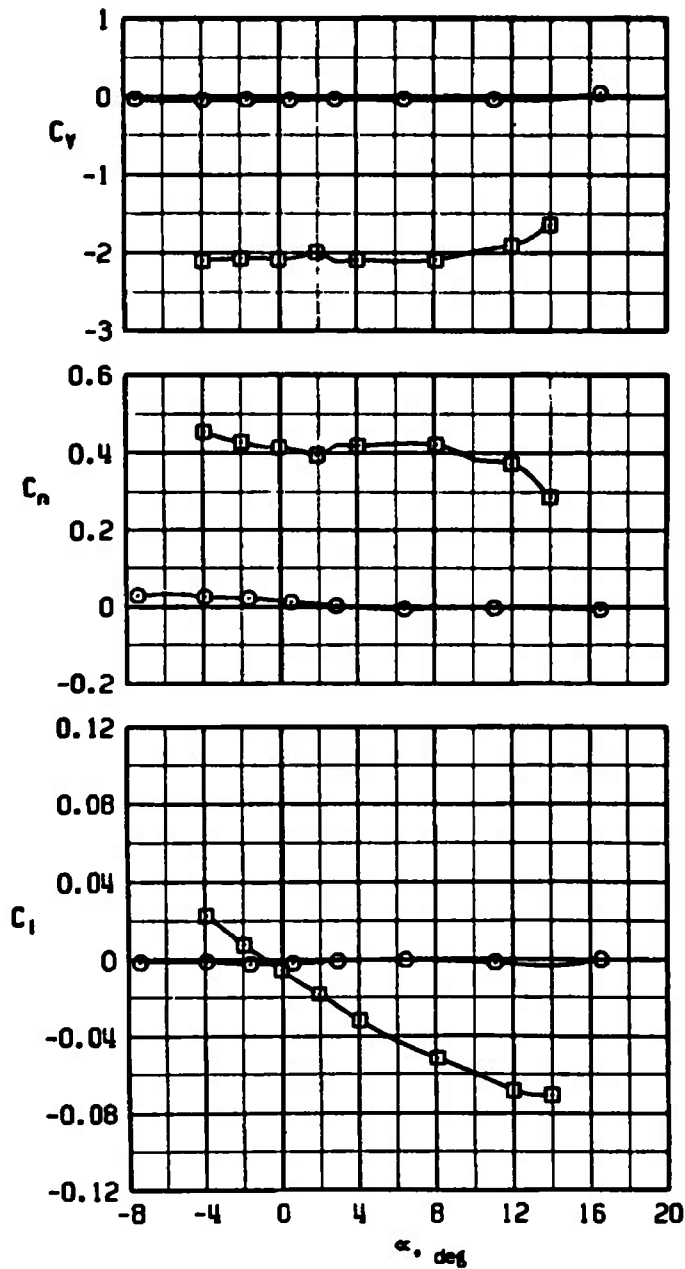
Figure 33. Effect of angle of sideslip on the side-force, yawing-moment, and rolling-moment coefficients, $M_{\infty} = 0.8$, $A_t = 0.505 \text{ in.}^2$, $\delta_c = 0$, configuration 2.

SYMBOL	M _∞	CONFIG	ϵ_c	ϵ_n	β
○	0.80	2	0	10	0
□	↓	↓	↓	↓	6



b. $\delta_s = 10$ deg
 Figure 33. Concluded.

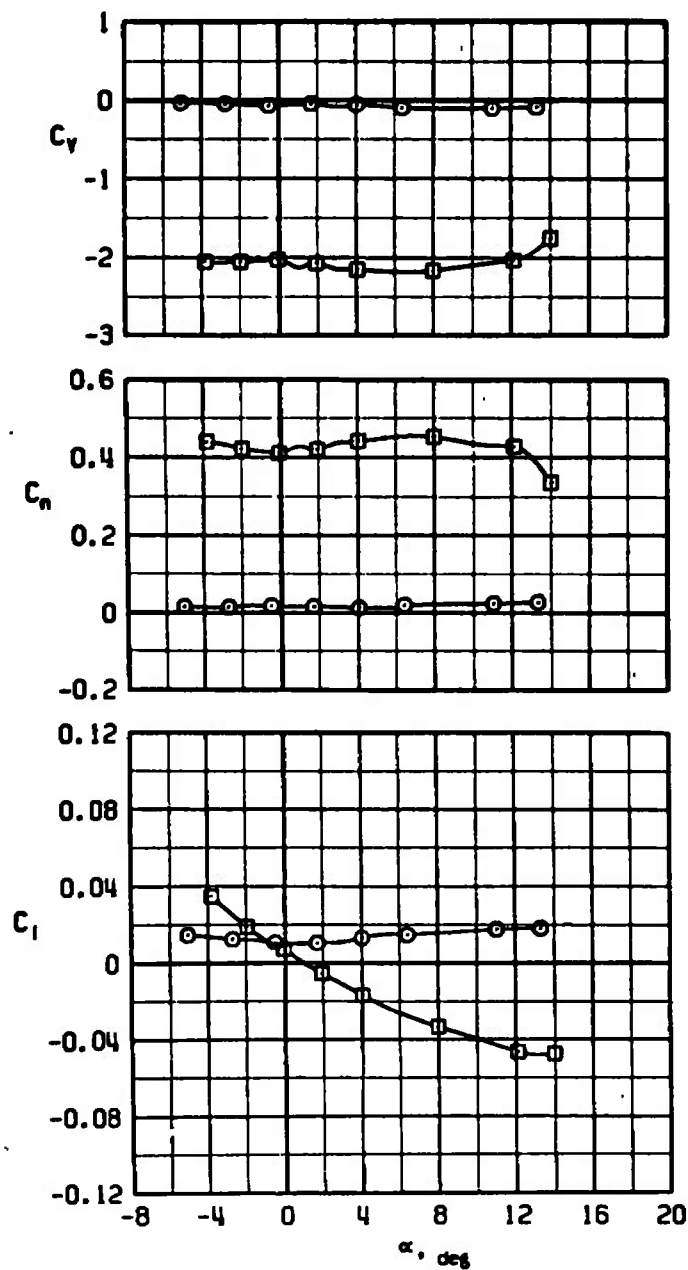
SYMBOL	M_∞	CONFIG	ϵ_c	ϵ_n	β
○	0.95	2	0	0	0
□	↓	↓	↓	↓	6



a. $\delta_a = 0$

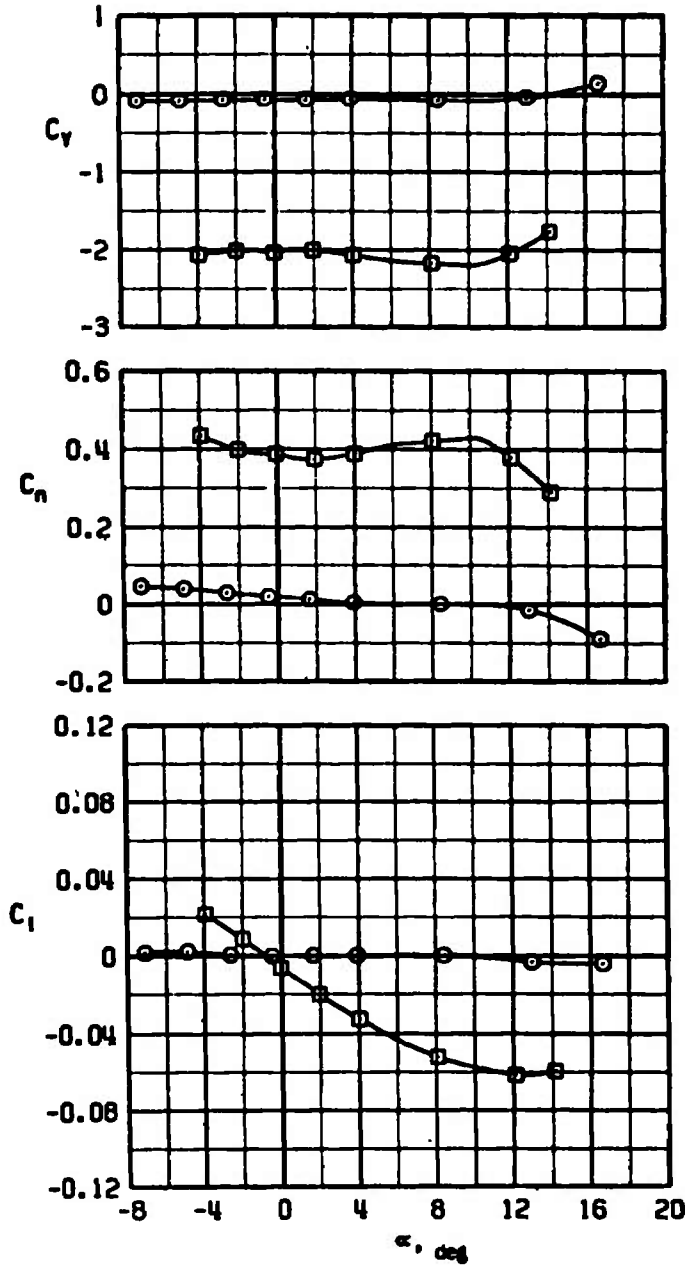
Figure 34. Effect of angle of sideslip on the side-force, yawing-moment, and rolling-moment coefficients, $M_\infty = 0.95$, $A_t = 0.505 \text{ in.}^2$, $\delta_c = 0$, configuration 2.

SYMBOL	M _∞	CONFIG	t _c	t _n	β
○	0.95	2	0	10	0
□					6



b. $\delta_a = 10$ deg
 Figure 34. Concluded.

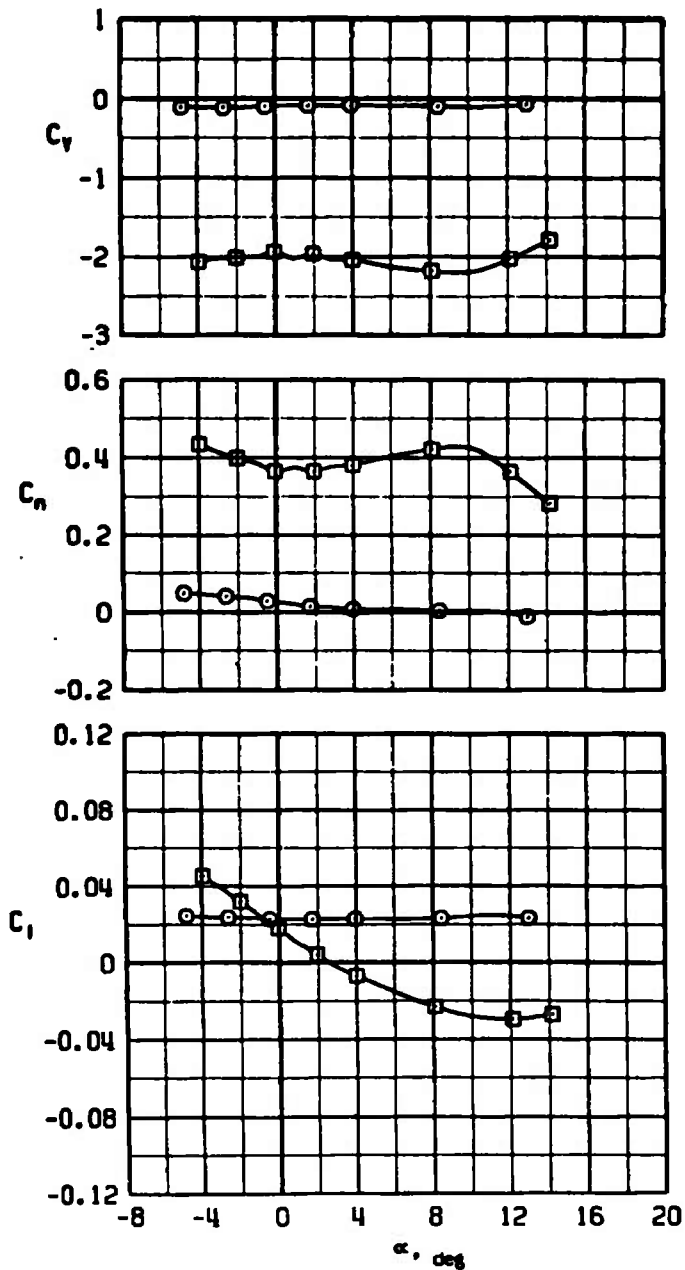
SYMBOL	M_{∞}	CONFIG	δ_c	δ_n	β
○	1.10	2	0	0	6
□	↓	↓	↓	↓	6



a. $\delta_n = 0$

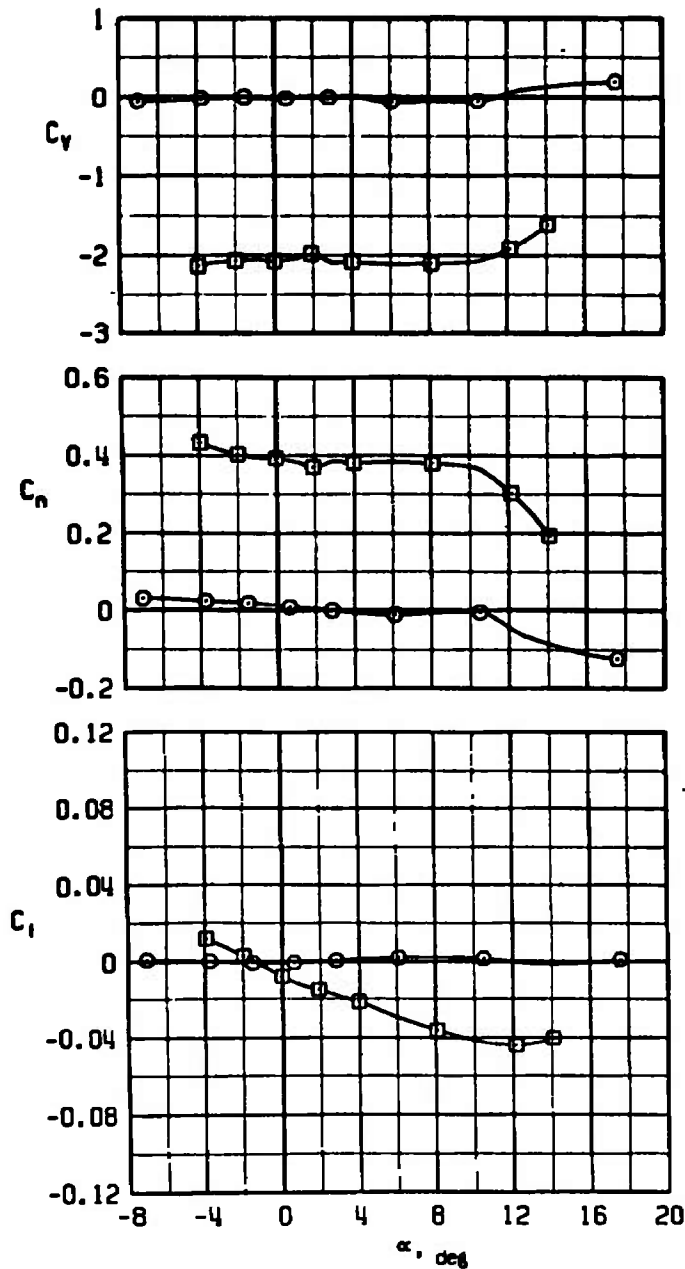
Figure 35. Effect of angle of sideslip on the side-force, yawing-moment, and rolling-moment coefficients, $M_{\infty} = 1.1$, $A_t = 0.505 \text{ in.}^2$, $\delta_c = 0$, configuration 2.

SYMBOL	M _∞	CONFIG	α _c	α ₀	β
○	1.10	2	0	10	0
□					6



b. $\delta_0 = 10$ deg
 Figure 35. Concluded.

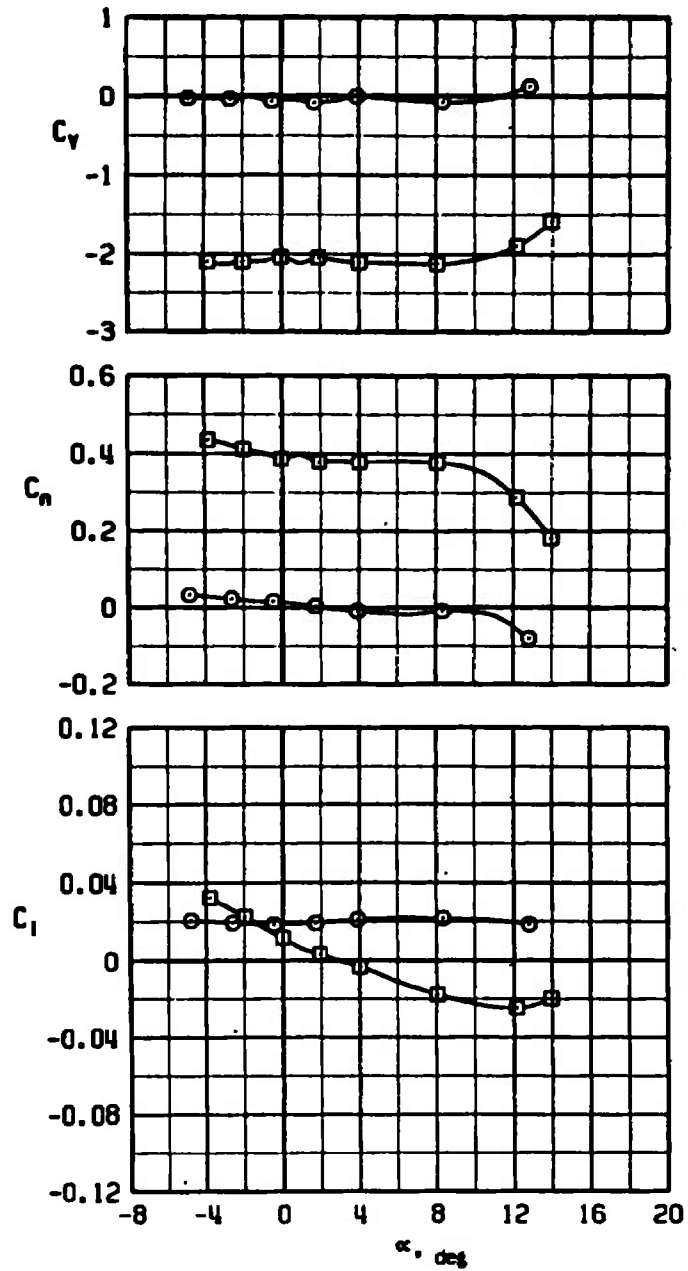
SYMBOL	M_∞	CONFIG	δ_c	δ_a	β
○	1.30	2	0	0	0
□	↓	↓	↓	↓	6



a. $\delta_a = 0$

Figure 36. Effect of angle of sideslip on the side-force, yawing-moment, and rolling-moment coefficients, $M_\infty = 1.3$, $A_t = 0.505 \text{ in.}^2$, $\delta_c = 0$, configuration 2.

SYMBOL	M _∞	CONFIG	ϵ_c	ϵ_n	β
○	1.30	2	0	10	0
□	↓	↓	↓	↓	6



b. $\delta_s = 10$ deg
 Figure 36. Concluded.

SYMBOL	M_{∞}	CONFIG	δ_c	δ_a	β
○	1.60	2	0	0	0
□	↓	↓	↓	↓	6

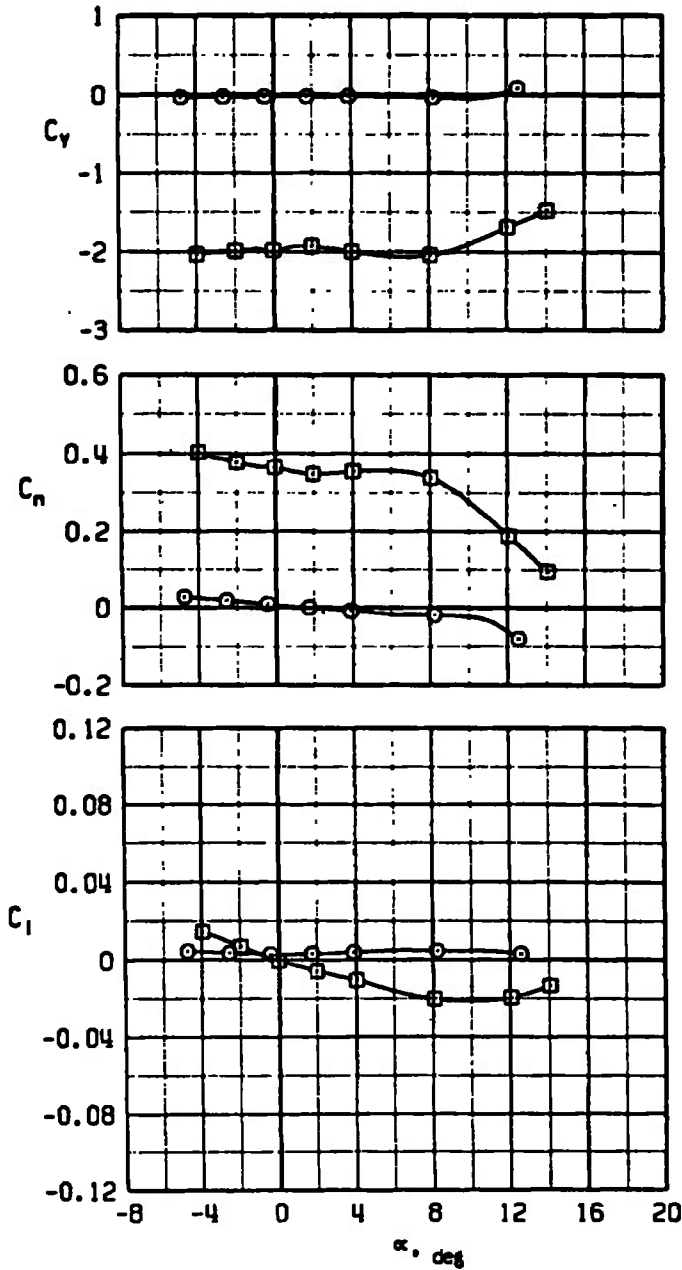
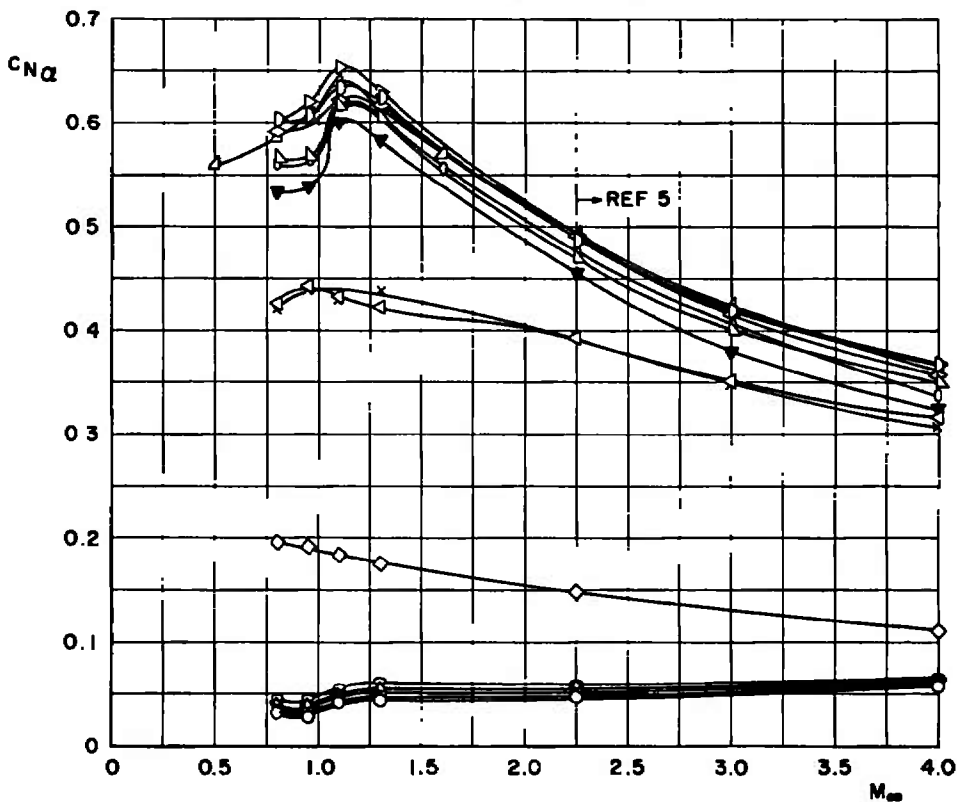


Figure 37. Effect of angle of sideslip on the side-force, yawing-moment, and rolling-moment coefficients, $M_{\infty} = 1.6$, $A_t = 0.50 \text{ in.}^2$, $\delta_c = \delta_a = 0$, configuration 2.

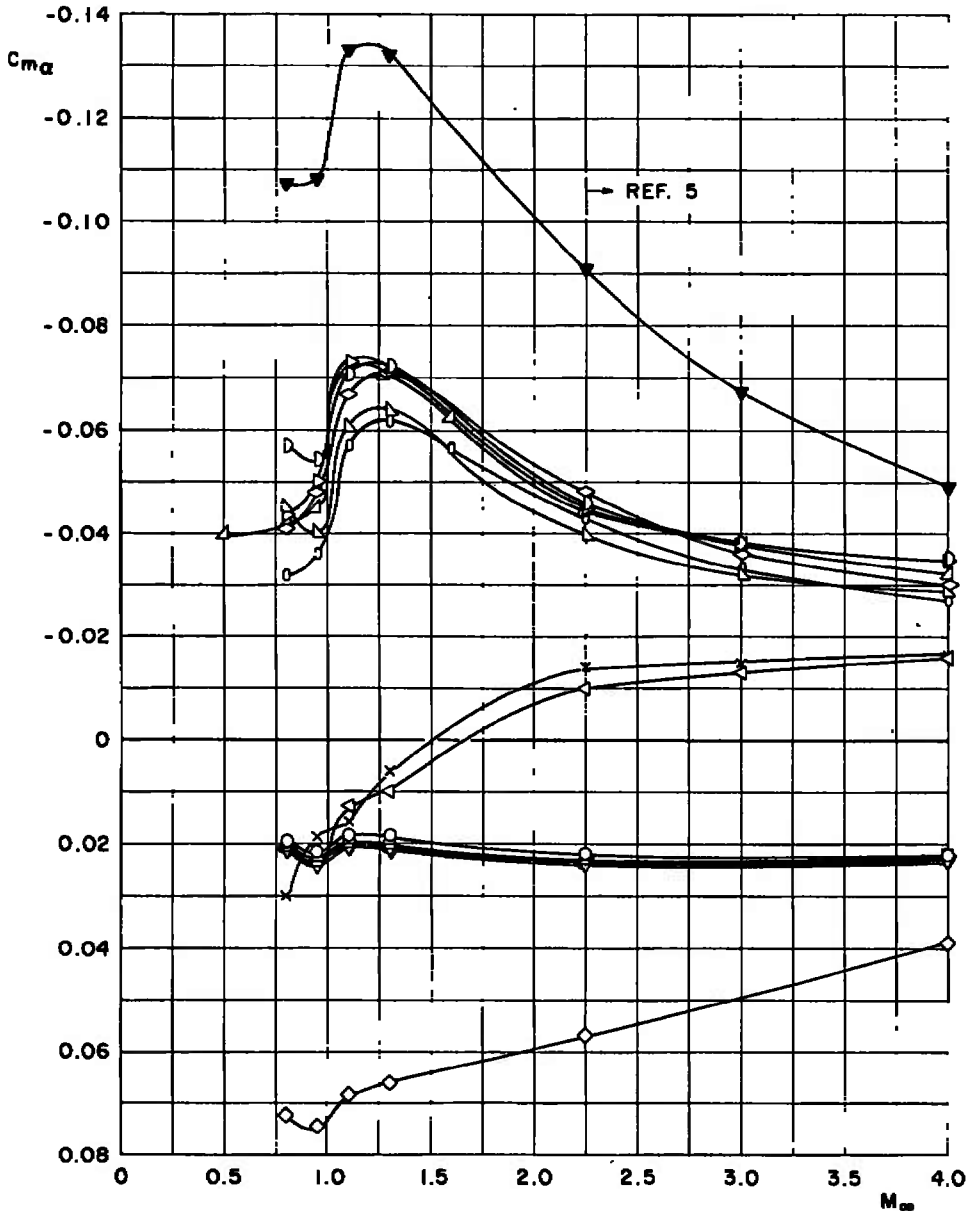
	CONFIG	REMARKS
○	18	CLEAN, OGIVE CYLINDER
△	17	+ PITOT PROBE
□	16	+ C-BAND ANTENNAS
◇	15	+ FOREBODY ANTENNAS
▽	14	+ LAUNCH PINS
◊	13	+ RADOMES
◇	12	+ CANARDS
△	11	+ WINGS
▷	9	+ VERTICAL FINS
▷	8	+ VDMI ANTENNAS
▷	7	+ T5 POD
◇	6	+ INLET AND INLET ANTENNA
△	2	+ T4 AFTERBODY
◻	3	- ALL ANTENNAS
▼	4	- CANARDS
x	5	- VERTICAL FINS + CANARDS



a. $C_{N\alpha}$ versus M_∞

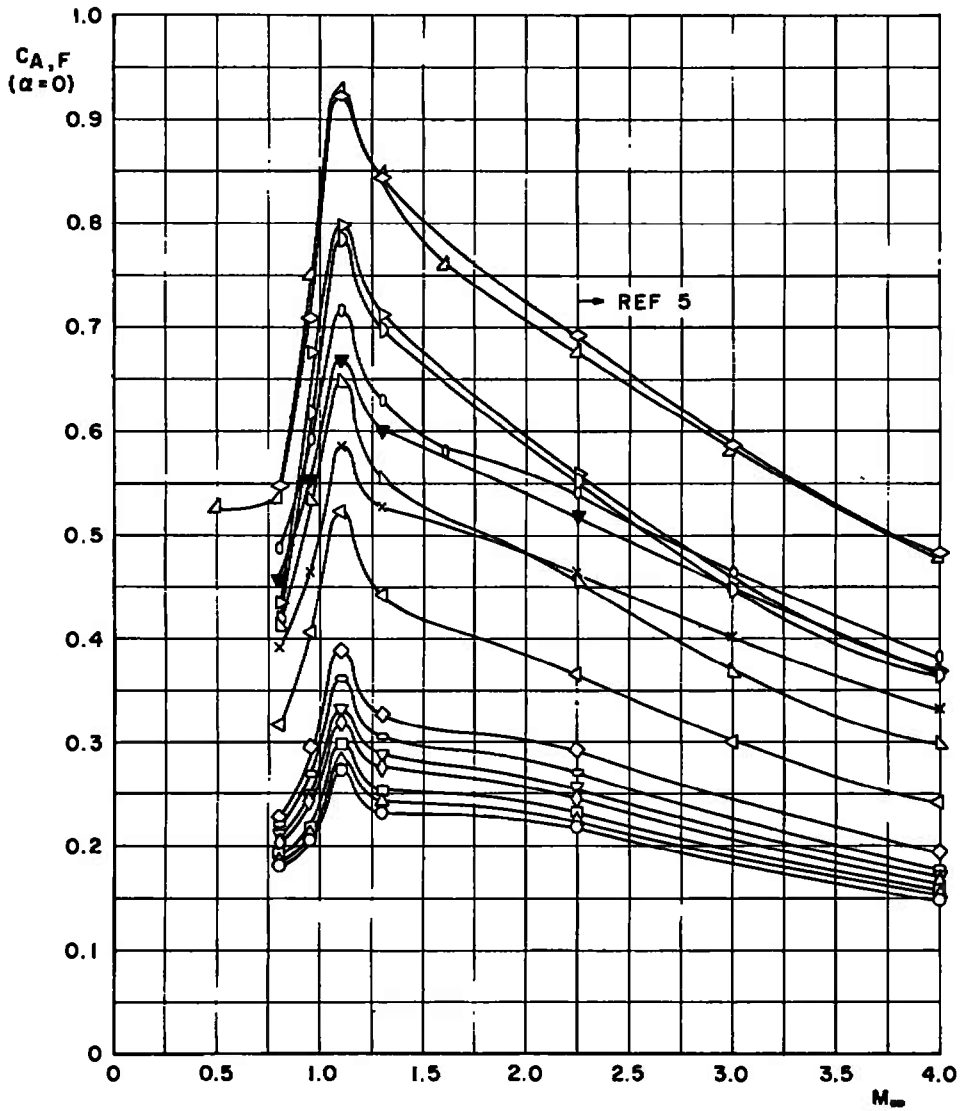
Figure 38. Effects of missile components on the longitudinal stability derivatives and axial-force coefficients at zero angle of attack, $\delta_c = \delta_a = \beta = 0$.

CONFIG	REMARKS	CONFIG	REMARKS
○	18 CLEAN, OGIVE CYLINDER	△	9 + VERTICAL FINNS
△	17 + PITOT PROBE	▷	8 + VDMI ANTENNAS
◻	16 + C-BAND ANTENNAS	▽	7 + T5 POD
◇	15 + FOREBODY ANTENNAS	◊	6 + INLET AND INLET ANTENNA
▽	14 + LAUNCH PINS	△	2 + T4 AFTERBODY
○	13 + RADOMES	○	3 - ALL ANTENNAS
◇	12 + CANARDS	▽	4 - CANARDS
△	11 + WINGS	x	5 - VERTICAL FINNS + CANARDS



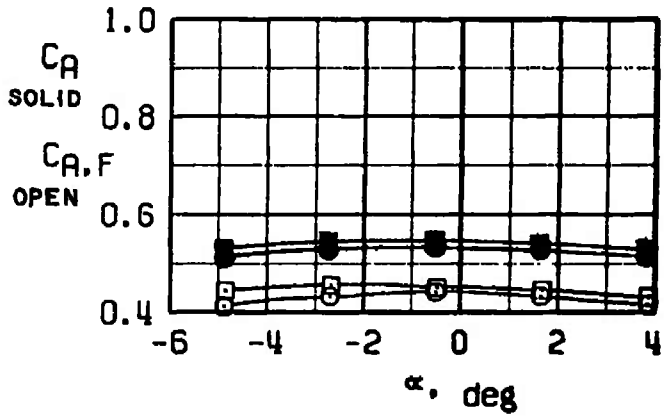
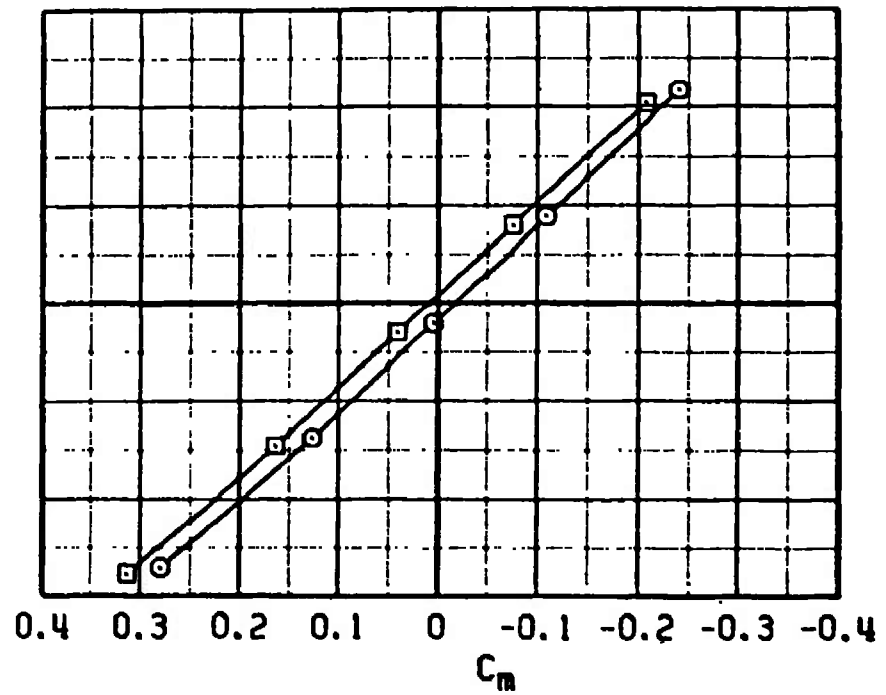
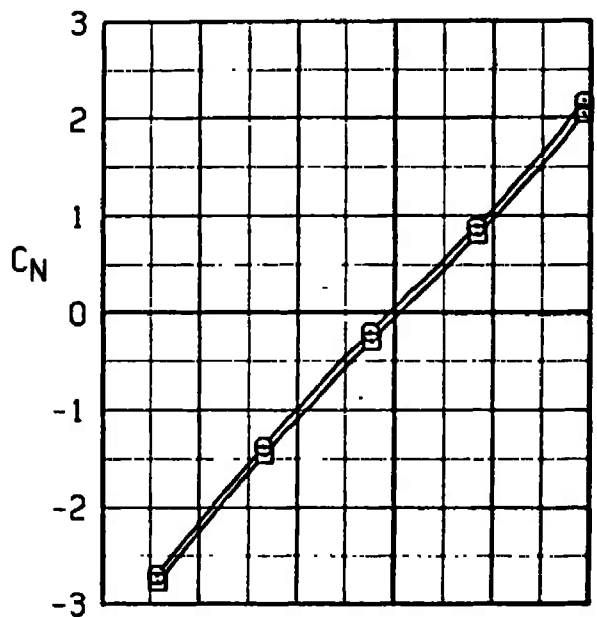
b. $C_{m\alpha}$ versus M_∞
 Figure 38. Continued.

CONFIG	REMARKS	CONFIG	REMARKS
○ 18	CLEAN, OGIVE CYLINDER	△ 9	+ VERTICAL FIN
△ 17	+ PITOT PROBE	◊ 8	+ VDMI ANTENNAS
□ 16	+ C-BAND ANTENNAS	▷ 7	+ T5 POD
◇ 15	+ FOREBODY ANTENNAS	◊ 6	+ INLET AND INLET ANTENNA
▽ 14	+ LAUNCH PINS	△ 2	+ T4 AFTERBODY
○ 13	+ RADOMES	○ 3	- ALL ANTENNAS
◇ 12	+ CANARDS	▽ 4	- CANARDS
△ 11	+ WINGS	× 5	- VERTICAL FIN + CANARDS



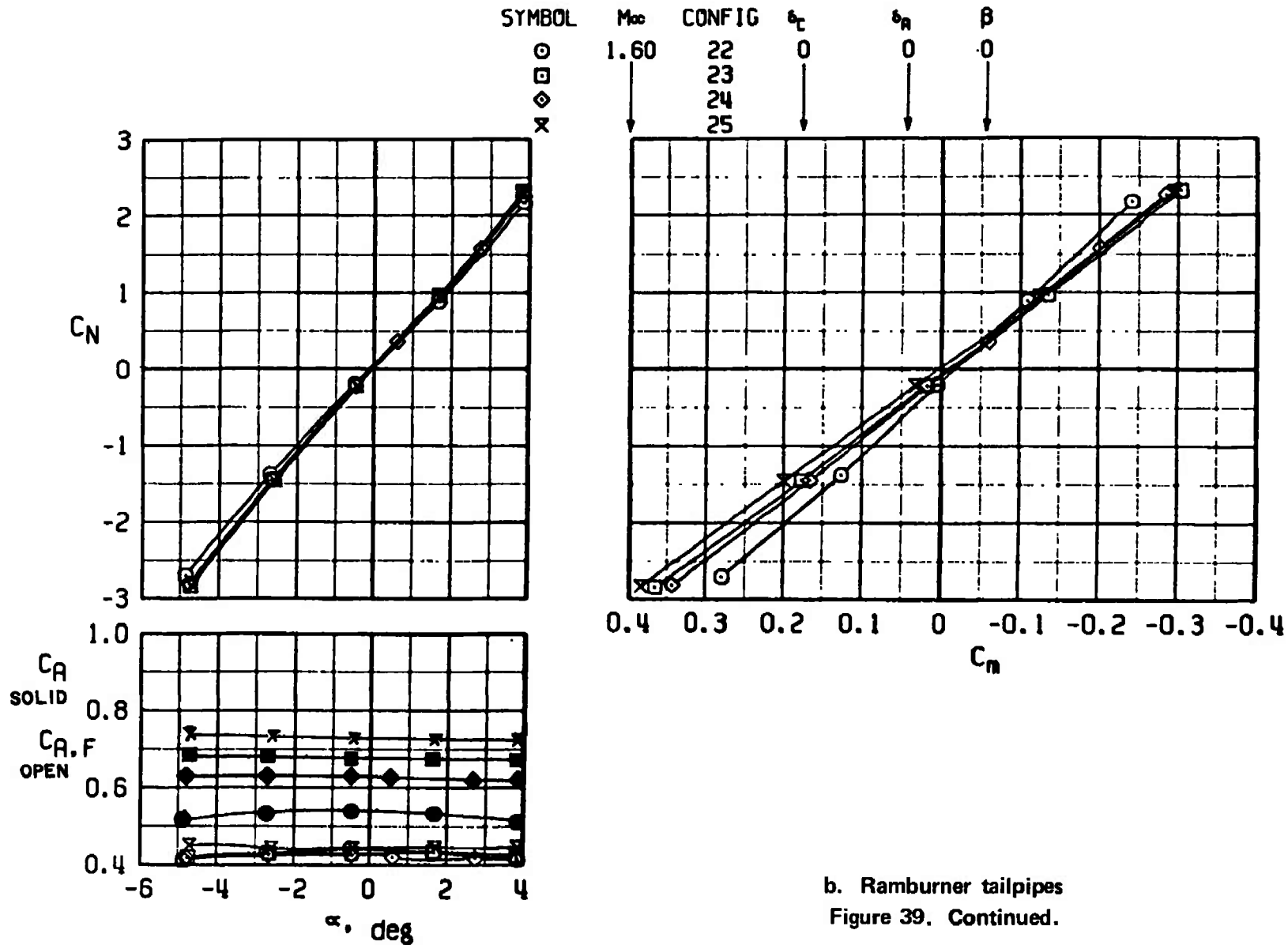
c. $C_{A,F}$ versus M_∞
 Figure 38. Concluded.

SYMBOL	M_{∞}	CONFIG	δ_c	δ_a	β
□	1.60	21	0	0	0
○	↓	22	↓	↓	↓



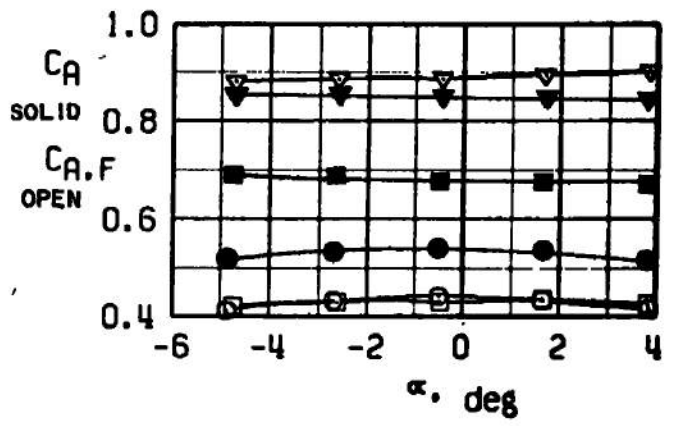
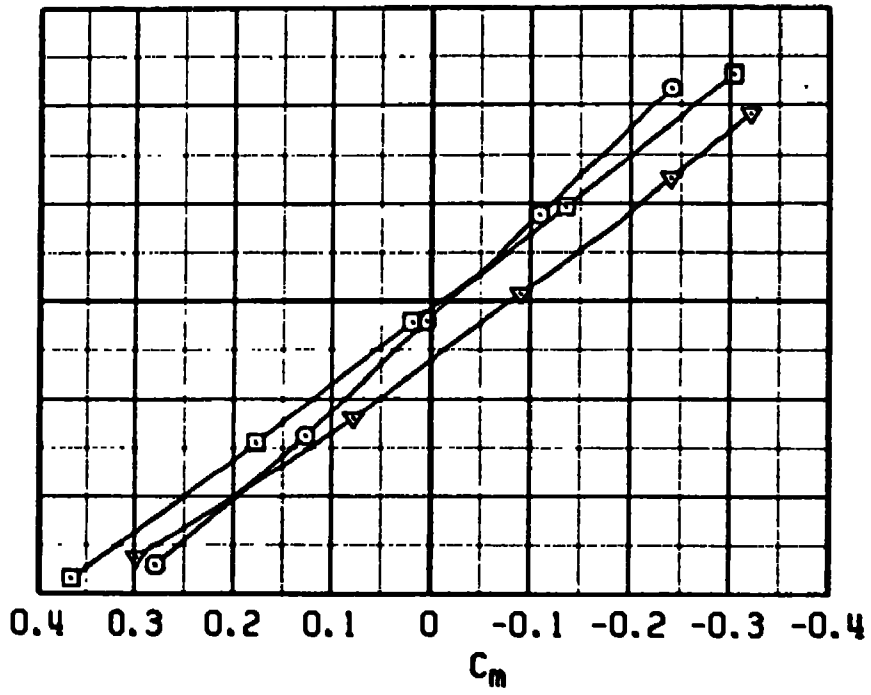
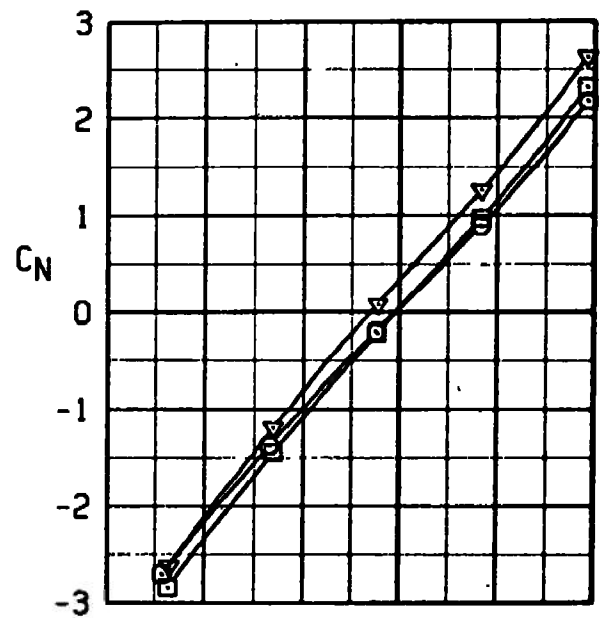
a. Raceways

Figure 39. Effects of missile components on the normal-force, pitching-moment, and axial-force coefficients, $M_{\infty} = 1.6$, $\delta_c = \delta_a = \beta = 0$.



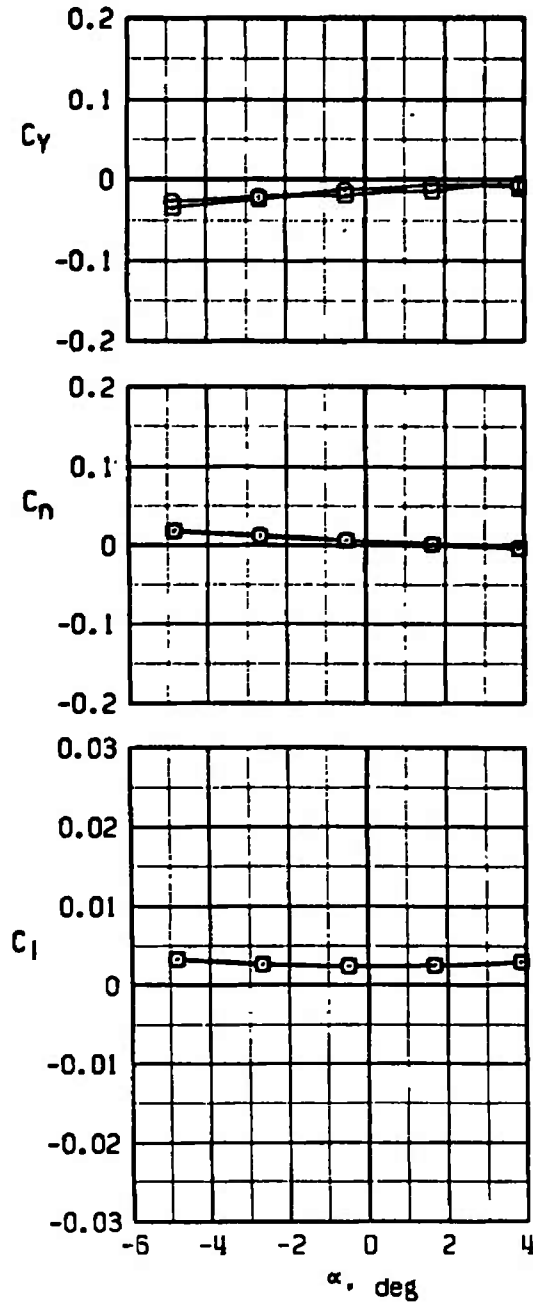
b. Ramburner tailpipes
Figure 39. Continued.

SYMBOL	M_∞	CONFIG	ϵ_c	ϵ_R	β
○	1.60	22	0	0	0
□	↓	23	↓	↓	↓
▽	↓	26	↓	↓	↓



c. Inlet
Figure 39. Concluded.

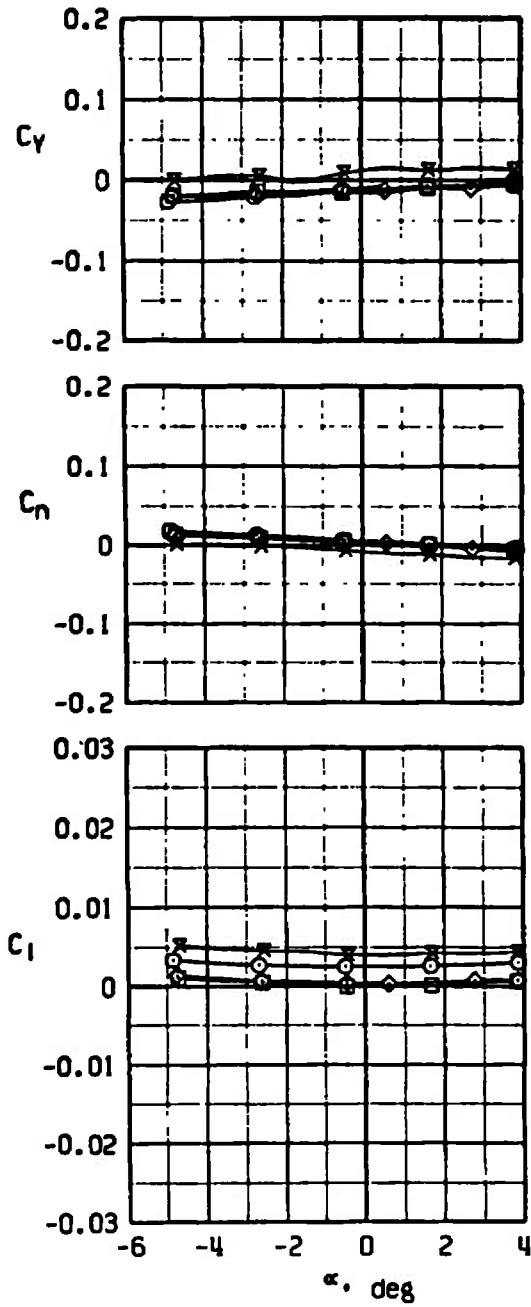
SYMBOL	M_{∞}	CONFIG	δ_c	δ_a	β
□	1.60	21	0	0	0
○	↓	22	↓	↓	↓



a. Raceways

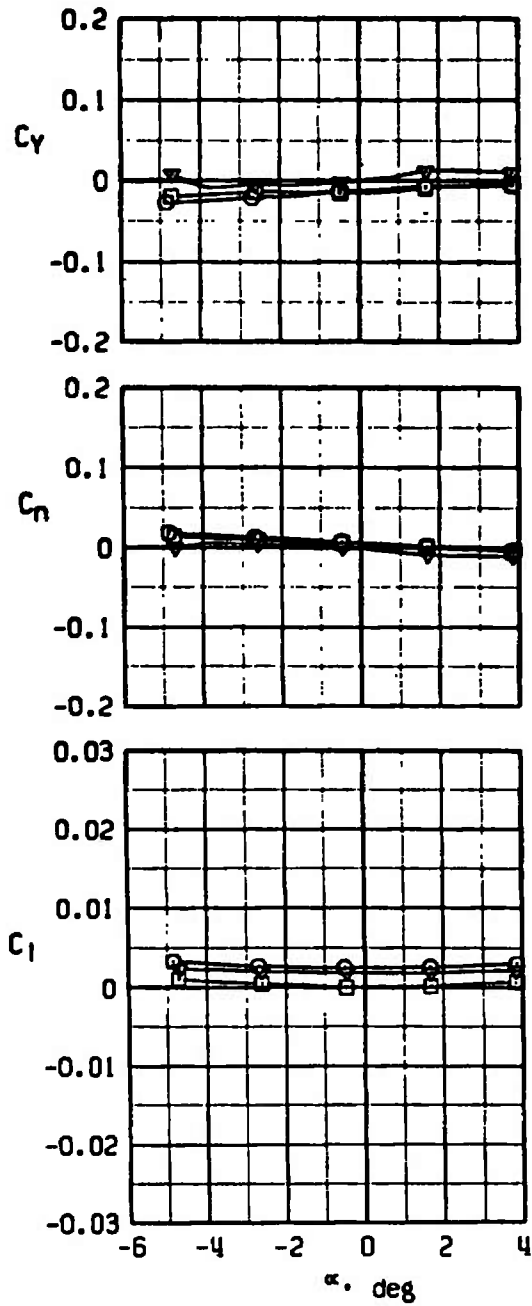
Figure 40. Effects of missile components on the side-force, yawing-moment, and rolling-moment coefficients, $M_{\infty} = 1.6$, $\delta_c = \delta_a = \beta = 0$.

SYMBOL	M _∞	CONFIG	ϵ_c	ϵ_n	β
○	1.60	22	0	0	0
□	↓	23	↓	↓	↓
◇		24			
x		25			



b. Ramburner tailpipes
Figure 40. Continued.

SYMBOL	M_∞	CONFIG	ϵ_c	ϵ_n	β
⊙	1.60	22	0	0	0
⊠	↓	23	↓	↓	↓
▽	↓	26	↓	↓	↓



c. Inlet
 Figure 40. Concluded.

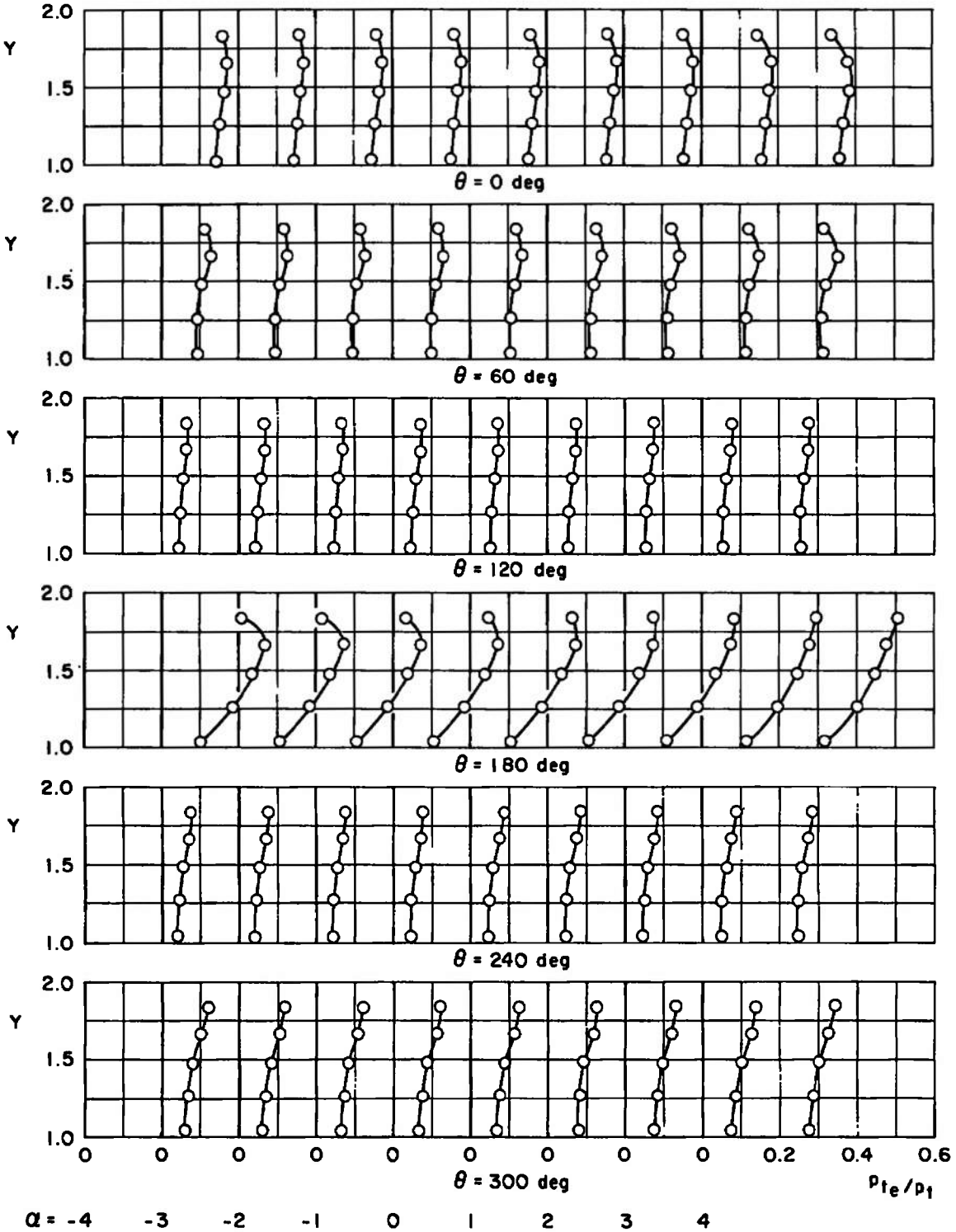


Figure 41. Effects of angle of attack on the inlet exit total pressure distributions, $\delta_c = \delta_a = \beta = 0$.

Table 1. Configuration Listing

Configuration	HAST I Components												
	Canards	Wings	T ₅ Pod	Vertical Fins	HAST I Inlet	Afterbody	Antennas						
							Inlet (1)	VDMI (2)	Radomes (2)	Launch Pins (2)	Forebody (3)	C-Band (4)	Pitot Probe (1)
1	On	On	On	On	On	T ₃	On	On	On	On	On	On	On
2	↓	↓	↓	↓	↓	T ₄	↓	↓	↓	↓	↓	↓	↓
3	Off	↓	↓	↓	↓	↓	Off	Off	Off	Off	Off	Off	Off
4	On	↓	↓	Off	↓	↓	↓	↓	↓	↓	↓	↓	↓
5	↓	↓	↓	On	↓	Off	On	On	On	On	On	On	On
6	↓	↓	↓	↓	Off	↓	Off	↓	↓	↓	↓	↓	↓
7	↓	↓	Off	↓	↓	↓	↓	↓	↓	↓	↓	↓	↓
8	↓	↓	↓	↓	↓	↓	↓	↓	↓	↓	↓	↓	↓
9	↓	↓	↓	↓	↓	↓	↓	Off	↓	↓	↓	↓	↓
11	↓	↓	↓	↓	↓	↓	↓	↓	↓	↓	↓	↓	↓
12	↓	Off	↓	↓	↓	↓	↓	↓	↓	↓	↓	↓	↓
13	Off	↓	↓	↓	↓	↓	↓	↓	↓	↓	↓	↓	↓
14	↓	↓	↓	↓	↓	↓	↓	↓	Off	↓	↓	↓	↓
15	↓	↓	↓	↓	↓	↓	↓	↓	↓	Off	↓	↓	↓
16	↓	↓	↓	↓	↓	↓	↓	↓	↓	↓	Off	↓	↓
17	↓	↓	↓	↓	↓	↓	↓	↓	↓	↓	↓	Off	↓
18	↓	↓	↓	↓	↓	↓	↓	↓	↓	↓	↓	↓	Off

Configuration	HAST II Components								
	Canards	Wings	Vertical Fins	T ₅ Pod	Afterbody	Raceway	Ramburner Tailpipe	HAST II Inlet	Antennas
21	On	On	On	Off	Off	Modified	Off	Off	Off
22	↓	↓	↓	↓	↓	HAST I	↓	↓	↓
23	↓	↓	↓	↓	↓	HAST II	1	↓	↓
24	↓	↓	↓	↓	↓	↓	2	↓	↓
25	↓	↓	↓	↓	↓	↓	3	↓	↓
26	↓	↓	↓	↓	↓	↓	1	On	↓

Table 2. Wind Tunnel Test Conditions

M_∞	p_t , psf	T_t , °R	p_∞ , psf	q_∞ , psf	$Re_\ell \times 10^{-6}$
0.5	3210	560	2700	480	18.0
0.8	2380	↓	1560	700	18.7
0.95	1980	↓	1110	↓	16.4
1.10	1760	↓	820	↓	15.2
1.30	1640	↓	590	↓	13.9
1.60	1660	550	390	↓	14.0

Table 3. Test Summary

M_∞	Configuration	Inlet Orifice No.	α , deg	β , deg	δ_c , deg	δ_a , deg	
0.8, 0.95, 1.10, 1.30 ↓ 0.5, 0.8, 0.95, 1.1, 1.3 0.8, 0.95, 1.1, 1.3 ↓ 1.6 ↓	1	5	-4 to 12	0	0(a), 10, 20	0	
	1	↓	↓	↓	0	10	
	2	↓	↓	↓	0(a), 10, 20 -10, -20	0	
	↓	↓	↓	↓	0, 10, -10	0	
	↓	↓	↓	↓	0	5	
	↓	↓	↓	↓	0, 6	0, 20	10
	↓	↓	↓	↓	0	0	0
	↓	3	5	↓	0, 6	0(a), 20	0
	↓	↓	↓	↓	0	10, -10, -20	0
	↓	4	↓	↓	0	0	10
	↓	5	↓	↓	0, 6	Off	0
	↓	6	↓	↓	0, 6	0, 20	↓
	↓	7, 8, 9, 11	---	↓	0	0	↓
	↓	12	↓	↓	↓	↓	Off
	↓	13, 14, 15, 16, 17, 18	↓	↓	↓	Off	Off
↓	1, 2, 3	5	↓	0, 6	0, 10, 20	0	
↓	2	5	↓	0	0	10	
↓	2	1	↓	0	0	0	
↓	21, 22, 23, 24, 25, 26	---	-4 to 4	0	0	0	

a - Denotes extended α range of -10 to 27 deg ($\beta = 0$)

NOMENCLATURE

A_b	Model base area, sq ft
A_c	HAST I inlet cowl area, 0.64 in. ²
A_e	HAST I inlet exit area, 1.41 in. ²
A_o/A_c	Inlet capture area ratio, see Eq. (1)
A_p	HAST I inlet plenum area, 1.01 in. ²
A_t	Inlet throat area, in. ²
C_A	Axial-force coefficient, axial force/ $q_\infty S$
$C_{A,b}$	Base axial-force coefficient, $[(p_\infty - p_b)/q_\infty] (A_b/S)$
$C_{A,F}$	Forebody axial-force coefficient, $C_A - C_{A,b}$
$C_{A_i,e}$	Inlet axial-force coefficient, see Eq. (2)
C_ℓ	Rolling-moment coefficient, rolling moment/ $q_\infty S \ell$
$C_{\ell \delta_a}$	Rolling-moment derivative, $\partial C_\ell / \partial \delta_a$, per degree
C_m	Pitching-moment coefficient, pitching moment/ $q_\infty S \ell$
$C_{m \alpha}$	Pitching-moment derivative, $(\partial C_m / \partial \alpha)_{\alpha=0}$, per degree
$C_{m \delta_c}$	Pitching-moment derivative, $\partial C_m / \partial \delta_c$, per degree
C_N	Normal-force coefficient, normal force/ $q_\infty S$
$C_{N \alpha}$	Normal-force derivative, $(\partial C_N / \partial \alpha)_{\alpha=0}$, per degree
C_n	Yawing-moment coefficient, yawing moment/ $q_\infty S \ell$
C_Y	Side-force coefficient, side force/ $q_\infty S$
$f(M_p)$	Inlet plenum mass flow function, see Fig. 5
$f(M_\infty)$	Free-stream mass flow function for isentropic flow, see Fig. 5
g	Acceleration due to gravity, 32.174 ft/sec ²

l	Reference length, model length, 4.167 ft
M_e	Inlet exit Mach number
M_∞	Free-stream Mach number
p_b	Model base pressure, psfa
p_{se}	Inlet exit static pressure, psfa
p_{sp}	Inlet plenum static pressure, psfa
p_t	Free-stream total pressure, psfa
p_{t2}	Total pressure downstream of a normal shock at free-stream Mach number, psfa
p_{te}	Inlet exit total pressure, psfa
p_{tp}	Inlet plenum total pressure, psfa
p_∞	Free-stream static pressure, psfa
q_∞	Free-stream dynamic pressure, psfa
R	Universal gas constant, 1716 ft ² /sec ² °R
Re_l	Free-stream Reynolds number based on model length
S	Reference area, model cylinder cross-section area, 0.0576 sq ft
T_t	Free-stream total temperature, °R
V_∞	Free-stream velocity, ft/sec
Y	Radial distance from model centerline, in. (see Fig. 3m)
α	Model angle of attack, deg
α_t	Model trim angle of attack, deg
β	Model angle of sideslip, deg
γ	Specific heat ratio, 1.4

- δ_a Aileron deflection angle relative to model centerline, deg (see Fig. 4)
- δ_c Canard deflection angle relative to model centerline, deg (see Fig. 4)
- θ Model circumferential angle, deg (see Fig. 3m)